Millimeter-wave 39 GHz 4×4 Phased Antenna Array with Embedded Near-field Probing Antenna for Performance Enhancement

by

Huixin Jin

A thesis
presented to the University of Waterloo
in fulfillment of the
thesis requirement for the degree of
Master of Applied Science
in
Electrical and Computer Engineering

Waterloo, Ontario, Canada, 2023

Author's Declaration

I hereby declare that I am the sole author of this thesis. This is a true copy of the thesis, including any required final revisions, as accepted by my examiners.

I understand that my thesis may be made electronically available to the public.

Abstract

Beamforming arrays are a vital technology for millimeter-wave (mm-wave) wireless communication systems. A large amount of research and an increasing number of phased array prototypes have been developed which provide high data rates and low latency. However, as sub-6 GHz bands have limited bandwidth and crowded spectrum occupation, mm-wave phased arrays are more desirable for future generation systems. Yet, there are challenges with current phased array technologies that need to be addressed by researchers. Linear power amplifier response, radio frequency front-end calibration, and affordable prototyping costs are the main challenges that must be taken into consideration when designing arrays for mm-wave systems.

This thesis discusses approaches to these challenges and trade-offs and proposes an optimized design solution. A novel wideband near-field (NF) probing antenna is proposed that can be embedded in mm-wave phased arrays to provide the feedback signal path necessary for carrying out array calibration and digital pre-distortion training. Specifically, the topology and layout of the proposed NF probing antenna have been carefully devised to achieve a coupling to its surrounding antenna elements with flat magnitude and constant group delay. A proof-of-concept 4×4 linear-polarized active phased array prototype with embedded NF probing antennas is designed to operate over 37-41 GHz. A 4×4 linear-polarized active phased array without NF probing antenna is also fabricated to serve as a benchmark. Measurements confirm the negligible impact of the NF probing antennas on the antenna array's radiation pattern. Furthermore, the active phased array prototype with embedded NF probing antennas was successfully used to train a digital pre-distortion function which enabled the effective isotropic radiated power to be increased from 32 dBm to 34.3 dBm, while maintaining an error vector magnitude below 3.5%, when the array was steered from $-50°$ to $50°$.

Acknowledgements

Most especially, I would like to thank my parents, Hao and Nan, for raising me with all love and kindness, and supporting me throughout years of living and studying in Canada. Without them, I would never have had the opportunity to study at the University of Waterloo and this thesis would not have been possible.

I would like to thank Professor Slim Boumaiza for his supervision and help with my Masters and Undergraduate studies since 2020, for his superior guidance in my research and career development, and for providing the necessary logistics and resources for completing my research projects.

I would like to thank my boyfriend Yushi Cao, for the encouragement, for taking care of me, and for all the academic discussions in this journey.

I would like to thank Ahmed Ben Ayed, Nizar Messaoudi, and Jingjing Xia for helping with the lab measurement and providing tons of new ideas that would be remembered in history; Ziran He, and Bernard Tung for supporting and backing each other up, and working together as a team.

Last but not least, I would like to thank each member of the EmRG family for every moment that we shared and for memories that all will cherish.

Table of Contents

List of Figures

viii

List of Tables

Chapter 1

Introduction

1.1 Motivation

An explosion of research into wireless communications has occurred since the 1980s, as mobile communication has become an indispensable essential, integrated into everyone's daily life [27]. As the world's population grows and the demands of advanced technologies multiply, researchers and industrial developers have been working hard to improve the quality of life for human beings. In 2017, the Third Generation Partnership Project (3GPP) approved the first package for Release 15, announcing the first fifth-generation (5G) new radio (NR) standards. In the years that followed, 3GPP launched Releases 16, 17, and 18, exploiting new spectrum bands for 5G NR and more sophisticated radio operation schemes [28]. Compared to the fourth-generation (4G) technology, Fig. 1.1 shows that
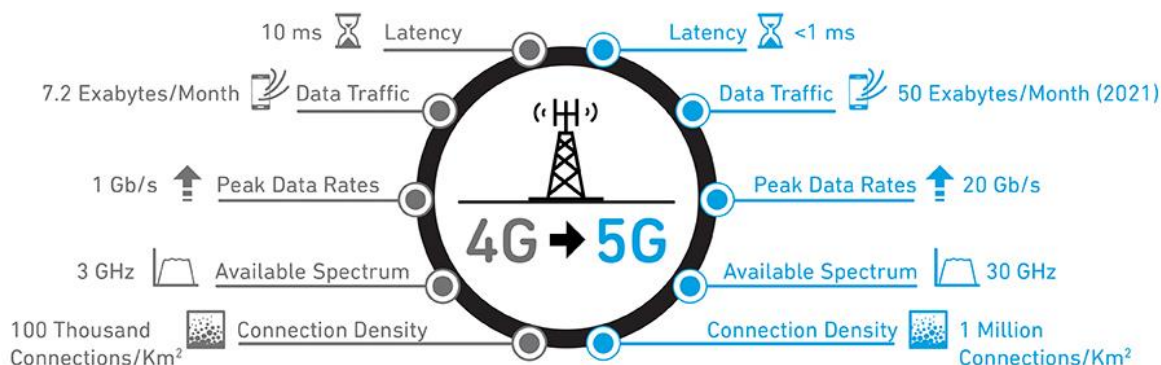
Figure 1.1: Comparison of 4G and 5G networks. [1]
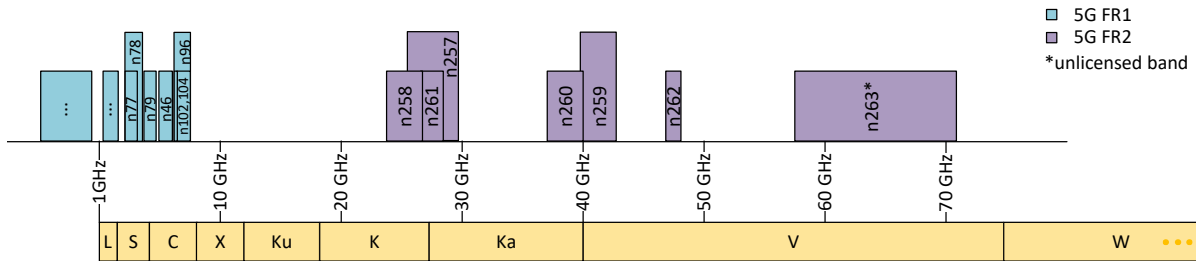
Figure 1.2: 5G NR frequency spectrum and corresponding radar letter designations [2], [3], [4].

5G NR can support faster data rates, lower latency, and higher reliability [29]. According to Quovo [1], the latency of the 5G network can achieve 1 ms, which is one-tenth of the 4G network. Such low latency is critical for supporting fundamental infrastructure such as cloud computing/storage, front/backhaul links, and smart cities. 5G can achieve peak data rates of 20 Gb/s, 20 times higher than 4G networks, and has 10 times more spectrum available than 4G's total of 3 GHz. In addition, the connection density of a 5G network is able to achieve 1 million connections per one squared kilometer. The accommodation of such high loads allows data-intensive communications such as video streaming and smart transportation systems. Fig. 1.2 shows the frequency spectrum of 5G NR separated into two frequency ranges. FR1 contains the bands which mostly fall in sub-6 GHz, while FR2 includes the frequency bands from 24.25 GHz to 52.6 GHz. The detailed standardized band coverage and the corresponding radar letter designations are also illustrated in Fig. 1.2 [2], [3], [4]. Comparing the frequency bands of FR1 and FR2, it is obvious that the available spectrum in FR2 is much wider than that of FR1. This has attracted the attention of researchers and industrial developers, resulting in the rapid progress of mm-wave technology development operating at 5G FR2 in recent years.

One of the most famous applications in 5G is phased arrays. Phased arrays consist of multiple antenna elements with different geometric arrangements, with the ability to steer and aim each beam radiated from the antenna elements in different directions through digitally controlling the signals' relative phase and amplitude in each element. The metrics of phased array technology such as low latency, high speed, and wide bandwidth, make it a good candidate for implementation in base stations, indoor smart cell access, and intelligent vehicle networks [27].

2

1.2 Problem Statement

The challenges faced in mm-wave phased array antenna design come from multiple sources. Firstly, the wavelength is short at mm-wave frequencies, which decreases the antenna spacing and the overall array size. Such limited spacing brings difficulties in designing the layouts of radio frequency (RF) beamforming integrated circuits (ICs) and phased arrays. All components, such as power supply(s) and digital signal routing, are required to fit in a compact footprint. Moreover, the cost of these highly integrated modules increases significantly as the frequency goes up. Despite the challenges in designing the phased array itself, the processes of array fabrication and deployment are also important. For example, due to manufacturing imperfections, complex RF signal routing, and non-ideal measurement setups in practice, beamforming arrays typically require calibration in the factory and even in-field after deployment. This step is essential to ensure optimal beamforming performance and maintain desired RF system quality.

Although beamforming arrays are used in mm-wave communication systems to combat high propagation path losses, the downside of incorporating such large numbers of elements is higher power consumption. To achieve optimal power efficiency, power amplifier (PA) elements need to operate in the non-linear region. However, this degrades signal quality and may even violate spectral emission regulations. To compensate for this, digital pre-distortion (DPD) blocks are added to the digital signal processing (DSP) chain, and are used to pre-distort the signal to make the final output signal from the PA appear linear [30].

To apply array calibration and DPD to phased arrays, a feedback mechanism is required to provide the captured signals that radiate from the transmitting phased arrays and feed them back to the DSP block to apply the corresponding algorithms. In recent years, a number of calibration and DPD algorithms have been developed, however, few research groups have implemented their theories into practical hardware-level devices. Some work has shown great theoretical promise but due to hardware limitations, either there are no real-world prototypes (and measurement data) to validate the theory, or, if prototypes have been fabricated, they are not fully representative or suitable to prove the proposed concepts. Therefore, an implementable feedback mechanism for phased arrays is needed to apply calibration and DPD training to enhance overall array performance.

This thesis proposes the design of a reliable wideband near-field (NF) probing antenna embedded into an mm-wave phased array to provide feedback signals. This would enable the array's calibration and DPD training without requiring any additional external receiver or transmitter being added to the system.

1.3 Thesis Organization

This thesis is organized as follows.

Chapter 2 presents the background and relevant principles of antenna phased array design and operation including antenna elements, beamforming, antenna fabrication processes, and printed-circuit board (PCB) stack-up. Recent work on beamforming arrays and NF-based RF beamforming array calibration techniques from the literature are reviewed.

The remaining chapters outline the design and validation of a novel NF probing antenna. Chapter 3 covers the detailed design of the proposed NF probing antenna embedded in a 4x4 linear-polarized phased array; design constraints and simulation results are discussed as well. Validation results for the proposed design's fabricated prototypes are presented in Chapter 4. The thesis concludes with a discussion in Chapter 5 that includes recommendations for future work.

Chapter 2

Background and Literature Review

2.1 Background

2.1.1 Key Performance Indicators in Antenna and Phased Array Systems

The performance of a phased array is strongly dependent on the design of its antenna elements and their overall integration. Therefore, it is necessary to design qualified antenna elements/arrays first and then optimize their performance with other integrated modules within a system to realize beamforming capability. The following lists key parameters important to antenna and array system designs.

1. **Radiation Power Density and Radiation Power Intensity**: The radiation power density and radiation power intensity are fundamental metrics that link electromagnetic (EM) waves to practical parameters such as directivity, gain, and (therefore) radiation pattern. The radiation power density (P_{rad}), with a unit of W/m^2, is defined as the amount of power transmitted per unit area from an observation surface, where the surface is usually a large sphere with radius r, and r exceeds the far-field distance. The radiation power intensity (U) is based on the radiation power density, translating a 2-dimensional measurement into a 3-dimensional one. The radiation power intensity is a multiple of the radiation density and the square of distance r, and its unit is described as W/unit solid angle. Both measures are related to the observer's position, and use the spherical coordinate as a convenient coordinate for antenna analysis in most cases. In a spherical coordinate, θ and ϕ

represent the angle with respect to the polar axis (z-axis), and the angle of rotation on the x-y plane, respectively.

2. **Insertion Loss, Antenna Radiation Efficiency, and Antenna Efficiency**: There are three major losses that happen in antennas designs, reflection loss (e_r), dielectric loss (e_d) and conductor loss (e_c) [31]. The reflection loss is caused by the mismatch of the antenna, since the antenna cannot be perfectly matched in reality, so a part of the incident wave reflects back, decreasing the overall antenna efficiency. Dielectric and conductor losses are difficult to measure in practice as they are caused by multiple factors such as frequency, dielectric, and conductor characteristics. For example, when the dielectric constant of the substrate is low, the capacity to concentrate EM energy inside the substrate decreases, thus losses increase. In addition, skin depth is an important contributor to conductor losses. At 0 GHz (DC), the current flows through the entire cross area of the conductor; however, by increasing the frequency, the current only uses the outer skin of the conductor to flow so the current density is at its maximum near the surface of the conductor [32]. In terms of PCB-based microstrip antennas, the surface roughness of the exposed antenna patch and feeding lines, and the roughness between the conductors and dielectrics during the lamination cycles, would all contribute to the overall loss of the antenna. In general, antenna efficiency (e_0) is written as (2.1):

$$e_0 = e_r e_d e_c \tag{2.1}$$

where $e_d e_c$ represents the antenna's radiation efficiency.

3. **Directivity and Antenna Gain**: Directivity (D) is a dimensionless measure calculated as a ratio of the radiation intensity in a given direction to the radiation intensity averaged over all directions. For an isotropic antenna, the directivity is 1. Since power can be derived from the radiation intensity, directivity can also represent the ratio of radiated power in a given direction to the averaged radiated power across all directions—this is useful when comparing beam focusing capability between antennas [33]. Furthermore, the antenna gain will follow the same pattern/shape as the directivity does but with different magnitudes, as the antenna gain has to take antenna radiation efficiency $e_d e_c$ into account.

4. **Equivalent Isotropic Radiated Power and Path Loss**: Equivalent isotropic radiated power (EIRP) is the amount of hypothetical power that an ideal isotropic antenna would need to radiate in order to achieve the same beam strength that is radiated by an actual antenna in a particular direction, where the ideal isotropic
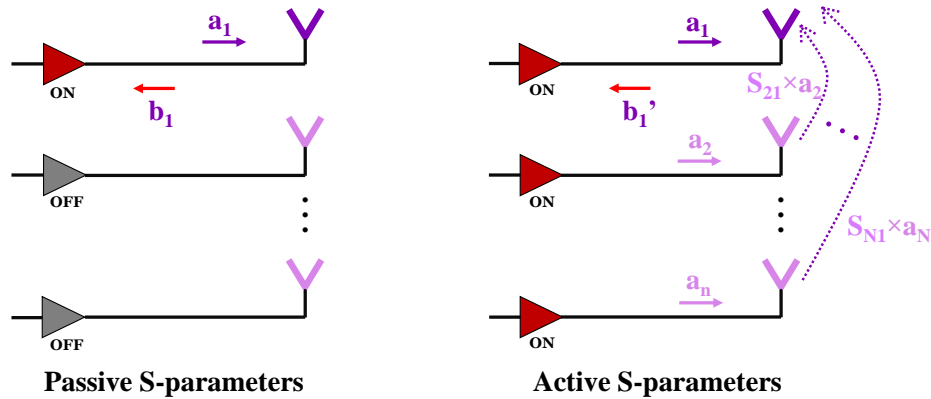
Figure 2.1: Illustrations of passive and active S-parameters.

antenna has the same power radiated in all directions [31]. The following equation is used to calculate EIRP:

$$EIRP(dBm) = P_{\text{out, TX}}(dBm) + G_{\text{TX}}(dB) \tag{2.2}$$

where $P_{\text{out, TX}}$ is the total output power from the PAs accounting for any mismatch, and G_{TX} is the realized antenna gain including antenna radiation efficiency. In addition to EIRP, path loss is another key metric in calculating the link budget. According to the Friis equation, the free space loss of a signal propagating through a line-of-sight path is defined as (2.3):

$$L(dB) = -20 \times log_{10}(\frac{\lambda}{4\pi d}) \tag{2.3}$$

where λ is the wavelength of the signal and d is the distance between the transmitter and the receiver. As illustrated in equation (2.3), the wavelength is inversely proportional to the loss while the distance is directly proportional to the loss.

5. **Mutual Coupling and Active Loading**: Ideally, each antenna's ports within an array are isolated at RF frequencies. However, some coupling exists in practical implementation, resulting in the transmitted signal coupling back to the transmitting array. In FR1 operation, isolators are usually inserted between PAs and antennas to ensure this coupled signal does not present at the PAs' outputs. However, this method is not practical at mm-wave frequencies due to the space constraint discussed in Chapter 1. This coupled signal modulates the loading of the PAs and can cause additional non-linearity. Therefore, it is desirable to reduce the proportion of the

signal picked up by nearby antennas, effectively reducing the mutual couplings between antenna elements. The modulated loading presented at a PA's output can be represented by active S-parameters (a function of mutual couplings and each antenna's output), as shown in Fig. 2.1 (b), while Fig. 2.1 (a) represents the passive S-parameters when only one PA (RF chain) is turned on. In a multi-port network, active $\mathbf{S}_{11}$ can be calculated as (2.4):

$$Active\ \mathbf{S}_{11} = \frac{\mathbf{b}_1{'}}{\mathbf{a}_1} = \frac{\mathbf{S}_{11} \times \mathbf{a}_1 + \mathbf{S}_{21} \times \mathbf{a}_2 + \mathbf{S}_{31} \times \mathbf{a}_3 + ... + \mathbf{S}_{N1} \times \mathbf{a}_N}{\mathbf{a}_1} \qquad (2.4)$$

where N is the total number of ports in the network, $\mathbf{a}_n$ represents the incident wave that is excited at the nth port, and $\mathbf{b}_1{'}$ is the total reflect wave at port 1. This equation shows that if the mutual coupling is reduced to zero, the active loading becomes equal to the passive loading.

2.1.2 Beamforming Architectures

Beamforming arrays were initially developed for large-scale base stations in radar communication systems. As rapid developments in mm-wave technology have occurred in recent years, more attention has been focused on beamforming arrays operating in 5G mm-wave systems. Beamforming arrays consist of two main functional blocks: a set of antenna elements and a set of circuity functioning as beamforming drivers for each antenna element.

In terms of the set of antenna elements, the geometry of the antenna arrangement can vary. Antenna arrays with a size of 1×N (linear) and M×N (planar) are typically implemented in practice. In terms of a linear array with uniform spacing, Fig. 2.2 (a) and (b) demonstrate the model for analyzing the phase difference between each antenna element, when the beam is pointed to a certain direction. Fig. 2.2 (a) shows a model of a 1×4 linear array with uniform antenna spacing d, and the direction of mechanical boresight is perpendicular to the face of the antenna array. Since the radius of the spherical wavefront becomes very large in the far-field region, the assumption of parallel wave propagation paths can be made [31]. In addition, an angle of θ is defined between the mechanical boresight and the electrical boresight. The direction of electrical boresight is the same as the beam pointing direction—perpendicular to the wavefront. The phase difference between each antenna element can be derived from Fig. 2.2 (b), as an angle between the beam direction and the antenna array is ϕ, where $\phi = \pi/2 - \theta$. The distance L is easy to calculate using a trigonometric function (2.5):

$$L = dcos(\phi) = dsin(\theta) \qquad (2.5)$$
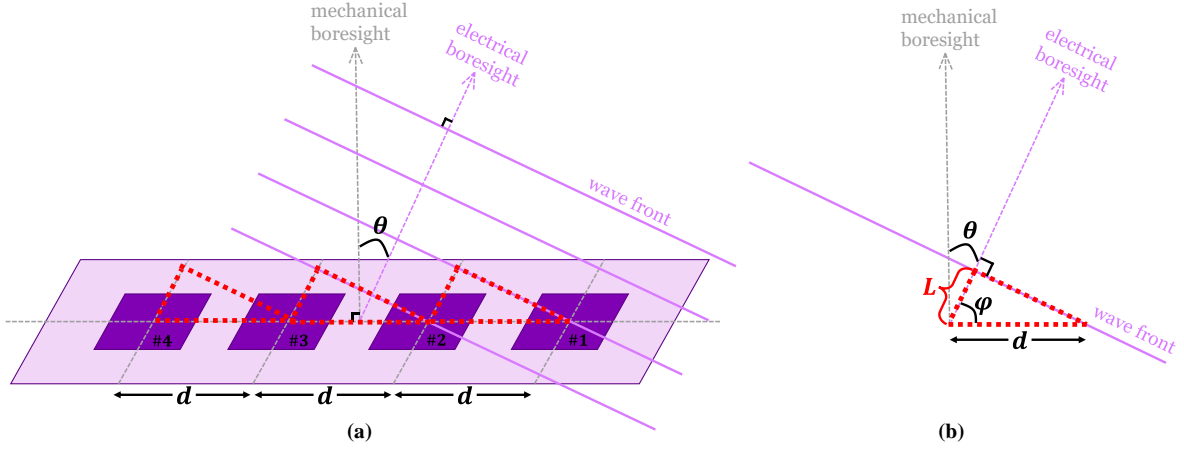
Figure 2.2: (a) Model of a linear phased array with four antenna elements observed in far-field. (b) Geometric illustration of phase difference between each antenna element.

by converting L from physical length to electrical length, the phase difference δ between each antenna elements is calculated as (2.6):

$$\delta = \frac{2\pi L}{\lambda} = \frac{2\pi d cos(\phi)}{\lambda} = \frac{2\pi d sin(\theta)}{\lambda} \qquad (2.6)$$

Therefore, if antenna element #1 is set as the reference element in Fig. 2.2 (a), then the phase difference of antenna elements #2, #3, and #4 with respect to the reference will be δ, 2δ, and 3δ, respectively. By setting the corresponding phase shifts for each antenna element, the phase difference due to wave propagation delay will be negated, and the beams radiated from each antenna element will combine coherently, thus resulting in maximum output at the targeted beam direction.

The array factor (AF) is a useful indicator that describes the beam-radiated pattern formed by a phased array. It depends on the array geometry and the beam weights from every antenna element [33]. It is important to note the AF does not relate to the antenna gain of each individual antenna element. To calculate the AF of a 1×N linear phased array, assume each antenna element has an electrical field (E-field) factor of $E_n(\mathbf{r})$, then the total E-field of a 1×N linear phased array at the observation point is given by (2.7) [31]:

$$\begin{aligned} E_{\text{total}}(\mathbf{r}) &= E_1(\mathbf{r}) + E_2(\mathbf{r}) + E_3(\mathbf{r}) + ... + E_{\text{N-1}}(\mathbf{r}) \\ &= E_1(\mathbf{r}) \times \left[1 + e^{j\delta} + e^{j2\delta} + ... + e^{j(N-1)\delta}\right] \end{aligned} \qquad (2.7)$$

9

where δ is defined in (2.6), and N is the number of antenna elements in the linear phased array. Using geometric series sum formula, equation (2.7) can be further simplified to (2.8):

$$
\begin{aligned}
E_{\text{total}}(\mathbf{r}) &= E_1(\mathbf{r}) \times \left[\frac{1 - e^{jN\delta}}{1 - e^{j\delta}} \right] \\
&= E_1(\mathbf{r}) \times \left[\frac{e^{\frac{-j\delta}{2}}}{e^{\frac{-jN\delta}{2}}} \times \frac{e^{\frac{-jN\delta}{2}}}{e^{\frac{-j\delta}{2}}} \times \frac{1 - e^{jN\delta}}{1 - e^{j\delta}} \right] \\
&= E_1(\mathbf{r}) \times \left[\frac{e^{\frac{-j\delta}{2}}}{e^{\frac{-jN\delta}{2}}} \times \frac{e^{\frac{-jN\delta}{2}} - e^{\frac{jN\delta}{2}}}{e^{\frac{-j\delta}{2}} - e^{\frac{j\delta}{2}}} \right] \\
&= E_1(\mathbf{r}) \times \left[\frac{e^{\frac{-j\delta}{2}}}{e^{\frac{-jN\delta}{2}}} \times \frac{sin(\frac{N\delta}{2})}{sin(\frac{\delta}{2})} \right]
\end{aligned}
\tag{2.8}
$$

Therefore, the AF of a 1×N linear phased array is defined as (2.9):

$$
AF(\theta) = \frac{sin(\frac{N\delta}{2})}{sin(\frac{\delta}{2})} = \frac{sin(\frac{N(\frac{2\pi dsin(\theta)}{\lambda})}{2})}{sin(\frac{(\frac{2\pi dsin(\theta)}{\lambda})}{2})} = \frac{sin(\frac{N\pi dsin(\theta)}{\lambda})}{sin(\frac{\pi dsin(\theta)}{\lambda})}
\tag{2.9}
$$

A similar analysis using 3-dimensional mathematical models can be implemented to calculate the phase difference and AF for M×N planar arrays.

In terms of beamforming systems, there are three general beamforming architectures: RF, digital, and hybrid. Fig. 2.3 (a) and (b) show an RF and a digital beamforming architecture for a Tx phased array, respectively, where the RF chain block includes digital-to-analog converter, RF filters, and mixer for frequency up-converting. In Fig. 2.3 (a), the antenna array is fed by one stream of baseband signal, which is split equally to each antenna element. Each antenna element has its own phase and amplitude controls, therefore, by setting the phase and amplitude controls of each antenna element, a directional beam or beams can be formed to point toward a particular target(s). However, since the RF beamforming architecture has only one RF chain, it lacks flexibility—the major disadvantage of using this architecture. For massive multiple-input multiple-output (MIMO) systems, it is necessary to have multiple directive communication paths to serve multiple users. Thus, an RF beamforming architecture is not appropriate for massive MIMO systems. However, the size and circuit complexity of RF beamforming architectures are
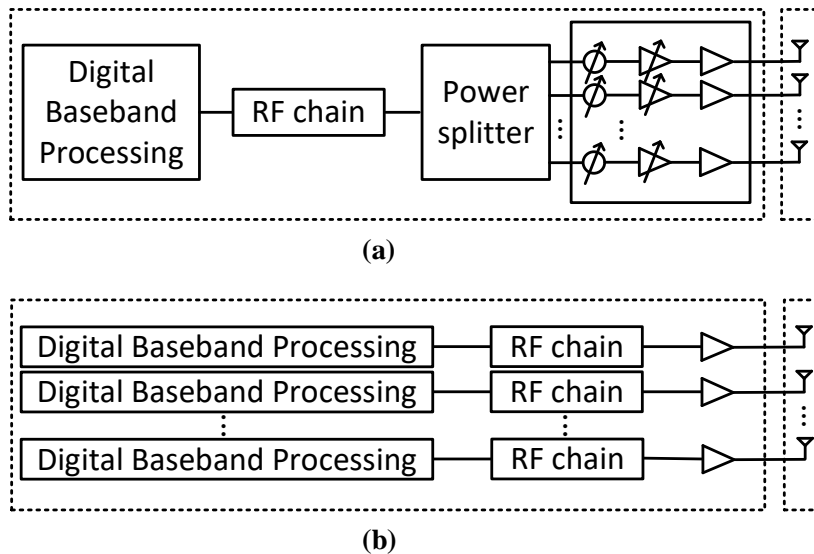
Figure 2.3: Architecture of (a) RF beamforming array, (b) digital beamforming array.

the smallest among the three architecture types. In the digital beamforming architecture, each antenna element has its own data stream and its phase/amplitude controls are implemented entirely in the digital circuitry at the baseband. This enables the antenna array to transmit multiple beams carrying different signals at the same time, making it a suitable candidate for massive MIMO systems. Although this architecture is more flexible, it requires bulky circuity and higher power consumption. As shown in Fig. 2.3 (b), the number of antenna elements should be equal to the number of RF chains and digital baseband processors. For the transmitter case, each RF chain contains a digital-to-analog converter (DAC), upconverter, filters, and PAs. This means that the cost and power consumption would increase significantly as the array size becomes larger [34]. The final architecture type, hybrid beamforming, is a mix of RF and digital beamforming architectures as its name suggests. It consists of multiple sets of RF beamforming arrays, each array with its own digital baseband processor. The hybrid beamforming architecture balances the advantages and disadvantages of the previously described beamforming architectures. It provides an opportunity for multi-stream functionality without occupying too much circuit area and it offers a balanced solution between power consumption and capabilities.

2.2   Literature Review

A huge number of RF beamforming array prototypes have been developed recently, as they are relatively simple to implement compared to the other beamforming architectures. However, there are still many challenges to be overcome in integrating the antenna arrays and the beamforming circuitry. To conquer these challenges, researchers have tried to implement phased arrays using different packaging techniques and fabrication processes such as PCB-based antenna arrays with flip-chip beamforming ICs, antenna-in-package, and antenna-on-chip (silicon-based). Furthermore, some alternatives for array calibration and DPD training in beamforming arrays are also reviewed.

2.2.1   Recent Works in Millimeter-wave RF Beamforming Arrays

The choice of packaging techniques and fabrication processes needs to be made considering the design specifications of the antenna arrays, including operating frequency, type of beamformer chip, PCB stack-up, targeted bandwidth, polarization, and size of the antenna array (number of antenna elements). The following discusses several existing RF beamforming array designs, each using different packaging techniques and fabrication processes.

1. **Multi-layer laminated PCB with flip-chip interconnection**: PCB-based phased arrays are the most traditional and commonly used in both the research and industry fields, given PCB technology has been developed since the 1940s. Such a long history brings with it mature technology and reliable, relatively low-cost manufacture. However, the frequency of operation is the most important factor limiting PCB-based phased arrays. Most antennas operating below 60 GHz are built on PCB technology, with the substrates reaching their upper limits when the system operates at higher frequencies [35]. The PCB stack-up is one of the most important features in antenna design. It must be determined before designing an antenna because it is necessary to set up all simulations correctly, according to the PCB stack-up. There are two main PCB fabrication processes: traditional multi-layer laminated and high-density interconnect (HDI) PCB. The simplest PCB structure is a single-sided board, containing a single copper layer and a substrate layer. It is also possible to use a double-sided PCB containing two layers of copper, one on top and one below, with the substrate layer sandwiched between. In terms of system integration, designers are trying to integrate multiple modules into a single package rather than cascading multiple discrete components together. The first reason is to reduce additional connection losses due to high operating frequency. The second reason is to save package
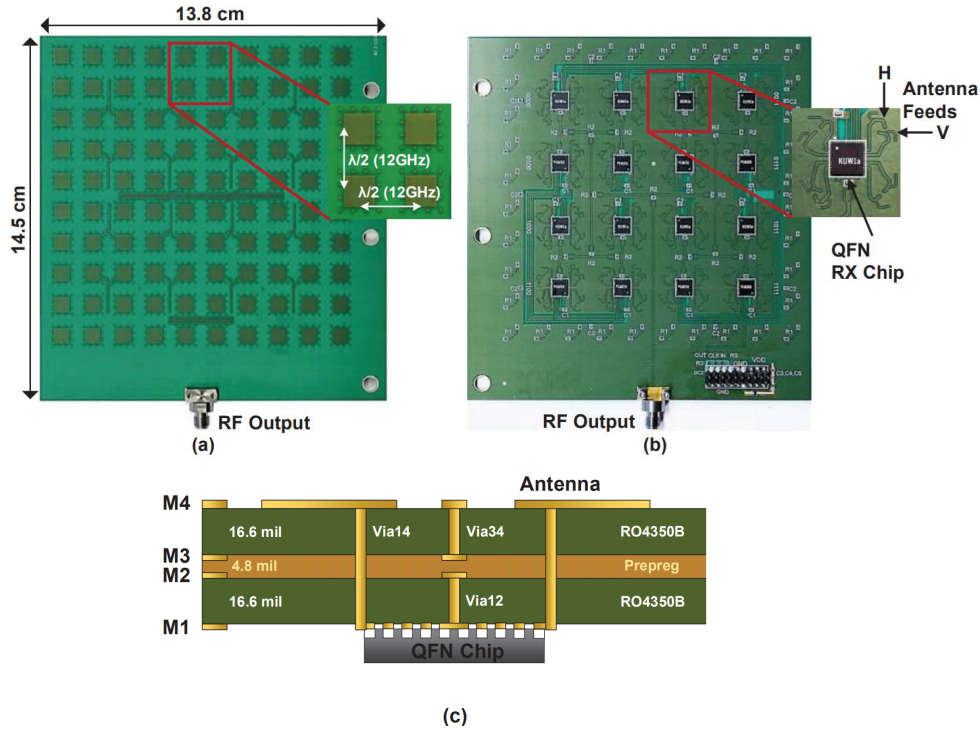
Figure 2.4: (a) Front view of 8×8 dual-polarized phased array PCB surrounded by 36 dummy antennas. (b) Back view of PCB with 16 beamformer chips. (c) Low-cost 4-layer PCB stack-up. [5]

area to reduce cost—at high frequencies the price is calculated per unit area. To integrate multiple modules on a PCB, more available layers are required to accommodate extra circuitry such as digital signal routing, power planes, and the antenna ground. In addition, EM shielding plays a key role in RF performance, so additional layers are required to apply RF shielding for antenna elements. Therefore, multi-layer laminated circuit boards are necessary for highly-integrated systems.

Aljuhani and other authors in [5] proposed an ultra-low cost PCB-based 8×8 dual-polarized phased array at Ku-band. The phased array is built on a 4-layer PCB with Roger 4350B as substrate. As shown in Fig 2.4, the antenna patches are located on M4, with M3 acting as antenna ground while a 4-stage Wilkinson network and beamformer chips are located on L1. Mechanically-drilled vias from L1 to L4 are used for antenna feedings. M1/M2 with Via12 are used to realize grounded coplanar-waveguide (CPW) lines for RF shielding. Note, as the phased array oper-

13
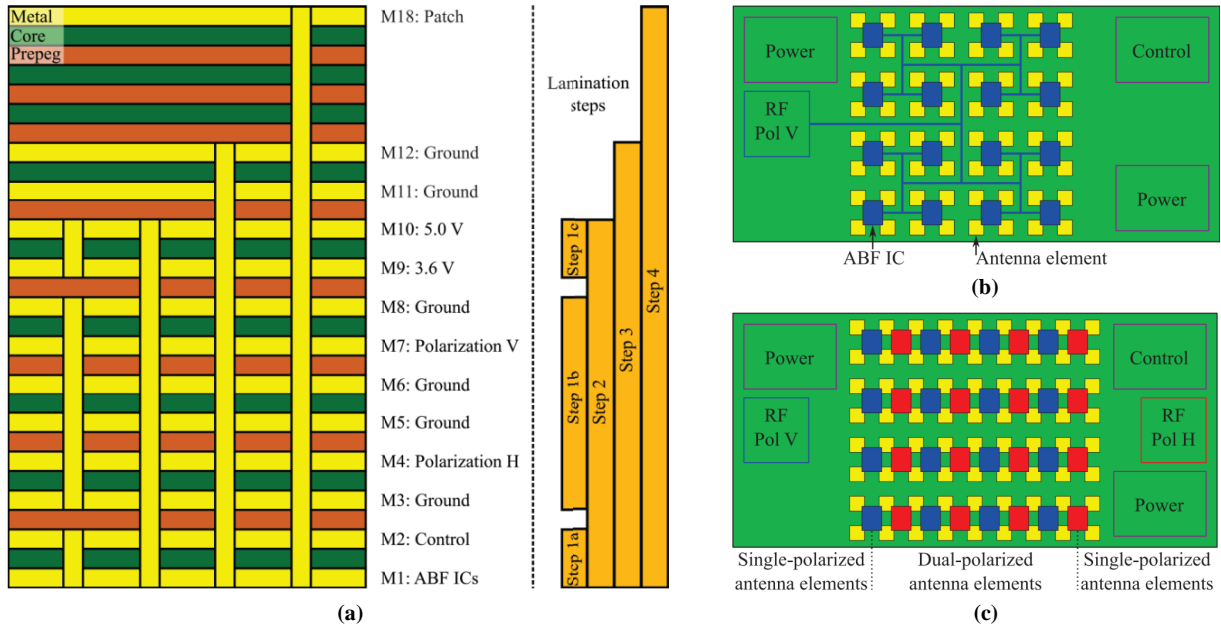
Figure 2.5: (a) 18-layer PCB stack-up. (b) Sketched 8×8 PCB phased array layout with beamformer chips for the vertical polarization only. (c) Sketched 8×9 PCB phased array layout with beamformer chips for both polarizations. [6]
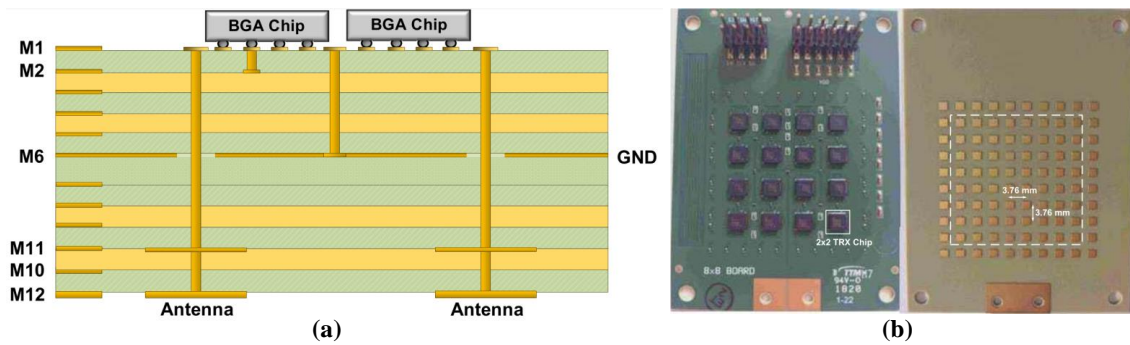
Figure 2.6: (a) Stack-up of low-cost 12-layer PCB board. (b) Front and back views of 39 GHz 8x8 phased array. [7]

ates at Ku-band, the $\lambda/2$ antenna spacing is relatively larger than the size of the beamformer chips, providing more space for RF routing. Since the PCB only has 4 layers to accommodate antenna feeds, Wilkinson network, power, bias, and digital signal routing, some of the routings for digital signals may share the same layer as the antenna patches. Extreme care must be taken to minimize RF interference. For example, ground vias (Via34) are placed around each microstrip antenna to reduce the coupling between antenna elements [5]. A similar 4-layer PCB stack-up was also successfully implemented on a 28 GHz linear-polarized phased array design in [36].

Work out of Eindhoven University of Technology [6] and the University of California [7] proposes more complicated multi-layer laminated PCB stack-ups compared with the previous design. A design for an 8×8 dual-polarized phased array centered at 28 GHz with 18-layer PCB stack-up is introduced in [6]. All the dielectric layers have the same thickness which creates symmetry and can minimize warpage of the PCB during fabrication. The antenna patches are located on M18 with M12 acting as the antenna ground. The remaining layers and their functions are shown in Fig 2.5 (a). The PCB was manufactured using six lamination cycles, as shown in the right side of Fig 2.5 (a). By using six lamination cycles, six different vias can be drilled as demonstrated by the vertical yellow bars. In Fig 2.5 (b) and (c), the sketched PCB layout of an 8×8 dual-polarized phased array is illustrated. The yellow squares represent the antenna patches; the blue and red rectangular shapes represent the beamformer chips for two different polarizations—vertical and horizontal. The sketched PCB layout for vertical polarization is shown in Fig 2.5 (b). Here, each beamformer chip is located at the center of each 2×2 sub-antenna array, and its Wilkinson network is indicated by the blue traces (placed on L7). Since a beamformer chip only has four channels, each beamformer chip can feed only one polarization of a 2×2 sub-array. Therefore, another set of beamformer chips (in red) is interleaved with the blue beamformer chips for feeding the horizontal polarization [seen in Fig 2.5 (c)], with the corresponding Wilkinson network routed on M4. However, due to the interleaved placement of beamformer chips, not all 64 elements are dual-polarized—it is not possible to connect the left-most column of antenna elements with the right-most column of beamformer chips without using complicated feeding routing. Therefore, an additional column of antenna elements is added to the right, creating an 8×9 antenna array. In this case, the outer left and right columns are only fed by one polarization, and the inner antenna array is dual-polarized. Moreover, the array is scalable only in the vertical direction when using this proposed arrangement because the two Wilkinson networks supporting the two different polarizations occupy space in the horizontal direction.

Another 8×8 linear-polarized phased array operated over the frequency band of 37-42 GHz was designed with a 12-layer PCB stack-up, as proposed in [7]. The stack-up and the low-cost PCB for 8×8 linear-polarized phased array prototype is shown in Fig 2.6 (a) and (b). A 1-to-16 Wilkinson network with 0201 resistors and 16 2×2 channel beamformer chips are located on M1. Power and digital signal routing are located on M3-M5. The stacked-patch antenna elements are located on M10 and M12 with M6 acting as the antenna ground. This PCB stack-up is completely symmetrical and only needs two laminated cycles for fabrication. The first lamination is to build M1-M6 and M7-M12, and the second lamination is to stack two sub-blocks together to form a single PCB. The types of vias shown in Fig 2.6 (a) are also easy to fabricate, the mechanical via from M1 to M6 can be drilled during the first lamination cycle, while the M1-M12 mechanical via can be drilled during the second lamination cycle.

Besides traditional multi-layer laminated PCBs, there is another fabrication process named HDI. With this approach, it is possible to achieve layer-by-layer processes with available microvias on each layer, bringing more flexible via connections between multiple layers. The stack-up of HDI boards is usually defined by the formula $i+N+i$, where N represents the number of layers in the inner core and i represents the number of sequential lamination steps needed in the PCB fabrication [8]. Fig 2.7 shows an example of a $2 + N + 2$ HDI stack-up: the dark green layers are core material, the light green layers are prepreg material, and the orange bars are different types of vias. The buildup process is as follows. An N-layer section known as the inner core is built to start and the N-layer mechanical via is drilled through the entire core directly. Then, two laminations are added sequentially on the top and bottom sides of the N-layer core. The via shown in these two sequential laminations are microvias, which are also known as laser-drilled microvias. Note, the mechanically-drilled via in the N-layer core can be aligned with the microvias to make more connections possible between the inner/outer layers. Also, another through-hole mechanical via can be drilled from the top layer to the bottom layer during the final stage as shown on the right side of Fig 2.7. Theoretically, N and i have no limitations; however, PCB fabrication companies usually have typical standards and restrictions. For example, the number of possible inner layers depends on the overall PCB thickness and the number of outer laminated layers; a larger i means more sequential lamination cycles which increases the cost and fabrication difficulty [8].

Instead of mechanically-drilled vias, there are two common microvias that are used in HDI PCBs—stacked and staggered microvias, as shown in Fig 2.8 (a) and (b). In general, microvias have a small minimum diameter requirement compared to
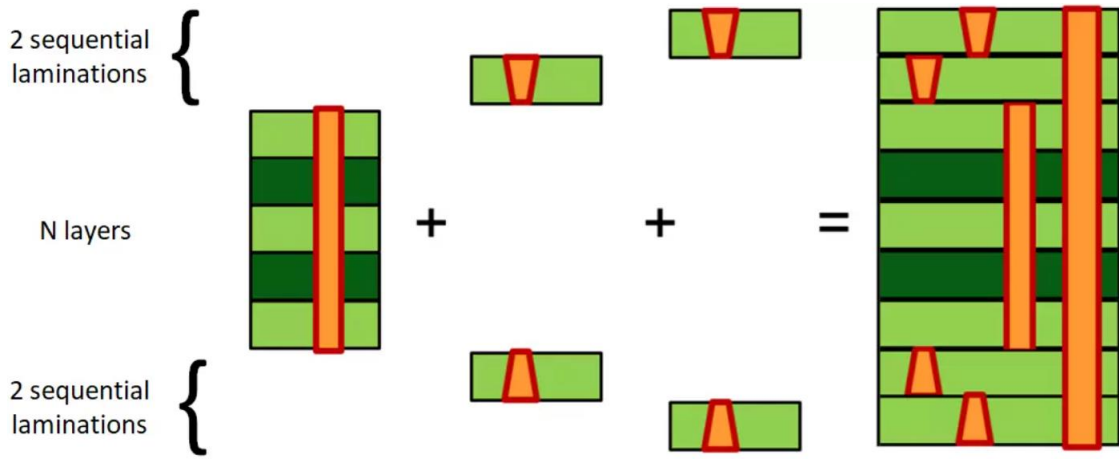
Figure 2.7: Structure of a 2+N+2 HDI stack-up. [8]
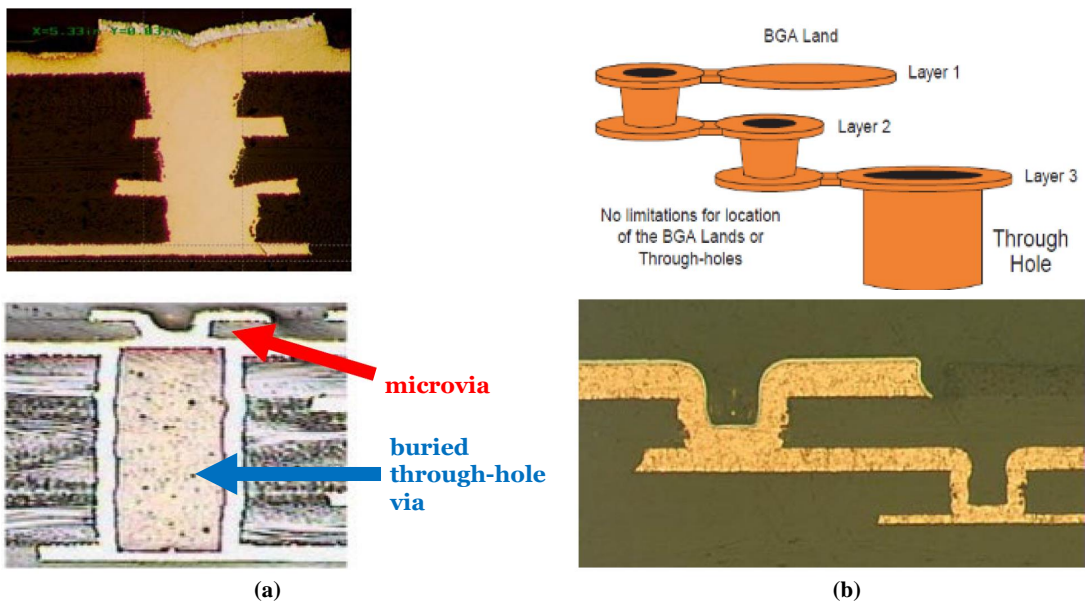
Figure 2.8: Cross-sectional microscope images of (a) stacked and (b) staggered microvias. [9]

mechanically-drilled vias, which is a great option for fitting them into tight areas on PCBs, assuming that the aspect ratio requirement can be met. In Fig 2.8 (b), staggered microvias are an alternative to the stacked microvias, with offsets between the placements of microvias in each successive layer [37]. Although the microvias bring flexibility in terms of connections, there are still a few aspects that must be considered. In the microscope images of stacked and staggered microvias presented in Fig 2.8 (a) and (b), it is clear that the accuracy and tolerance of fabricated microvias compared to the ideal microvias of simulations show non-negligible variation. These fabrication errors and tolerance will bring a lot of unexpected parasitic effects to RF matching and may result in a significant difference between simulation and measurement results.

Overall, the advantages of HDI boards are obvious and flexible connections between layers can be achieved by combing multiple microvias with the inner core vias. Moreover, since each sequential lamination cycle will stack one layer from the top and one layer from the bottom at the same time, the warpage of the PCB is minimized. However, due to the different technologies for drilling mechanical vias and microvias, microvias will cause more parasitic impedance and their tolerance and variation are typically larger than mechanical vias. Thus, stacked microvias are not suggested for feeding RF signals. Comparing HDI to the traditional laminated PCBs, the advantages and disadvantages of each manufacturing process are summarized and listed in Table 2.1.

	Multi-layer laminated PCB	**HDI PCB**
Pros	Multiple types of mechanical-drilled vias	Flexible via connections
	More accurate via transitions	Symmetrical stack-ups
Cons	Stack-up must follow the lamination logic	Less accurate via transitions
	Cost highly depends on lamination cycles	

Table 2.1: Multi-layer laminated PCB vs. HDI PCB

2. **Flip-chip ball grid array (BGA) packages and antenna-in-package (AiP)**: Aside from PCBs with flip-chip solutions as discussed above, there are several other technologies capable of realizing the packaging for mm-wave active beamforming arrays, including low-temperature co-fired ceramics (LTCC), high-temperature co-fired ceramics (HTCC), liquid crystal polymer (LCP), and standard organic packages.
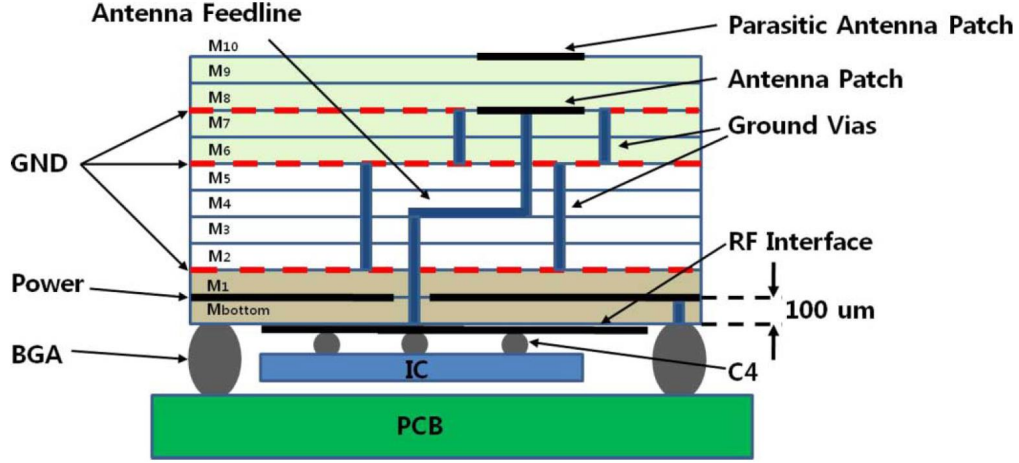
Figure 2.9: Structure of flip-chip BGA antenna package. [10]

LTCC is one of the most popular technologies for fabricating antenna-in-package (AiP) and system-in-package (SiP) solutions. The approach starts with printing different conducting circuits on each ceramic substrate foil or tape, and then all the printed tapes are laminated and fired together in one stage [38]. Because of this special manufacturing process, it is possible to reach 50 laminated layers, and to embed passive components and integrated chips using wire-bonding in the substrate [39]. Thus, multiple RF front-end modules can be integrated into one piece of LTCC, minimizing the footprint of the system [40]. In addition, LTCC has advantages such as low path loss, fine traces, line width/spacing flexibility, and low thermal expansion. Since ceramic has the property of high thermal conductivity, it can be used in beamforming chips to dissipate the generated heat, in turn allowing the overall system to be more stable and robust in various operation conditions [41]. Ferro A6M-E and DuPont 9K7 are common substrates used in LTCC packaging that have been shown to have low losses (loss tangent ≈ 0.005) at frequencies up to 60 GHz [10], [42], and loss tangent ≈ 0.006 at frequencies above 150 GHz [43]. In particular, the printed GCWGs using Ferro A6M-E and DuPont 9K7 materials have shown measured attenuation per unit length of 0.4 dB/mm at 150 GHz, for both cases [43]. Therefore, LTCC packaging is preferred for applications operating in multiple frequency bands: Ka-band [11], [44], [45], [46]; V-band [39], [42], [47], [48], [49], [50], [51]; W-band and higher frequency bands [12], [38], [43], [52].

19
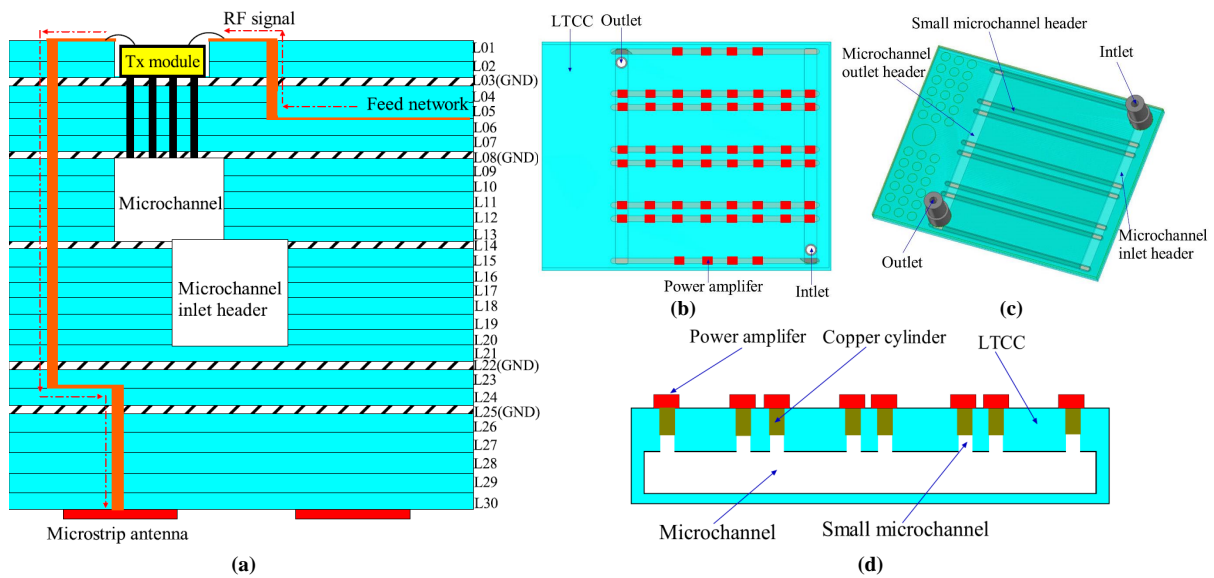
Figure 2.10: AiP with embedded heat sink. (a) LTCC stack-up. Structure of embedded micro-channel heat sink: (b) top view, (c) back view, (d) cross-section view. [11]
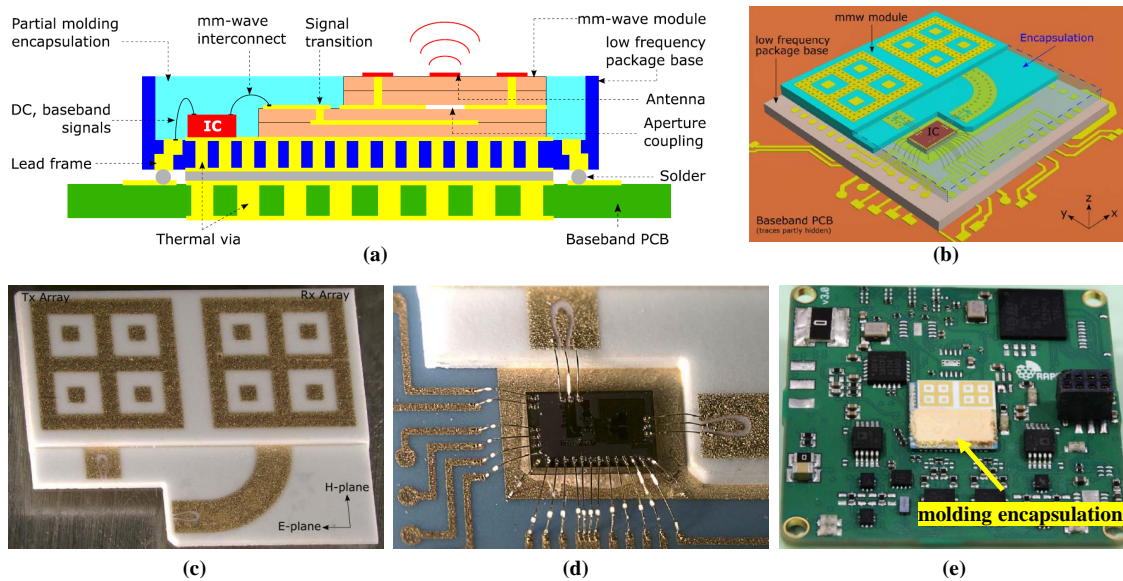
Figure 2.11: A 122 GHz radar SiP using LTCC. (a) Cross section. (b) Packaging structure. (c) Manufactured prototype of mm-wave module. (d) Wirebond interconnects between IC and mm-wave module. (e) SiP mounted on a baseband PCB. [12]

20

An example of a typical flip-chip ball-grid array (BGA) antenna package using LTCC technologies is shown in Fig 2.9. The function of each layer marked on the figure is similar to the traditional multi-layer laminated PCB stack-up. There are two sets of interconnections on the M_{bottom} layer. The first is the connection between antenna elements and the RF beamformer chip, achieved with the solder bump flip-chip assembly. The second is through the use of a set of BGA, connecting the digital and power signals from the LTCC package to a low-cost simple fabricated PCB. By using this method, a bulky and intense multi-layer board is split into two separate boards: one LTCC and one traditional laminated PCB. The LTCC board mainly contains RF feed-lines and transitions, while the power and digital signals are brought to a lower-cost, conventional flame retardant-4 (FR4) PCB that provides plenty of space to route. However, the design of interconnections in BGAs needs to be carefully and correctly simulated; any tolerance or fine defects will cause measurement errors.

Fig 2.10 shows an example of an AiP with embedded heat sink. In Fig 2.10 (a), the LTCC design contains 30 layers with the RF transmit module located on the cavity of L01 and L02, and the antenna patches located on L30. A micro-channel heat sink is embedded between L08 and L20 to cool the system as high-power amplifiers are used in the RF transmit module. There is a copper cylinder under each high-power amplifier as shown in Fig 2.10 (d) to conduct heat from the module to the micro-channel. Fig 2.10 (b) and (c) show the structure of the micro-channel. The coolant flows from the inlet header and shunts into eight small micro-channels. After this, the coolant combines and flows away from the outlet, thus taking the heat away from the module [11]. A SiP solution based on LTCC for frequencies beyond 100 GHz is shown in Fig 2.11. The structure of the proposed SiP in Fig 2.11 (a) and (b) contains both mm-wave and low-frequency modules. The radar chip is wire-bonded to the LTCC mm-wave module in Fig 2.11 (c) and the baseband PCB in Fig 2.11 (d). A molding compound fills in the open-cavity and covers the radar chip for encapsulation purposes [12].

3. **Surface-mounted antenna arrays**: Another antenna packaging solution, which is not widely used but has some interesting features, is called surface-mounted antenna arrays. The antenna elements or antenna arrays are packaged as passive components; the package only contains the antenna radiating elements and partial antenna feeding structures. In addition to the package, an adapter (mother) board is needed to connect the antennas and the active components (e.g., discrete phase shifters, PAs, beamformer chips), at the top and bottom sides respectively. This adapter board also provides a large amount of space for the routing of power, digital signals, and the
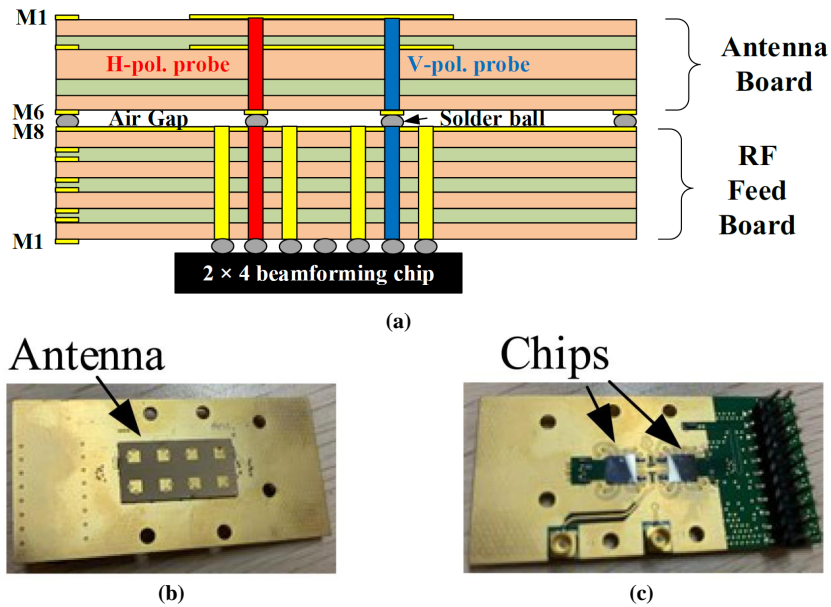
Figure 2.12: A 2×4 dual-polarized phased array at 28 GHz using surface-mounted antenna packaging. (a) PCB stack-up. (b) Top view of fabricated prototype. (c) Bottom view of fabricated prototype. [13]
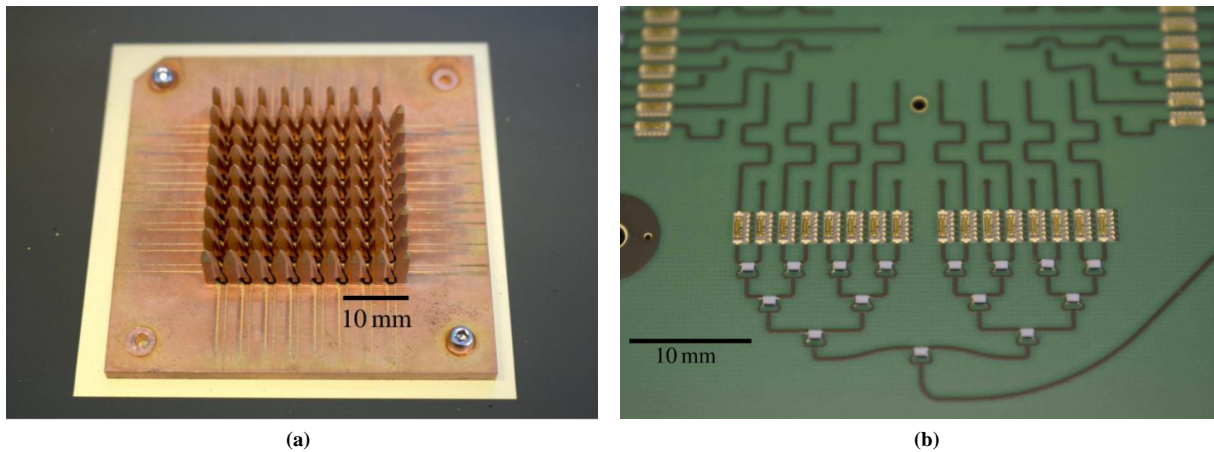
Figure 2.13: Photos of 8×8 dual-polarized Ka-band Vivaldi antenna array prototype. (a) Top view of connector-less aluminum Vivaldi mounted antennas. (b) Bottom view of attached phase shifters and resistors. [14]

remaining antenna feeding structures. Fig 2.12 displays a 2×4 dual-polarized phased array operating in 24.5-27.5 GHz frequency band that uses surface-mounted antenna packaging [13]. The packaging solution contains two separate PCB boards that are simple and inexpensive: one is a 6-layer antenna board, and the second is an 8-layer RF feed board (adapter board) with beamforming chip flipped onto the M1 layer, as marked on Fig 2.12. The connections between these two boards are made using pads and solder balls that create an air gap. The most significant issue noted by the authors is that the height of the solder balls and the air gap would strongly affect the antenna input impedance; it therefore must be considered in the antenna simulation [13]. However, even if such a design were carefully simulated, manufacturing accuracy and tolerance could still have strong effects on the measurement results.

Another interesting design using surface-mounted implementation is a Ka-band Vivaldi antenna array presented by Aalto University in Finland [14], [53], [54], [55]. A photo of a fabricated Vivaldi antenna array is shown in Fig 2.13. The Vivaldi antenna is known for its wide bandwidth and large beam steering range [14]. However, most implementations of Vivaldi antennas are 1×N linear arrays in the end-fire direction, where the beam steering range is significantly limited [53]. In the Aalto University papers, a 3D fully-metallic structure Vivaldi antenna array is developed. The array includes feed pins that can be connected to through-holes on PCB, with RF feeding lines routed within an 8-layer PCB using striplines and CPWGs. At the bottom of the PCB, the phase shifters and the resistors for the Wilkinson networks are soldered for beam-steering purposes. The 3D Vivaldi antenna array is able of covering the frequency range from 26 to 40 GHz based on the simulation results; however, the phase shifters that were used in this design can only support from 32 to 37 GHz. Thus, a beam steering range of approximately ±60° in the E and H -planes at both 32 and 37 GHz were measured [14].

4. **Wafer-scale and antenna-on-chip**: The highest integration level of antenna packaging is antenna-on-chip (AoC) or system-on-chip (SoC). The antenna elements and chips are co-integrated in silicon, with the antennas being fed directly through silicon. This minimizes the RF loss due to the feeding structures and interconnections significantly [56]. A group from UCSD proposed a wafer-scale beamforming array operates at 60 and 140 GHz, with intermediate-frequency (IF) input [15], [16], [57], [58]. Fig 2.14 shows a 2×4 wafer-scale phased array operated at 140 GHz with IF input signal at 9-14 GHz. The package contains the entire RF front-end. The input LO signal at 21-24 GHz is multiplied by a tripler to 63-72 GHz, and then a 1-to-8 Wilkinson network distributes the signals to doublers located at each channel. The
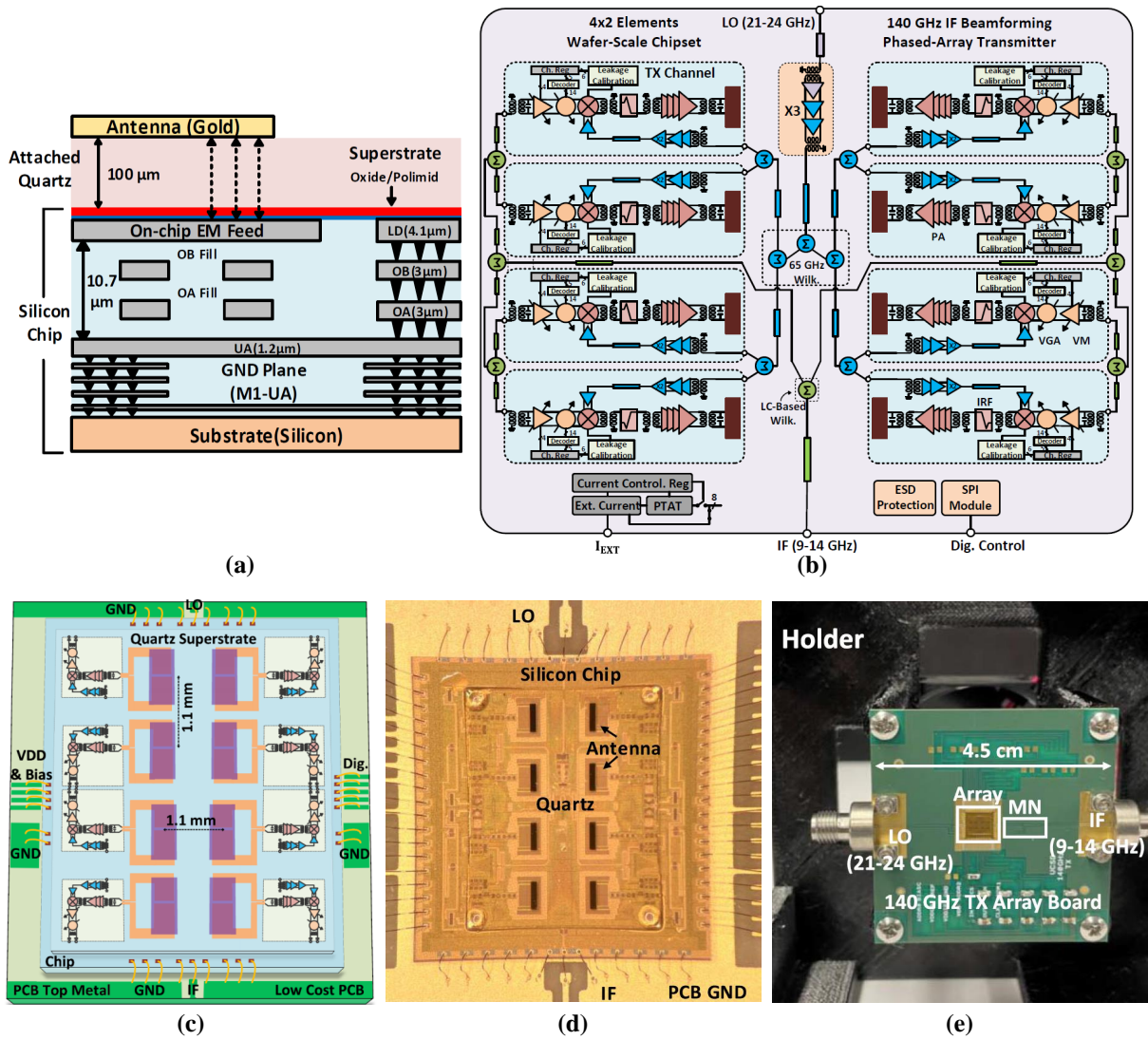
Figure 2.14: Design of 2×4 wafer-scale phased array operated at 140 GHz. (a) AoC stack-up. (b) Block diagram of proposed chipset. (c) Structural diagram of assembled system. (d) Die photograph of proposed chipset. (e) Chip wire-bonded on PCB. [15], [16]

IF signal is also distributed through a 1-to-8 Wilkinson network and followed by a 5-bit phase and 4-bit gain control circuit. Then, the eight mixers at each channel upconvert the IF signal to the targeted frequency band and a differential 4-stage transformer-coupled PA is connected to each antenna to achieve the required output power level, as shown in Fig 2.14 (b). The cross-section of the proposed chipset in Fig 2.14 (a) illustrates the interconnections between the antenna elements and the ICs. The antenna patches are attached to a 100 μm quartz substrate and the quartz substrate is then attached to the silicon wafer. The feeding structure of the antenna is proximity coupled which is located on the top layer of the silicon chip, and the remainder of the chip contains the integrated circuits such as transformer, low noise amplifier, and mixer. The authors also mention that the quartz-to-silicon attachment is a normal fabrication process and does not increase the cost, but there is an unavoidable air gap between the quartz and silicon due to manual assembly. Variation in this gap size would significantly affect the antenna center frequency and the radiation efficiency [59].

2.2.2   Recent Advances in RF Beamforming Array Calibration

RF beamforming arrays are critical constituents in mm-wave wireless communication systems. An important step before the phased arrays are deployed is calibration. An RF beamforming array contains multiple components such as antennas, PAs, phased shifters, variable gain amplifiers, switches, and power combing networks. Due to the temperature variation, drift over time, aging effects, and manufacturing tolerance, errors or failures can occur in each block and cause degradation of the overall system performance [60]. Amplitude and phase controls are the most common errors in practice, arising from phase shifters and variable gain amplifiers. These errors can cause serious inaccuracy of beam steering angles and radiation patterns. Therefore, it is necessary to employ calibration to compensate for the errors before operating the phased arrays.

The foundation of any calibration method is the feedback mechanism; a way to monitor the signals transmitted by each antenna element. Various feedback path approaches have been proposed in the literature, and they can be divided into two categories: external feedback calibration and self-feedback (internal-feedback) calibration. External feedback calibration means that the feedback path originates outside of the main beamforming array. Typically, a horn antenna is used at the far/near field as the receiver and the received signals are fed back to the antenna-under-test (AUT)/user for calibration or DPD purposes.
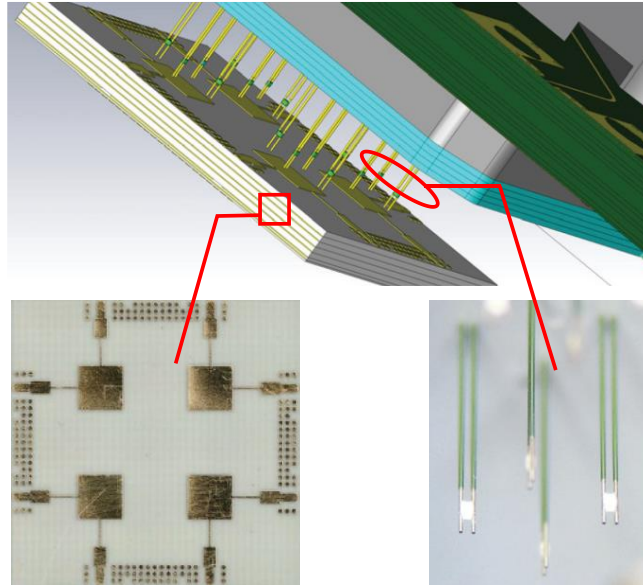
(a)
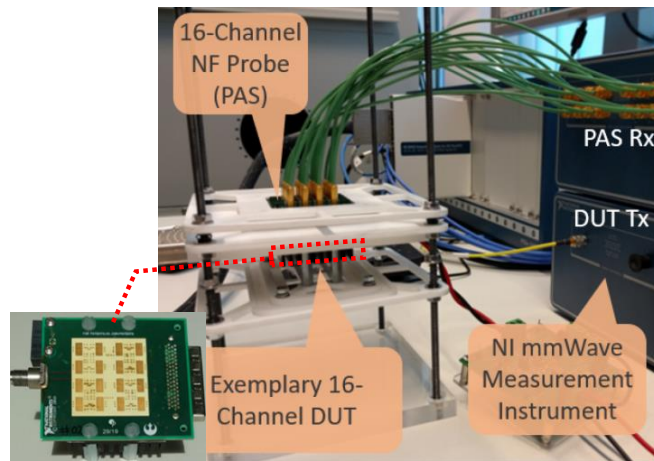
(b)

Figure 2.15: External near-field calibrations using: (a) transmission line probes [17], (b) Vivaldi antenna arrays [18].
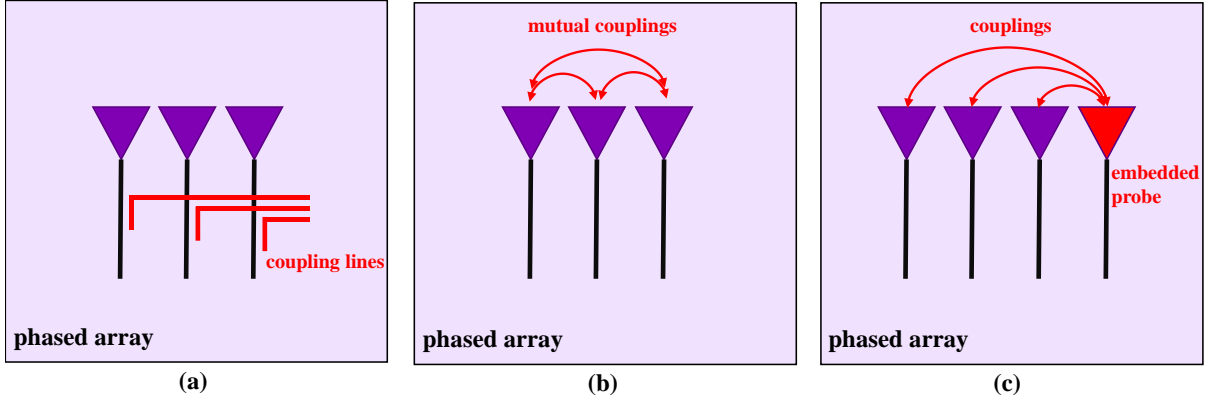
Figure 2.16: In-field calibration using: (a) coupled lines, (b) mutual couplings, and (c) embedded probe. [19]

Fig 2.15 (a) and (b) show two implementations of external feedback calibration. A 2×2 dual-polarized edge-fed patch array operating at 28 GHz with transmission line probes inserted in the near-field (NF), as shown in Fig 2.15 (a). The transmission line probes are designed to avoid affecting the antenna's impedance [17]. Four transmission line probes are placed at a distance of 0.27mm above each dual-polarized patch with the other side of the probe lines passing through a block of absorber and then connecting to a multi-layer PCB for receiving the feedback signals. Fig 2.15 (b) follows a similar design idea, where the AUT is a 4×4 linear-polarized phased array. The 16-channel NF probe antenna system contains four PCBs; each PCB having a 1×4 linear Vivaldi antenna array. The probe antenna system is placed 2 mm above the AUT and embedded in an absorber to reduce the coupling between antennas and stabilize the mechanical structures [18].

In terms of far-field calibration, the methods available are not always practical. For example, the base station is usually mounted on a cell tower or on the roof of a building and it is not feasible to bring the equipment on-site to do far-field calibrations. Therefore, in-field calibration methods have caught the attention of researchers as it does not require any additional far-field circuity or RF hardware for monitoring or observing. There are three main in-field calibration methods as illustrated in Fig 2.16 (a), (b), and (c). The following reviews the designs that implement one of these in-field calibration methods.

The idea of using embedded coupled lines as feedback paths is one of the most popular, having been implemented over a wide range of frequencies from sub-6 up to 100 GHz [19], [20], [21], [61], [62]. Examples of embedded coupled line on PCBs are shown in

27

(a)

(b)
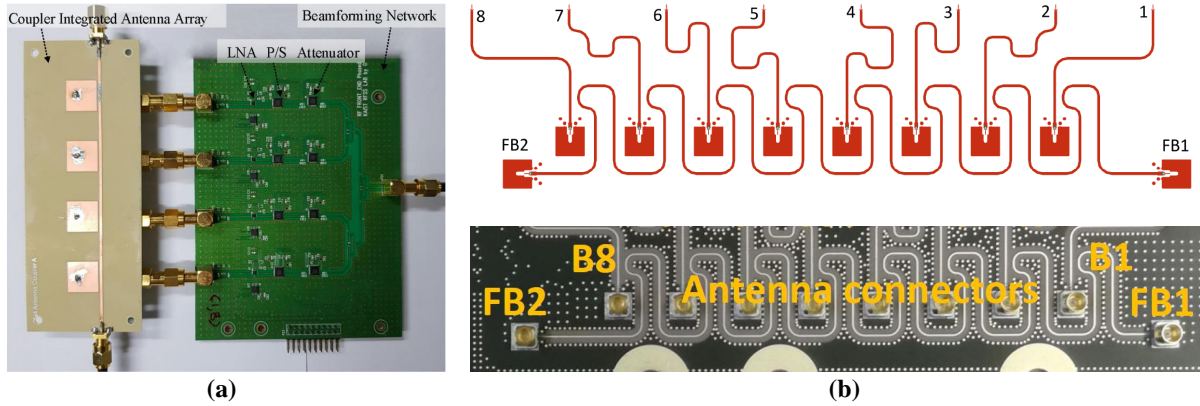
Figure 2.17: Embedded coupled line designs in PCB-based phased arrays. (a) A 1×4 linear microstrip patch phased array operating at sub-6 GHz [19]. (b) A 28 GHz transmit phased array with eight feed paths [20].

(a)

(b)
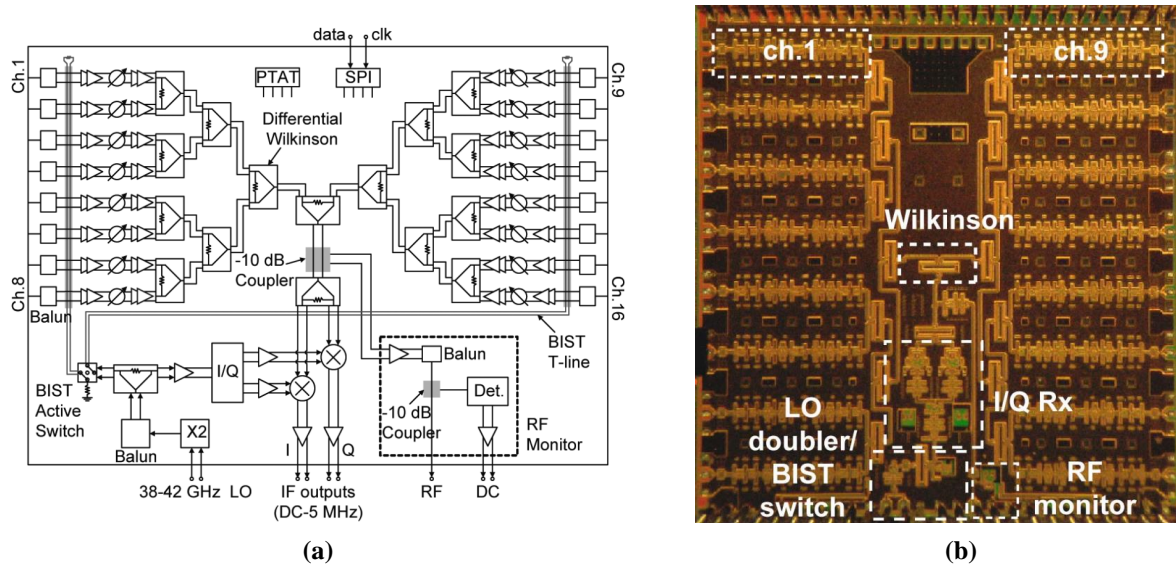
Figure 2.18: Embedded coupled line design in chip-based phased array. (a) Block diagram of chipset. (b) Fabricated chip micro-photograph. [21]

Fig 2.17 (a-b), with the on chip-level shown in Fig 2.18 (a-b). Fig 2.17 (a) is a 1×4 linear microstrip patch phased array with an integrated coupler from a group at KAIST, designed to operate at 5.8 GHz [19]. As shown in Fig 2.17 (a), the system contains two separate boards connected by RF connectors. The left board is for antenna elements and the proposed coupled line, and the right board is a beamforming board that contains discrete components such as LNAs, phase-shifters, attenuators, power combing networks, and other supporting circuits. The coupled line is placed close to the radiating edges of the antenna patches that are weakly coupled to the antenna array. The calibration signal is fed from one port of the coupled line while the other port is terminated. Then, the antenna elements are turned on one by one to receive the coupled signal and output to the spectrum analyzer. By analyzing the received calibration signals one at a time, the gain and phase difference deviation between channels can be captured and calibrated. Methods similar to embedded coupled lines are applied at higher frequency bands. A group from the University of Oulu proposed a Ka-band transmit phased array with a meandering microstrip line [Fig 2.17 (b)]. The microstrip line is routed next to each antenna feeding port to couple the signal from each antenna element. The antenna elements are built on a second PCB which is not shown in this figure and the boards are connected through sub-miniature push-on micro (SMPM) connectors [20]. The repeated shape of the meandering microstrip line maintains a similar coupling between the coupled line and each antenna element. The on-chip level design with built-in self-test (BIST) capabilities shown in Fig 2.18 (b) follows a similar idea as the previous cases. Differential couplers and transmission lines are used to couple the calibration signal to each phased array channel one by one. Afterward, the BIST signal down-converts to DC voltages through a homodyne I/Q mixer, the voltages being proportional to the gain and phase settings of each channel [21], [61].

The second in-field calibration method used is based on mutual couplings between certain antenna elements within a phased array. A group from Nokia Bell Labs proposed a large-scale multi-tile TX/RX phased array system at 90 GHz in Fig 2.19 (a), which contains 16 identical tiles with a total of 256 TX elements and 128 RX elements (marked in blue and green squares respectively). The feedback paths are generated between one TX element and one RX element from each tile while the remaining elements are off. The signal transmitted by the TX element couples to the RX element and feedback to the users. Note, the TX/RX pair selected should have a large spatial separation to minimize interference between pairs [22]. Although the paper proposed a DPD technique, the feedback solution can be applied for array calibration as well. A group from Tsinghua University proposed a modified beam-oriented DPD utilizing the over-the-air (OTA) diversity feedback in hybrid beamforming arrays [23]. As shown in Fig 2.19 (b), there are two transmit sub-arrays with a size of 1×3 placed in a line. The authors suggest placing two non-radiating elements to act
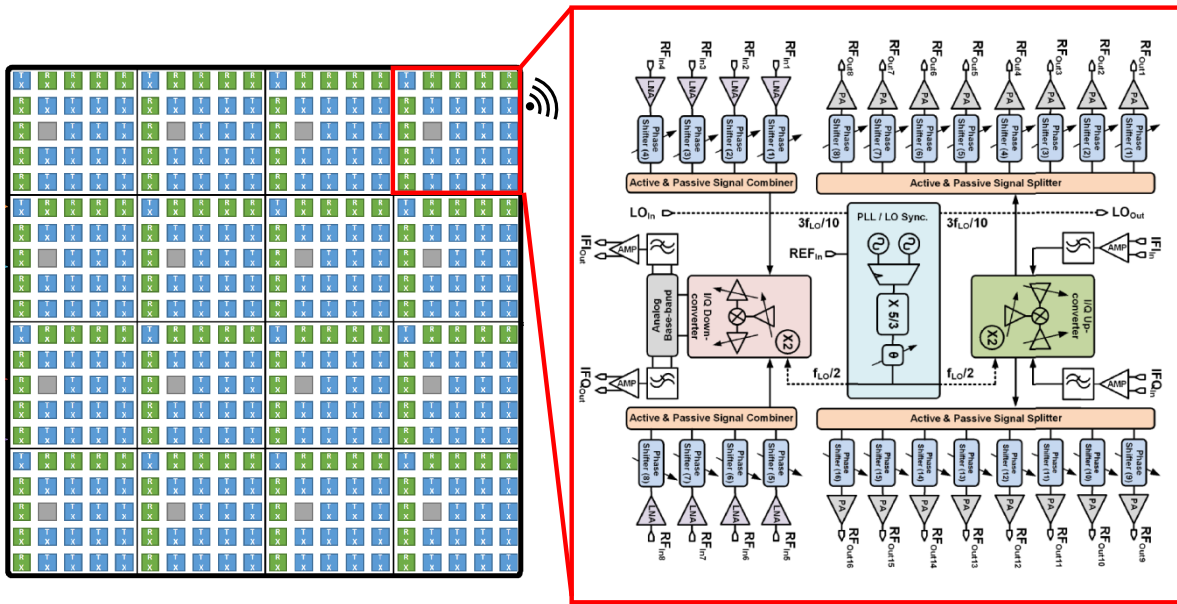
(a)
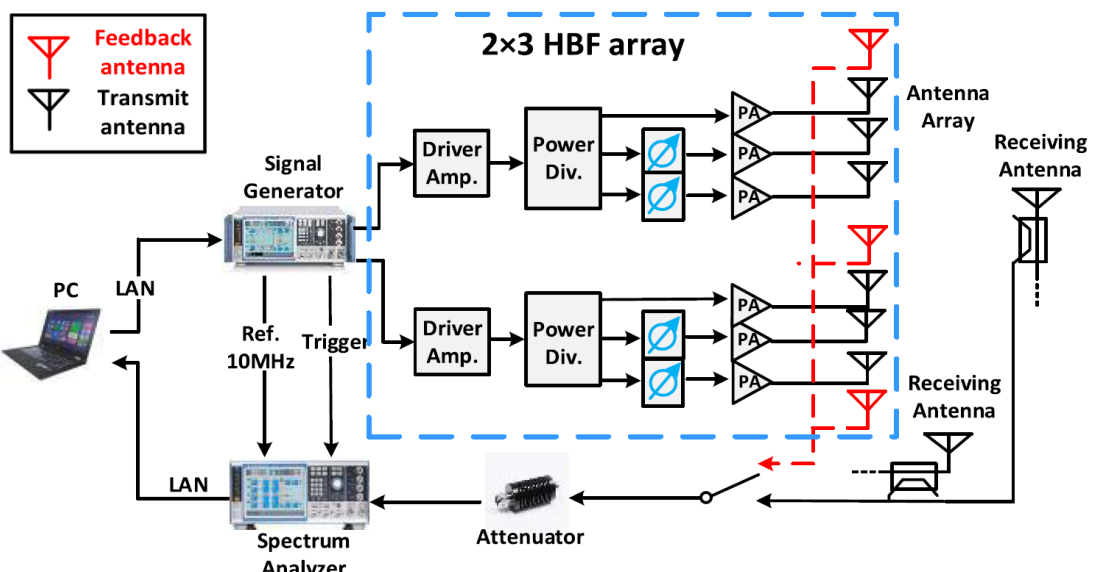
(b)

Figure 2.19: Phased array calibration through antenna mutual couplings. (a) Design from Nokia group [22]. (b) Design from Tsinghua group [23].
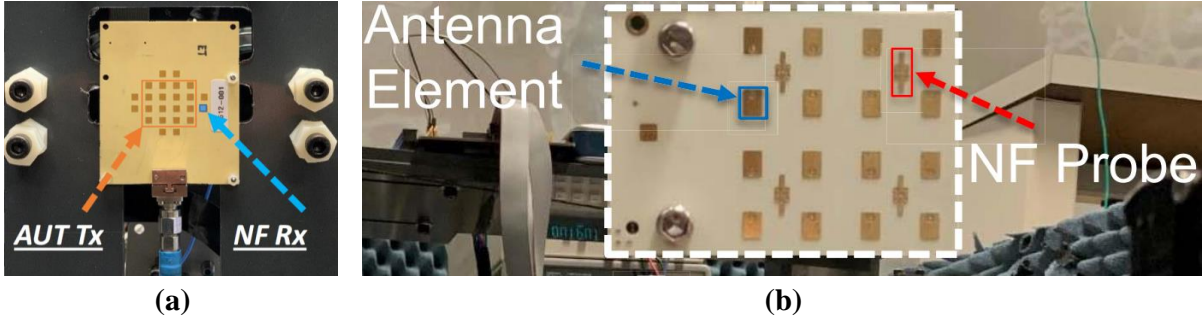
Figure 2.20: Designs of 4×4 linear-polarized beamforming arrays at 28 GHz with (a) embedded NF observation receivers at the array edges [24], (b) embedded NF observation receivers at the center of each 2×2 sub-arrays [25].

as two OTA receivers that are placed symmetrically within the radiating array for sampling the transmitted signals. Unfortunately, due to hardware limitations, there is no further verification based on a larger-scale AUT. In addition, based on the theoretical derivations, the authors assume the coupling coefficients between the OTA receivers and each transmit antenna element are appropriately the same. However, the coupling coefficients are based on the relative locations of the OTA receivers and the orientations of each antenna element. The observation receivers would see each antenna element differently, thus the couplings (magnitude and phase) between each observation receiver and antenna elements cannot be the same in practice, even within a small-sized array.

A larger scaled phased array with embedded observation receivers was proposed by the EmRG group from the University of Waterloo, as shown in Fig 2.20 (a). Here, the authors embedded eight NF observation receivers at the edges of a 4×4 phased array to collect the AUT's transmitted signals [24]. Similar to the last approach described above, however, this design did not overcome the issues of different magnitudes and phases between the embedded observation receivers and the antenna elements. The same group at the University of Waterloo also came up with a novel idea that did solve the issue of different coupling magnitudes and phases. Fig 2.20 (b) shows the novel NF probe structure that can be embedded into the main phased array without disturbing its radiation pattern. These uniformly distributed NF probes are placed at the center of each 2×2 sub-array, and are capable of capturing the signals transmitted from the main phased array and feeding them back to the digital signal processor for monitoring and improving the main phased array's performance [25]. However, these NF probes are operated at 28 GHz and can only be used in linear polarized phased arrays.

31

2.3 Discussion

Based on the literature review in Section 2.2, several trends and trade-offs can be observed:

- RF beamforming is the most popular architecture for mm-wave active phased antenna arrays in the literature due to its compact circuitry and functional blocks. In addition, the fabrication cost and power consumption of this architecture are the lowest when compared to other beamforming architectures.

- There are various packaging solutions for phased antenna arrays. One of the key decision factors is the operating frequency. For systems operating at or below Ka-band, most packaging solutions are PCB with flip-chip interconnection. For systems operating between Ka-band and sub THz, antenna-in-package and antenna-on-chip packaging are used as the system size gets smaller at higher frequencies. Moreover, the fabrication cost of these packaging technologies increases as the system-level integration rises. Therefore, the simple mechanism and relatively low cost of PCB-based packaging solutions have made PCB-based phased antenna arrays more attractive.

- NF calibration with an embedded feedback path is desirable for beamforming arrays. NF calibration is an alternative method to far-field calibration that does not require additional setups in the far-field and is possible to achieve in practice. The feedback path is embedded within the beamforming array which simplifies the calibration setups. Furthermore, the feedback path is designed together with the main beamforming array, guaranteeing the performance of the main beamforming array will not be affected by the built-in probing antenna structure.

In conclusion, this thesis will propose a new design of beamforming array with embedded NF probing antenna for array calibration and DPD training, able to operate at n260 band. The proposed NF probing antenna will be suitable for use in dual-polarized phased arrays as well. At the time of writing, no other solution has been proposed in the literature.

Chapter 3

39 GHz RF Beamforming Array Design with Embedded NF Probing Antenna

Based on the discussions in the previous chapters, it would be desirable to design an RF beamforming array with embedded feedback path to enhance array performance through array calibration and DPD training, using the most suitable packaging solution for Ka-band phased antenna arrays of a multi-layer laminated PCB with flip-chip interconnections. Unfortunately, trade-offs between antenna array design and fabrication limitations are unavoidable. However, an optimized solution is found and proposed in this chapter.

3.1 Design Objectives

The design objectives of each component, and of the beamforming array as a whole, are listed below:

1. PCB stack-up: The PCB stack-up must be designed to accommodate a flip-chip assembly for the beamforming IC and provide sufficient layers and structures to support functionalities such as RF signal routing and shielding, power delivery, and digital control signal daisy chaining and interfacing.

2. NF probing antenna and phased antenna array integration: The two structures must be co-designed and co-optimized to ensure that:

- The coupling magnitude between each NF probing antenna and its surrounding antenna elements should be greater than the coupling to the rest of the array, and this magnitude delta should be as big as possible.

- The coupling magnitude and group delay are relatively constant across the design frequency.

- The addition of the NF probing antenna to the antenna array does not negatively affect the array's beamforming performance.

3. Array size: The array should be scalable; while this design targets 16 elements (to keep the array size feasible for its purpose), the design size is not limited.

4. Mechanical considerations: In addition to the main array, any surrounding logistic components (e.g., digital signal interfacing, power delivery, thermal management, mechanical housing) must be included in the design process as well.

The beamforming IC (MMW9003KC) from NXP Semiconductors was selected for use in this design. This beamforming IC operates from 37.1 to 40 GHz and contains four transceiver (TRx) channels with one RF input that can be connected to four antenna elements for linear-polarized operation. The IC requires two supply voltages and is controlled using a high-speed serial-peripheral interface (SPI).

3.2   PCB Stack-up and Design Constraints

A multi-layer laminated PCB stack-up is based on the logic of lamination cycles; any stack-up design that fails to follow such logic cannot be fabricated. A multi-layer laminated PCB stack-up consists of multiple sheets of substrate (core) and pre-impregnated (prepreg) material, the core and prepreg being pre-fabricated from the same material but having different properties and functionalities.

The core usually comes with copper foils attached to it and the prepreg is made from substrate impregnated with resin. The prepreg is softer than the core; therefore, it plays an important role in bonding cores together to achieve a multi-layer stack-up. The sheets are grouped and pressed in a certain order. Fig 3.1 shows three examples of sheet grouping that can be achieved by a single lamination cycle. Fig 3.1 (a) is the most fundamental unit of the core material, having two copper foils pressed to the top and bottom of the core
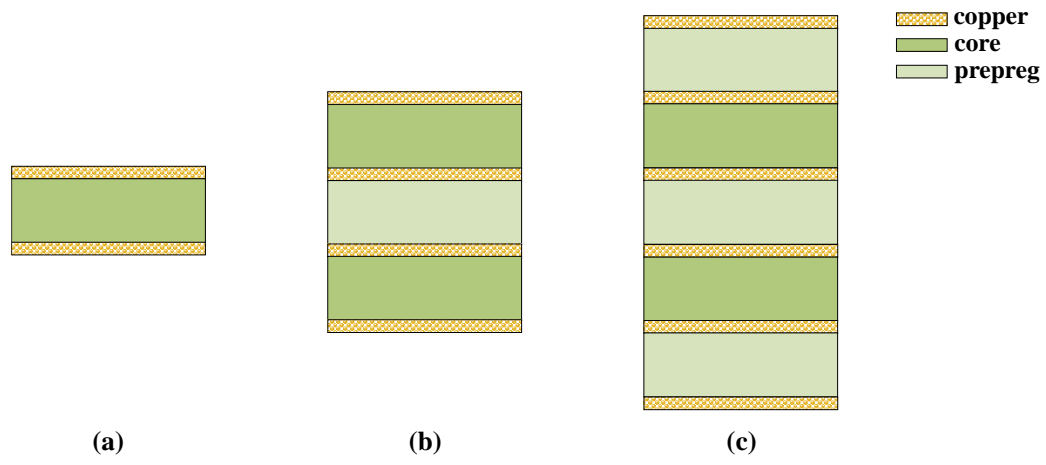
Figure 3.1: Three examples of sheet grouping achieved with first lamination cycle. (a) Unit of 2-layer PCB stack-up. (b) Unit of 4-layer PCB stack-up. (c) Unit of 6-layer PCB stack-up.
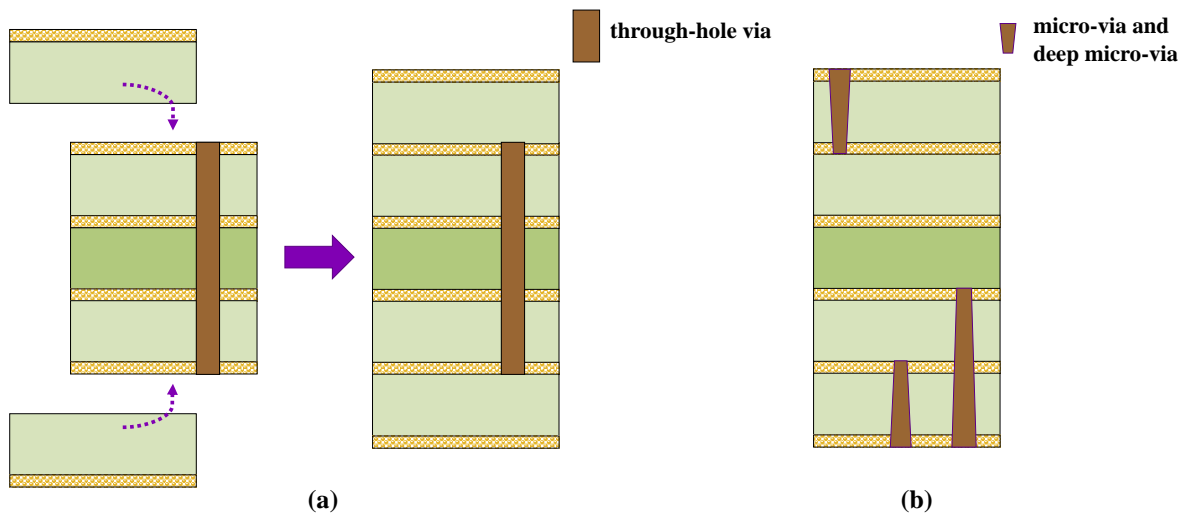
Figure 3.2: Build process of (a) blind via, (b) micro-via and deep micro-via.
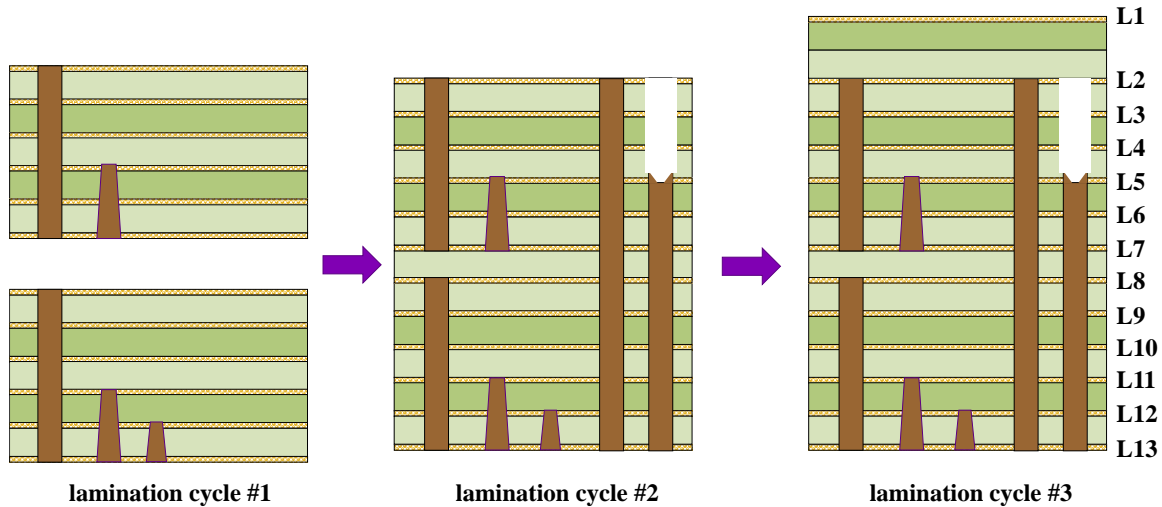
Figure 3.3: Proposed 13-layer multi-laminated PCB stack-up with three lamination cycles. [26]

(one to each). Fig 3.1 (b) and (c) are more complicated units with multiple sheets of core and prepreg pressed together.

In terms of drilled vias, there are multiple types that can be produced in a multi-layer laminated PCB stack-up. The most commonly used vias are through-hole, blind, micro, and deep micro. A through-hole via is also known as a mechanically-drilled via, as it is drilled from the top layer to the bottom layer directly. For example, a through-hole via can be built on the stack-ups shown in Fig 3.1 (a)-(c), as long as the via size follows the aspect ratio required by manufacturers. Blind vias, also known as buried vias, require more than one lamination cycle to build. The build process of a blind via is demonstrated in Fig 3.2 (a). Here a through-hole via is drilled during the first lamination cycle #1 and then, during the second lamination cycle when another layer of prepreg is stacked on both the top and bottom of the first lamination block, the previously through-hole via is buried in the stack-up to become a blind via. Fig 3.2 (b) shows the structures of a micro-via and a deep micro-via. A micro-via crosses one layer from the top or bottom layer, while a deep micro-via can cross more than one layer. Currently, the maximum number of layers a deep micro-via can travel is limited to two due to laser drilling technology hardware limitations. Note, that both a micro-via and deep-micro via can be drilled during any lamination cycle; they can also be buried in the stack-up to become blind vias.

36

Another type of via which is less commonly used as it incurs additional fabrication costs is a back-drilled via. A back-drilled via, as shown in the right-most via in Fig 3.3 lamination cycle #2, is a special type of via that requires advanced drilling technology. To create a back-drilled via, a through-hole via is drilled to connect the top and bottom layers, however, as a connection from only one of the middle layers to the bottom layer is desired, secondary drilling (represented as a white bar in Fig 3.3) is done to drill out a few layers of copper while leaving the remaining conductive via plating. While back-drilled vias provide flexibility in layer connections, there are several drawbacks that must be considered, specifically in regard to carrying RF signals. In general, the drilling tools used have sharp tips that provide high pressure for easy thrust. However, this may result in some copper residue, leaving the resultant via not as clean as would be ideal. In addition, it is difficult to maintain high accuracy in the depth control of the secondary drilling; under-drilling or over-drilling causes additional parasitics for RF circuits, affecting their matching performance [63], [64]. Another crucial restriction of using back-drilled vias is the via-to-copper clearance, which should always be kept in mind when designing an EM model. In order to drill out the unwanted copper in the through-hole via, the size of the secondary drilling tool should be slightly larger than that used to drill the through-hole via. In every layer the secondary drilling passes through, a minimum clearance must be maintained between any signal traces, pads, and the back-drilled via; if it is not, the secondary drilling could drill out those circuits and destroy the original design. This is sometimes overlooked during design and simulation stages where traces could accidentally be placed intersecting the to-be-drilled areas.

A 13-layer multi-laminated PCB stack-up is proposed for this project [26]. Such a complicated stack-up was designed to accommodate not only the antenna elements but also the RF beamforming ICs. Fig 3.3 illustrates the build process of the 13-layer stack-up with three lamination cycles. In lamination cycle #1, two 6-layer grouped sheets are laminated at the same time and though-hole vias, micro-vias, and deep micro-vias are drilled. In lamination cycle #2, one layer of prepreg sheet is sandwiched between the two stacked blocks from lamination cycle #1, and though-hole vias and a back-drilled via are drilled after the second lamination. In the final lamination cycle, one additional layer is laminated on the top, which is designated for the antenna patches with proximity-coupled feeding structures.

The substrate used in this design is Isola ASTRA MT77 which is characterized by a dielectric constant of 3 and loss tangent of 0.0017 [65], [66]. The antenna elements of the proposed array use a proximity-coupled feed structure, where the antenna patch is located on L1, its microstrip feed line is on L2 and L5 is the antenna ground. The RF beamforming ICs are placed on L13. L8 and L9 are two power planes for two voltages.

37
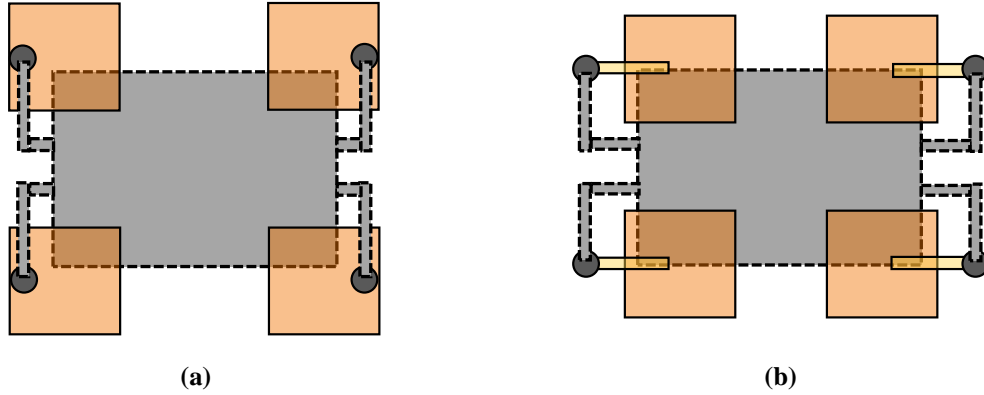
Figure 3.4: Two possible solutions for beamforming IC routing constraints using: (a) probe feed antenna structure, (b) proximity-coupled feed antenna structure.

L10 and L11 are used for digital signal routing. L7 and L12 are RF grounds. One of the most important considerations in RF design is isolation, as at such high frequencies any interference will degrade the overall RF performance. Thus, the functionality of each layer must be determined based on optimal EM performance such that the isolations between RF traces, power planes, and digital signal routing are maximized. In order to achieve maximum isolation in the proposed design, a ground plane has been placed below the antenna ground and above the power planes on L7. This strengthens the isolation between the antenna elements and power/digital traces. Another ground plane (L12) is placed between the RF beamforming ICs and the power/digital layers—this is a mandatory ground to ensure the performance of the beamforming ICs. To illustrate this point, consider the PAs located inside the beamforming IC. The drain of the PA is connected to a DC voltage which is connected to L8 and L9 in the proposed design. If the PA output signal somehow leaked to the biasing voltage, oscillation would occur, affecting the RF beamforming IC's performance.

The beamforming IC footprint is the most crucial limitation in phased array designs. The layouts and routing of beamforming ICs play an important role in overall array performance because all the signals spread out from such tiny areas. Because of this, isolation between different signals, grounding, and shielding vias must be maximized at the interface of the IC bumps. Each beamforming IC has a size of 4.39 mm × 3.59 mm, and the ideal antenna spacing at 39 GHz is 3.9 mm. This means an ideal 2×2 antenna grid size should be 3.9 mm × 3.9 mm. However, it is obvious the IC footprint size would deviate from the ideal 2×2 antenna grid size if a probe-feeding antenna structure is being designed as, with-

38

out taking alternative measures, the footprints of through-hole vias would intersect with the beamforming IC footprints. The author explored two potential solutions as illustrated in Fig 3.4. One alternative was to increase the antenna spacing such that the IC footprint could fit under the antenna grid [Fig 3.4 (a)]. This solution relaxes the routing challenges between the IC footprint to the antenna patches, however, the radiation pattern would significantly degrade since larger antenna spacing results in larger grating lobes. The second option explored Fig 3.4 (b) was to use proximity-coupled feeding structures such that the feeding position could be extended out of the 2×2 antenna grid. This feeding structure provides better isolation between the RF signal feedings and other signals emanating from the beamforming ICs as the feeding lines are far away from the IC footprint. This approach creates enough routing area for ground shielding. Moreover, the proximity-coupled feeding structure provides wider bandwidth due to its intrinsic properties. However, the trade-off when using this structure is the increased complexity of antenna routing designs and PCB stack-up.

After considering the options, the proximity-coupled feeding structure was selected for this project and lamination cycle #3 was added to implement this structure [Fig 3.3]. Unlike the probe-feeding structure, the antenna patch does not require a direct connection with the feeding probe, instead, a certain distance must be maintained between the antenna patch and the feeding structure. Therefore, the antenna patch is located on L1 and its microstrip feed line is on L2, with L5 being the antenna ground. The through-holes (L2-L13) drilled during lamination cycle #2 are used as antenna feeding vias, and a coplanar waveguide (CPWG) transmission line is routed for connecting antenna feeding to the IC bumps with L12 as the RF ground. The antenna ground is built using back-drilled vias from L5 to L13. As mentioned earlier, the back-drilled vias are not as accurate as mechanically-drilled vias (due to the fabrication process) and should not be used to carry RF signals [63], [64]. In the current design, all back-drilled vias are used for grounding purposes, which minimizes the effects of non-ideality and inaccuracy during the fabrication process.

3.3 Design of RF Beamforming Array with Embedded NF Probing Antenna

As discussed in Section 2.2, an NF probing antenna capable of providing the feedback signal path necessary for carrying-out array calibration and DPD training is desirable.
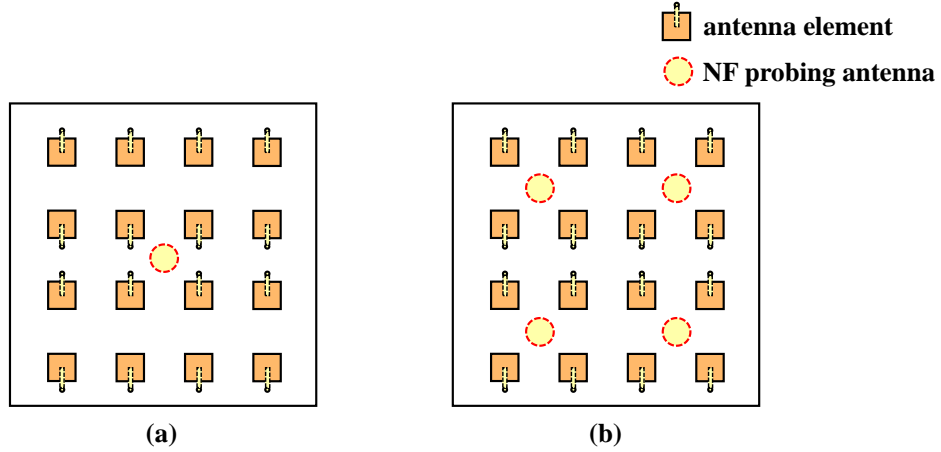
Figure 3.5: Two possible allocations of NF probing antenna(s) within a 4×4 phased antenna array. (a) One NF probing antenna is located in the center of the 4×4 phased antenna array. (b) Four NF probing antennas are equally distributed among the 4×4 phased antenna array, where each NF probing antenna is placed at the center of each 2×2 sub-array.

Specifically, the NF probing antenna should be designed to provide flat coupling magnitudes and a constant group delay to its surrounding antenna elements.

There are four design tasks which will be addressed and solved in this section:

1. Allocation of NF probing antenna(s) within a 4×4 phased antenna array.

2. Unit-cell antenna element.

3. NF probing antenna structure.

4. Transition of NF probing antenna.

Fig 3.5 (a) and (b) demonstrate two possible allocations of NF probing antenna(s) within a 4×4 phased antenna array. In Fig 3.5 (a), only one NF probing antenna is located in the center of the 4×4 phased antenna array, while in Fig 3.5 (b), the 4×4 phased antenna array is divided into 4 sub-arrays with a size of 2×2, and an NF probing antenna is placed at the center of each sub-array. Comparing the two possible allocations, it is clear the solution in Fig 3.5 (a) requires fewer NF probing antennas, which minimizes the massive transition designs. However, the coupling magnitudes and group delay between the NF probing antenna and the 16 antenna elements differ as the distance to the center 4 antenna

Figure 3.6: (a) Side view of proposed transition for NF probing antenna. (b) Block diagram of 4×4 linear phased antenna array with proposed embedded NF probing antenna and its routing solution.

elements is smaller than the distance to the remaining 12 antenna elements. The coupling strength between the NF probing antenna and the closest four antenna elements will be greater than those with the further antenna elements. In terms of the second allocation arrangement examined, even though it requires more NF probing antennas and increases the complexity of the feedback signals' transitions, the coupling magnitudes and phases between the NF probing antenna and its adjacent four antenna elements in each 2×2 sub-array are almost identical. It should be noted that the flatness of coupling magnitude and linear phase response are key design parameters for an NF probing antenna. Another key consideration for NF probing antennas is keeping the footprint as compact as possible as the antenna spacing of mm-wave phased arrays is small compared to that of phased arrays at sub-6 GHz. Thus, an NF probing antenna design with an optimized size that can cope with the constrained spacing between the antenna elements is desirable. Furthermore, a phased antenna array with an NF probing antenna distribution capable of scaling up to any larger-sized array without sacrificing any design parameters would be ideal. In conclusion, the solution presented in Fig 3.5 (b) was selected for the proposed design.

As the NF probing antennas will be embedded within the main phased antenna array, the layer for the NF probing antenna structure should be determined as the next design step. NF probing antennas will form the feedback path, requiring a structure capable of

41

coupling the signal from the antenna elements and bringing it back for DSP (digital signal processing). Thus, the transitions of the NF probing antennas must cross the middle layers, bringing the feedback signal all the way down to the bottom layer, and finally outputting via external connectors. Based on the available vias that can be built within three lamination cycles, through-hole vias L2-L13 and L2-L7 are potential candidates for building the transitions for the NF probing antennas. In addition, there can be a through-hole via drilled from L1 to L13 during the final lamination cycle (not shown in Fig 3.3). However, this type of via and the through-hole via L2-L13 cannot be used because both the NF probing antennas and beamforming IC footprints are located at the same position [as seen from the top view of the PCB in Fig 3.6 (b)], at the center of each 2×2 sub-array. Any intersection between vias used for transition and the IC footprint must be avoided during design. Thus, using the through-hole via L2-L7 to route the feedback signal is the only possible solution, and embedding the NF probing antenna on L2 is the best choice because it connects to the through-hole via (L2-L7) directly without any additional via stubs on L2. Moreover, performing any routing on L2 would break the symmetry in the NF probing antenna structure thus impacting its performance. To alleviate this issue, the NF probing antenna is routed to L13 through an L2-L7 through-hole via, a stripline on L6, and an L2-L13 through-hole via, as presented in Fig 3.6 (a). Note, both the use of the L2-L7 via to transition from L2 to L6 and the use of the L2-L13 via to transition between L6 and L13 result in unavoidable stubs in the transitions that must be taken into account during the design process. However, it was necessary to use this structure to maximize the trade-off between the limited via types, the complexity of the PCB stack-up, the NF probing antenna symmetry, and the amount of isolation between the different signals. In addition, after the feedback signal is brought down to the bottom layer by the through-hole via L2-L13, there is one more routing needed to connect the through-hole via with the RF connector. Since there are four NF probing antennas in total, four RF connectors are needed for outputting the four feedback signals. In order to save PCB area and reduce system-level testing complexity, a single-pole four-throw (SP4T) switch (PN: ADRF5043BCCZN) was selected to collect the feedback signals from the four feedback paths. The routing of feedback signals on the bottom layer uses CPWG transmission lines, marked in Fig 3.6 (b) with dashed lines in dark blue. Note, the transmission lines for routing the feedback signals are placed far away from both the beamforming IC footprint and other RF signal traces so there is space available for adding ground vias as shielding walls. The downside of this approach, however, is the increase in transmission line length which increases the path loss when receiving the feedback signals.
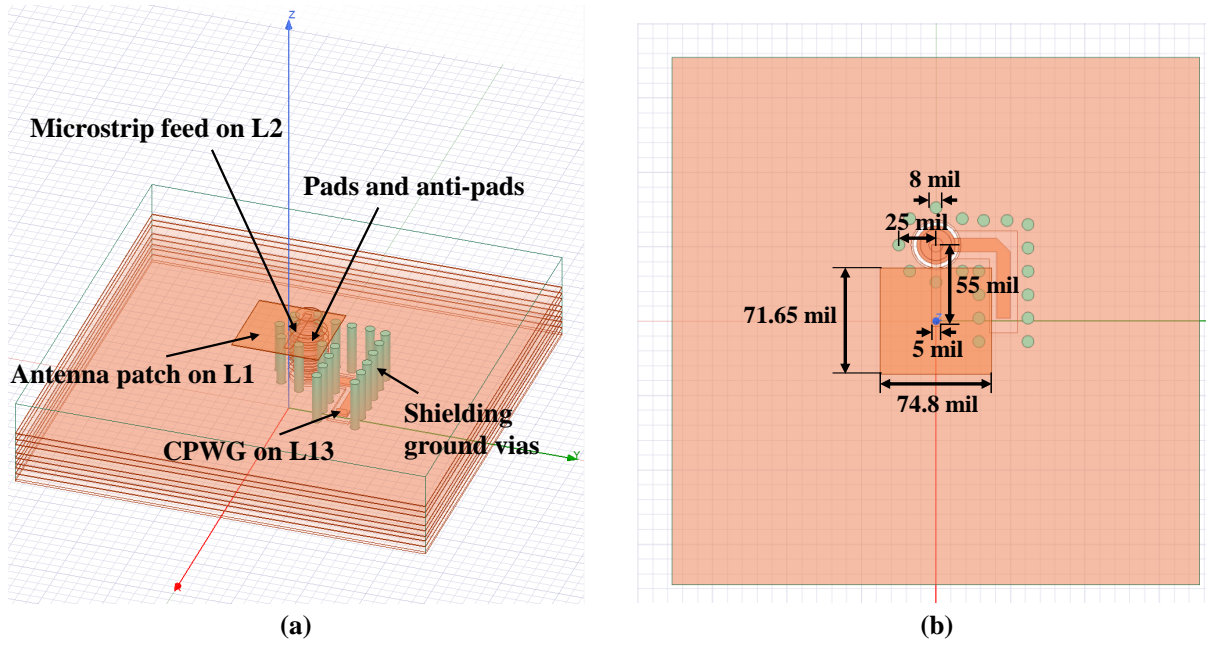
Figure 3.7: HFSS model of single antenna element. (a) Key component illustrations. (b) Detailed dimensions.
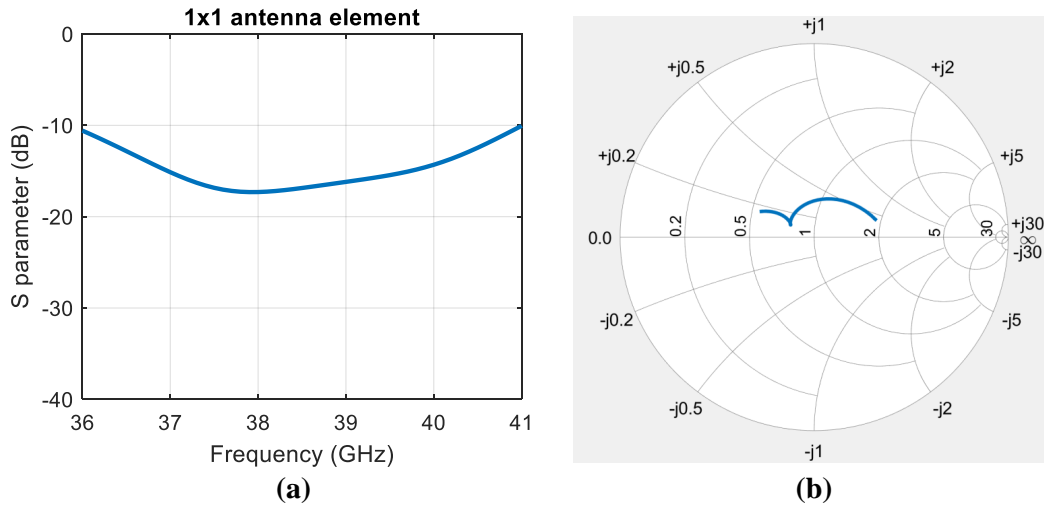
Figure 3.8: Single antenna element HFSS model performance simulation. (a) Return loss in magnitude. (b) Return loss in Smith chart.

43

(a)   (b)   (c)
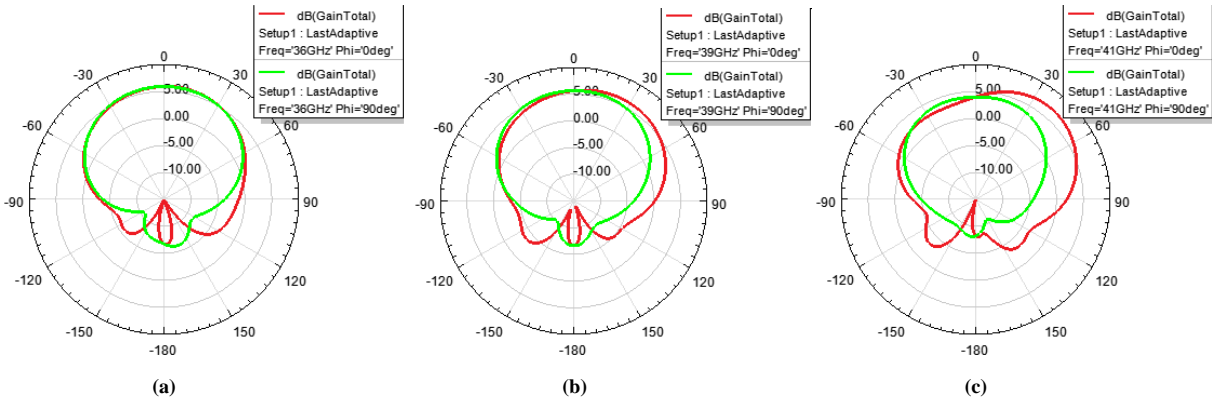
Figure 3.9: Single antenna element HFSS model simulated antenna gain on E- and H-planes at (a) 36 GHz. (b) 39 GHz. (c) 41 GHz.
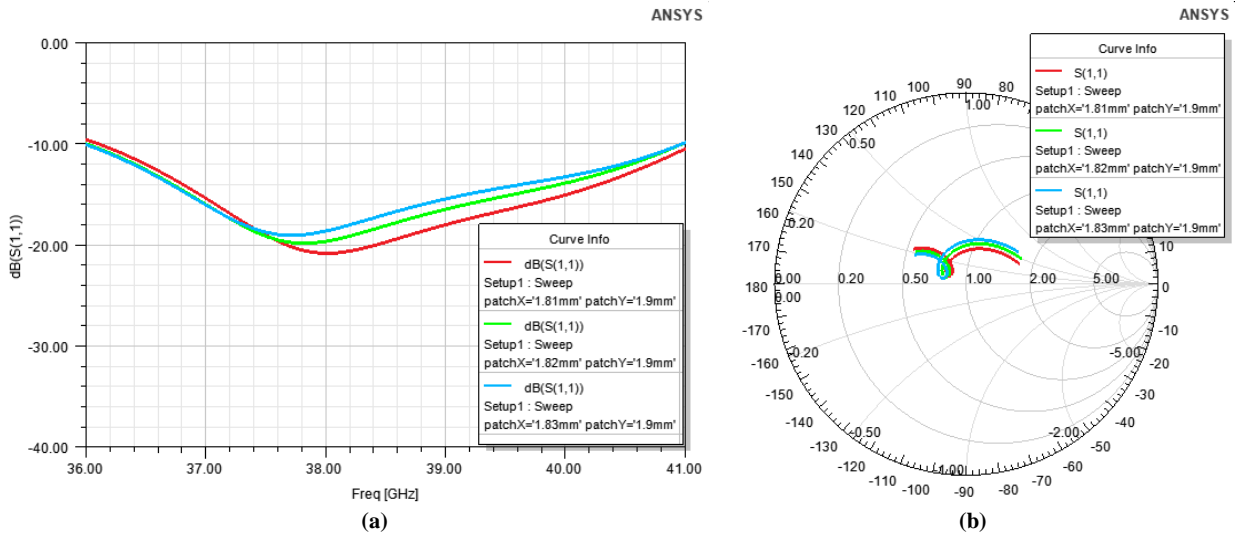
Figure 3.10: Parametric sweep of unit-cell antenna patch size showing effects on input matching. (a) Return loss in decibels. (b) Return loss in Smith chart.

44

3.3.1 Unit-cell Antenna Element Design

The design of the single antenna element is demonstrated in Fig 3.7 (a). The antenna patch is located on L1 and its microstrip feed is on L2, with the through-hole via from L2 to L13. On L13, a short path of CPWG is co-simulated with the antenna element connecting to the beamforming IC bump, and the antenna feed port is set at the terminal of the CPWG transmission line. The detailed dimensions of the antenna structure are illustrated in Fig 3.7 (b). All structures in this design were simulated in ANSYS HFSS and the EM simulation results of the single antenna element are shown in Fig 3.8. The S11 of the single antenna element is below -10 dB across the frequency band of 36-41 GHz [Fig 3.8 (a)], and the Smith chart of S11 is shown in Fig 3.8 (b). The antenna gain of the unit cell simulated at 36, 39, and 41 GHz are presented in Fig 3.9, respectively, where the red curve indicates the antenna gain on the E-plane and the green curve shows the antenna gain on the H-plane. The proposed antenna element is able to achieve more than 5 dB of gain at the boresight when the antenna element is operated at 36 and 39 GHz, where the substrate loss and transition loss from feed pin to the antenna are included; antenna mismatch loss was not included in this simulation. Considering the antenna element is well matched, the mismatch loss is minimum. In addition, the simulated radiation efficiency of the single antenna element at 39 GHz is 95.09%. Note, the design of the single antenna is not tuned for optimal impedance matching because the unit cell design is the first step of the antenna array design and, as such, no coupling exists in this 1×1 antenna array. When multiple unit cell elements are arranged to form an array grid with $\lambda/2$ spacing between, each antenna element would experience several couplings from the surrounding antenna elements with different magnitudes and the impedance matching of the antenna array would be different from the single antenna element. Therefore, the design of a single antenna element can serve only as a reference for designing the large-scale antenna array; the antenna structure must be re-tuned to optimize array RF performance. Moreover, there are many parameters of this antenna structure that would have a significant effect on the antenna input matching, and one of the main parameters is the antenna patch size. Fig 3.10 (a) and (b) show the variations of antenna input matching with changing antenna patch sizes; the resonance frequency shifts to a higher frequency while the antenna patch size becomes smaller.

3.3.2 NF Probing Antenna Design

Fig 3.11 (a) shows the key components of the proposed NF probing antenna. These include a cross-shaped patch, parasitic elements, and via/stripline transitions. The corresponding
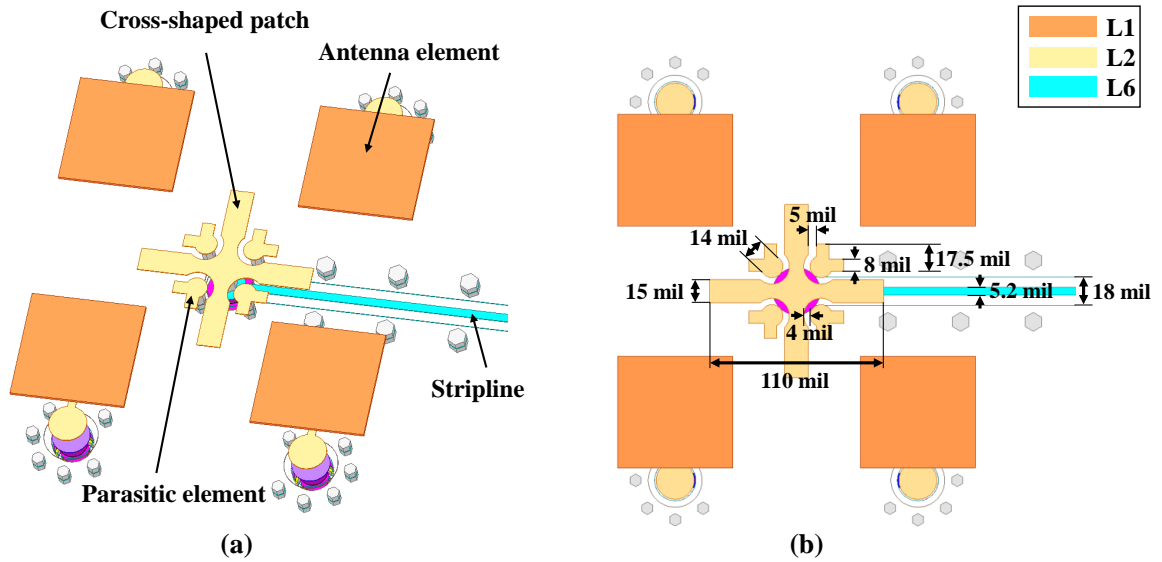
Figure 3.11: 3D model of proposed NF probing antenna design. (a) Key component illustrations. (b) Detailed dimensions.

dimensions of each key component are marked in Fig 3.11 (b). The cross-shaped patch is completely symmetrical in both the vertical and horizontal directions and is located at the center of the 2×2 sub-array on L2. Such placement ensures the spatial distance between the cross-shaped patch and its surrounding antenna elements are physically the same. In addition, the length and width of the cross shape are key parameters for tuning the resonance frequency of the NF probing antenna matching. It was determined that its optimized dimensions for the proposed design would be 110 mil × 15 mil. The small NF probing antenna size is optimized to cope with the constrained spacing between antenna elements (e.g, $\lambda/2$ antenna spacing). There are four identical parasitic elements placed symmetrically at the four corners of the cross-shaped patch on L2, and the distance between each parasitic element and the adjacent branches of the cross-shaped patch are the same such that the overall structure on L2 is completely symmetrical in both the vertical and horizontal directions. The parasitic elements are connected to the antenna ground and have minor effects on tuning resonance frequency; however, they are critical for enhancing matching stabilization and improving the isolation from other RF signals. The first stage of transition is co-designed with the NF probing antenna—the through-hole vias (L2-L7) are used to bring the signal from L2 to any middle layers up to L7, meaning the feedback signal can be accessed from any of the layers between L2 and L7. As L5 is used as an antenna

46
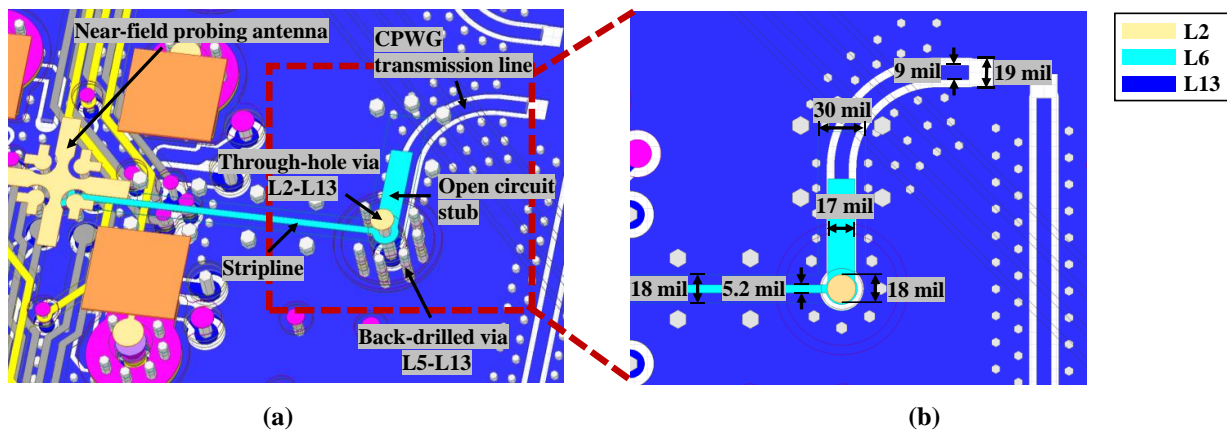
Figure 3.12: 3D model of the proposed transition design of the NF probing antenna (a) Key component illustrations. (b) Detailed dimensions.

ground and L7 is used as an RF ground for isolating the antenna and digital/power sections, they provide a perfect prerequisite for the stripline embedded in L6. Thus, using a stripline on L6 with available deep micro-vias (L5-L7) as shielding grounds fits perfectly for this design. The dimensions of the stripline are labeled in Fig 3.11 (b).

Two crucial restrictions in designing the NF probing antenna are the minimum copper trace width and the copper-to-copper clearance. These restrictions depend on PCB manufacturing capability and are provided by the manufacturer. The manufacturer producing the fabricated prototype PCB design required a minimum copper trace width of 5 mil, and a copper-to-copper clearance of at least 4 mil. Any design that exceeds these specifications cannot be fabricated; hence, it is important to keep these requirements in mind when designing to avoid wasted effort.

3.3.3 Transition Design

Fig 3.12 (a) and (b) demonstrate the detailed transition design of the NF probing antenna. Note, the middle layers on the PCB design are in transparent view, with only L13 solid, providing a clear view of the transition structure and how the signal is routed. The transition structure is labeled within the red box in Fig 3.12 (a). It begins at the stripline on L6 and then connects to a through-hole via, with surrounding back-drilled vias (L5-L13) as shielding grounds. On L13, the end of the through-hole via connects to a CPWG transmission line routed out to connect to an SP4T switch (not shown in this figure). The

detailed dimensions of all key components are labeled in Fig 3.12 (b).

The open circuit stub is the most difficult and important feature in this design. The ideal transition design should use a through-hole via (L6-L13) for routing the stripline to the bottom layer; however, due to limitations on the vias that can be utilized, only the through-hole via from L2 to L13 can be used for NF probing antenna transition. The back-drilled via (L5-L13) is not suitable for carrying an RF signal due to its fabrication process. Therefore, part of the through-hole via, from L2 to L5, turns into an additional stub in the proposed transition structure. This means the author needed to take extra care when designing the matching network and find ways to compensate for the impact of this additional via stub on the matching response. The following two design goals were set for designing the proposed transition structure:

- The structure should have a good matching response and constant group delay over a wide bandwidth at the target frequency band.

- The structure should have a compact footprint and be as simple as possible.

There are various ways in which the RF matching of the transition could be tuned. The most direct way would be to tune some parameters based on the existing structure such as via size, via pad/anti-pad size, and distance between the though-hole via and the shielding ground vias. Tuning these parameters causes significant changes in the S-parameters and matching performance. Regrettably, after many trials of tuning these parameters, the author did not find an optimal solution. Therefore, an additional matching network was included in the design to improve the matching response and recoup the effect of the extra via stub. Adding reactance such as inductors, capacitors, and short/open circuit stubs is a typical way to realize RF matching. Since inductors and capacitors are surface-mounted components, they can be placed on the bottom layer (L13) only. Another method is to use short/open circuit stubs for RF matching. The short/open circuit stubs are usually easy to implement and they can be embedded into any middle layers, bringing greater flexibility to the design. However, the fabrication accuracy of implementing these two methods differs significantly. Using discrete components requires soldering and assembly which causes more uncertainty and tolerance in the manufacturing stage compared to the embedded short/open circuit stubs. Therefore, an embedded short/open circuit stub was added for matching response enhancement in the proposed design.

The HFSS model of the proposed transition is presented in Fig 3.13 (a), where Port 1 is a waveport of the stripline on L6 that is located on the boundary of the radiation box. Port 2 is a lumped port connected to the CPWG transmission line on L13. Fig 3.13 (b)
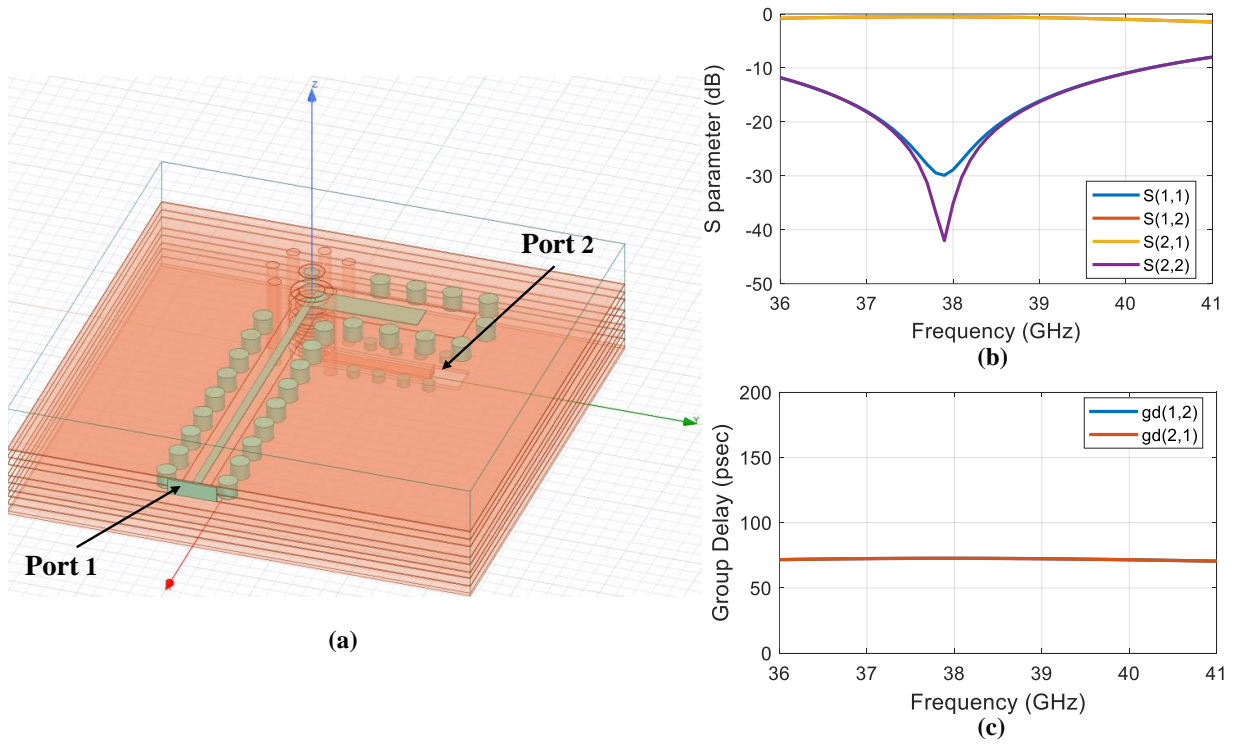
48

Figure 3.13: 3D model of proposed transition design of NF probing antenna. (a) Key component illustrations. (b) Simulated S-parameters of proposed transition. (c) Simulated group delay of proposed transition.

is the EM simulation results of S-parameters of this 2-port transition structure. It is clear that the return losses of Port 1 (S11) and Port 2 (S22) are below -10 dB and the insertion loss (S12, S21) is less than 1 dB, over the frequency band from 36-41 GHz. Fig 3.13 (c) shows the simulated group delay of the proposed transition, which is quite flat over a wide bandwidth. Note, adding an additional open circuit stub in the matching network significantly reduces the bandwidth. Therefore, a better revised PCB stack-up may need to propose in the future for minimizing the non-ideal via stubs that would occur in the designs.

3.3.4   4x4 Array Design

The 4×4 phased antenna array with four NF probing antennas was simulated and laid out on a 65 mm × 50 mm PCB. The layout design of the PCB is shown in Fig 3.14 (a) and (b). Fig 3.14 (a) is the top view of the design PCB (only L1 is shown). There are 16 copper patches, in yellow, and the NF probing antennas are embedded on L2 (which cannot be seen in the photograph). The rest of the space on L1, colored in black, represents the dielectric material. Note, there is no solder mask plated on top of L1. This is because in the HFSS simulation model, the dielectric layer on L1 is exposed to the air directly. Therefore, the solder mask should not be plated on the top layer of the fabricated PCB. Fig 3.14 (b) demonstrates the bottom 3D view of the proposed PCB (only L13 is shown). The bottom layer accommodates multiple functional components including four beamforming ICs, one SP4T switch, two vertical launch connectors, one 50-position digital connector, and one external heat sink [67]. As discussed above, the four beamforming ICs are used to generate the RF beamforming signals and the SP4T switch is used to output the feedback signals from the NF probing antennas to the DSP. The two vertical launch connectors are used to input and output RF signals which have an operating frequency range from 0 GHz up to 50 GHz. The right-hand RF connector outputs the signal from the SP4T switch, while the left-hand RF connector inputs the transmitted RF signals of the array. In addition, the 2×25-position connector is used for digital and power control, as both the beamforming IC and SP4T switch require two power voltage supplies and more than 10 digital control signals (e.g., switch-enable, chip-select, clock, SPI in/output). Finally, the attachable heat sink plays an important role in the thermal management of the phased array system. As the beamforming ICs contain multiple stages of PAs, they can generate huge amounts of heat during operation. There are two main reasons why reducing heat from the system is mandatory. First, a consistently high temperature would increase the IC aging speed and some functional blocks could become damaged under such extreme conditions. Second, heat distributed non-uniformly over the entire PCB would affect IC performance,
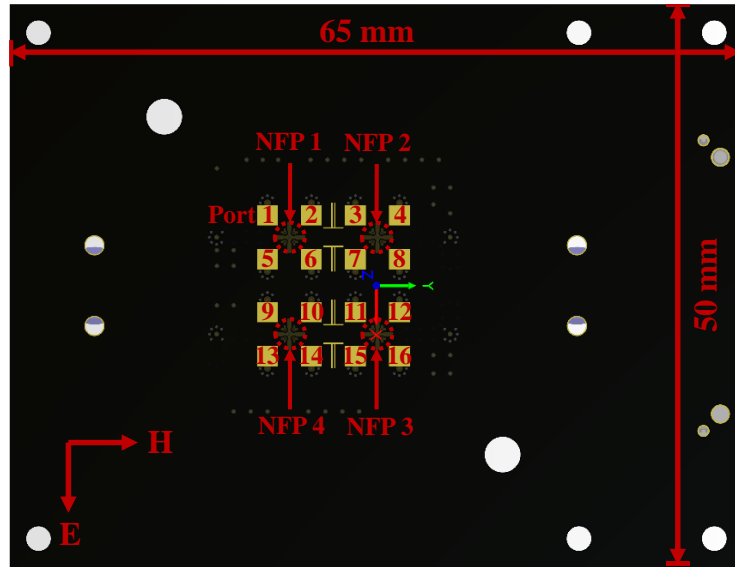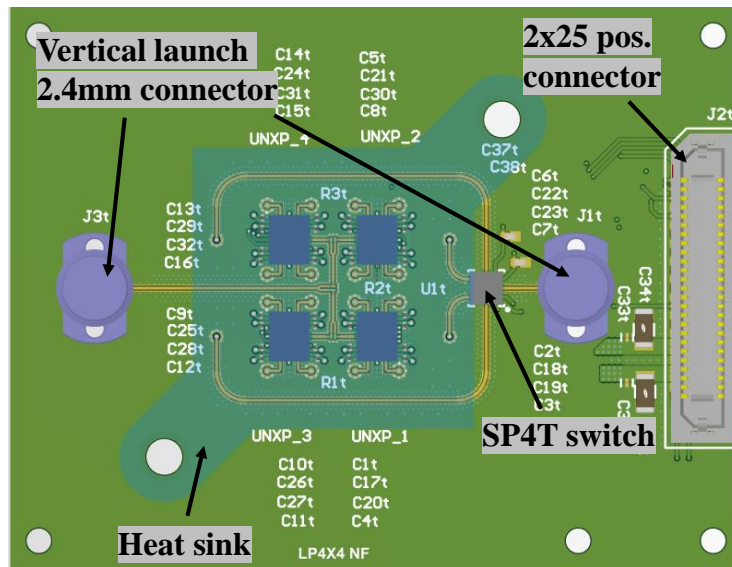
Figure 3.14: PCB layout design of proposed 4×4 phased antenna array with embedded NF probing antenna. (a) Top 3D view. (b) Bottom 3D view.
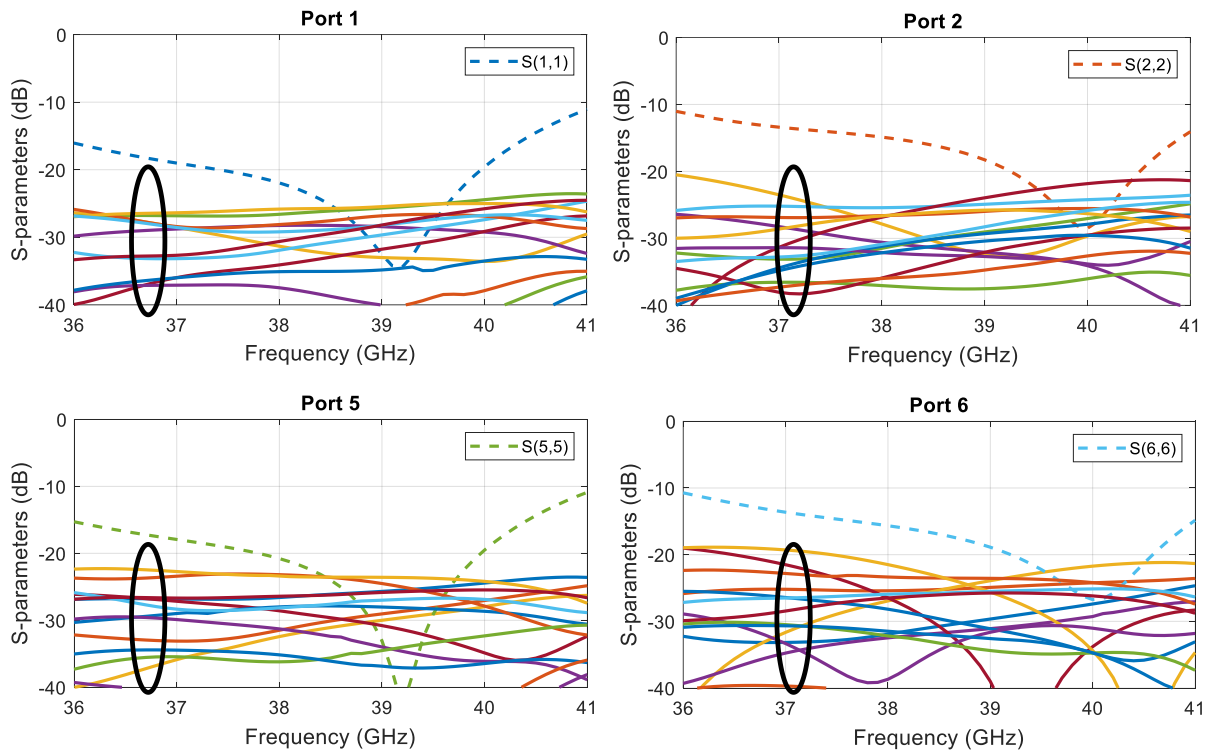
Figure 3.15: S-parameters of Ports 1, 2, 5, and 6: dashed lines represent the return loss at each specific antenna port; solid lines circled in black represent couplings between the specific antenna port and the remaining antenna elements of the 4x4 phased antenna array.

with areas closer to the IC footprint experiencing higher temperatures compared to areas further away from the ICs. Thus, in order to reduce temperature variation between different areas of the array, the most effective way is to minimize heat generated by the ICs. The external heat sink is assembled on the back side of the PCB, attached by thermal adhesive tape, right above the four beamforming ICs, which dissipates the heat generated from the beamforming ICs [67], [68].

All simulation results shown in this sub-section were produced from the post-layout EM simulation, which was done after finishing the full design of the phased antenna array on the PCB board. The PCB board was then treated as a 3D model and re-imported into HFSS. The EM simulation was then run again. The benefit of doing this second EM simulation is to ensure good RF performance as all digital routing and power planes are included as a part of the design model. If any signal routing or mechanical design issues affect the overall antenna array performance, it can be easily found out from this second EM simulation.

The port designations of the 4×4 phased antenna array can be seen in Fig 3.14 (a), with 16 ports assigned to the radiating antenna elements and 4 ports set for the NF probing antennas. The port designations in all EM simulation results shown hereafter follow the same naming convention as labeled in Fig 3.14 (a). Fig 3.15 shows the simulated S-parameters at Ports 1, 2, 5, and 6, respectively. The reason why the results for only these four ports are shown is that the phased antenna array is symmetrical; these four ports are located at a corner, top edge, left edge, and middle of the array, respectively, and therefore represent all the locations in this array. Consequently, showing the EM simulation results of the 2×2 sub-array is sufficient. The return loss of each port is presented in Fig 3.15 and is below -10 dB across the entire frequency band from 36 GHz to 41 GHz in all cases. The coupling magnitudes between the particular port and the rest of the ports are below -20 dB for Ports 1, 2 and 5 over the entire frequency band. Port 6 has a slightly higher coupling due to its relative location. The radiation antenna element of Port 6 is located in the middle of the phased antenna array, so the antenna of Port 6 would receive more couplings from its adjacent antenna elements (Ports 1, 2, 3, 5, 7, 9, 10, and 11), when compared to the antenna element of Port 1. Port 1 would also suffer fewer effects from the surrounding antenna elements (Ports 2, 5, and 6). The dashed lines in Fig 3.15 represent the magnitude couplings between each port and its closest NF probing antenna, labeled in Fig 3.14 (a) as NFP 1. As demonstrated in Fig 3.15, the magnitude couplings between each port and its closest NF probing antenna are relatively flat over the entire frequency band, with a variation of the coupling magnitude of less than 1 dB in all cases.

Fig 3.16 (a) and (b) show the active S-parameters of Ports 1, 2, 5, and 6 while steering angle varies from 0 to 60 degrees on the H- and E-planes, respectively. Active S-parameters
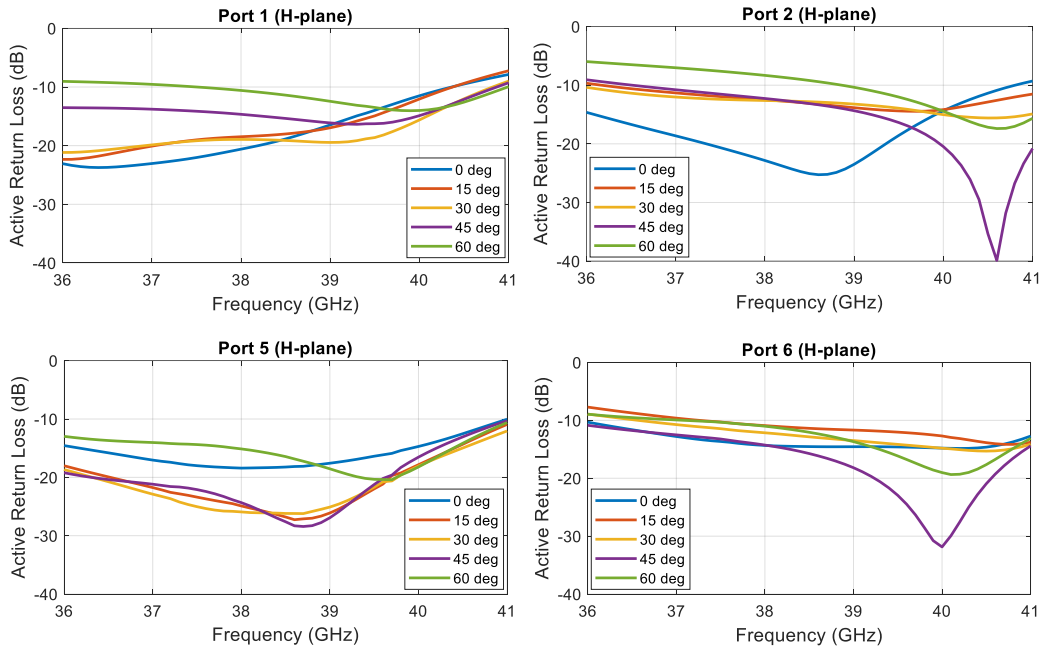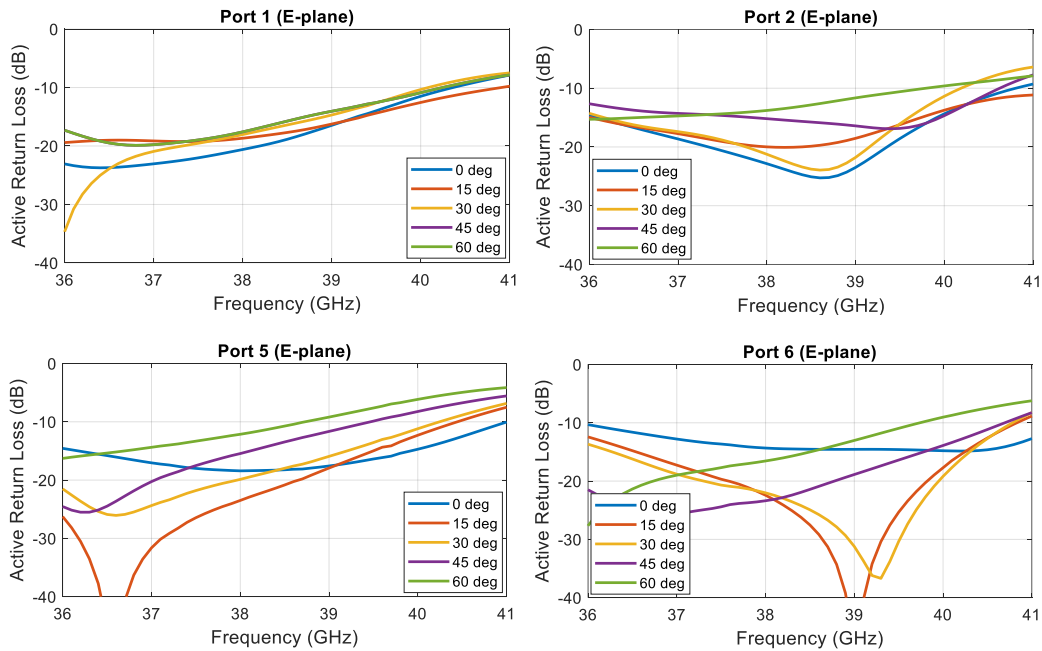
Figure 3.16: Active return losses at Ports 1, 2, 5, and 6, with different beam-steering angles on H- and E-planes, respectively.
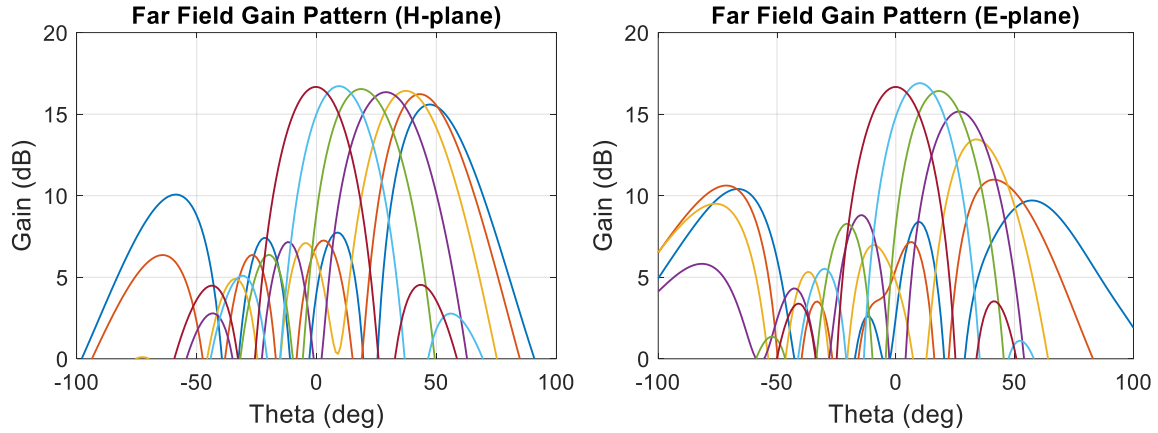
Figure 3.17: Simulated gain patterns on H- and E-planes for proposed 4×4 phased antenna array with four embedded NF probing antennas.

are based on the simulated passive S-parameters and were post-processed using Matlab. The active S-parameters were post-processed while considering the load modulations under different steering angles, so the active impedance matching and frequency responses are very distinctive from the passive ones, as shown in Fig 3.16. Moreover, the active S-parameters on the two planes perform differently. The reason for this is mainly due to the differential antenna element spacing on the H- and E-planes. Ideally, the spacing between antenna elements should be constant in both the H- and E-planes of the phased antenna array. However, the Wilkinson network of the phased antenna array is designed on L13, and its footprint is too large to fit in the ideal $\lambda/2$ grids (3.9 mm in this design). Thus, in order to accommodate the Wilkinson network on L13, the antenna spacing between the top half antenna array (Ports 1-8) and the bottom half antenna array (Ports 9-16) is larger, being 4.7 mm. Because of the non-uniform spacing on the E-plane, the beam steering performance degrades and results in worse active return losses compared to those found on the H-plane. In the frequency band from 37 GHz to 40 GHz, the active return losses are maintained under -10 dB under steering angles of up to 45 degrees in all ports on the H-plane. On the E-plane, Ports 1 and 2 are able to steer at 45 degrees with the active return loss lower than -10 dB, but at Ports 5 and 6, the active impedance is slightly more mismatched than on the H-plane.

Based on the HFSS simulations, the gain and radiation pattern can be generated, post-processed, and plotted in Matlab. Fig 3.17 illustrates the far-field gain patterns on both H- and E-planes when the array is simulated at 38.5 GHz. Note, the gain patterns show only the right-half side; the left-half pattern is hidden to allow for a clear view of its side-lobe

level. In fact, the left and right halves are symmetrical with respect to the boresight beam (theta is 0 degrees). In Fig 3.17 (a), each colored line represents a steering angle of 0, 10, 20, 30, 40, 50, and 60 degrees. The red curve sits at the center of the figure with theta equal to 0 degrees, showing the gain at the boresight can achieve 16.6 dB, and is able to steer -/+ 50 degrees with an offset of more than 7 dB at its side-lobe level. Note, the reason that the 60-degree curve in dark blue is not able to align with 60 degrees on the x-axis is due to the small size of the array. Moreover, the drop of the gain decreases slowly as the steering angle increases, and the beam steering to 50 degrees achieves a gain of 15.5 dB. The gain pattern on E-plane is significantly worse than that on H-plane, mainly due to the non-uniform antenna spacing. As demonstrated in Fig 3.17 (b), the gain drops rapidly and the side-lobe level increases as well. When the beam is steered to about 40 degrees, the main beam and its side-lobe reach almost the same power gain level. This means the radiation efficiency drops significantly and there is an unwanted beam pointed in an undesired direction. Not only is the radiation performance of the array itself degraded under such circumstances, but it also raises the risk of interfering with other array systems.

To assess the impact of embedding the probing antennas, the same phased array design without the four NF probing antennas was simulated and post-processed using Matlab. No remarkable differences were found between the two gain patterns, proving that embedding the proposed NF probing antennas into the main phased antenna array should not affect the array's gain patterns.

The simulated performance of the proposed NF probing antenna is shown in Fig 3.18 and Fig 3.19. Fig 3.18 shows the magnitude couplings between each NF probing antenna and the 16 radiating antenna elements of the main phased antenna array, where the dashed lines are the couplings among each NF probing antenna to its nearest four radiating antenna elements and the solid lines are the couplings to the rest of the radiating antenna elements. The dashed curves in the figure also highlight less than 3 dB variation while maintaining higher than -18 dB coupling magnitudes across the entire frequency band. In addition, the coupling magnitudes between each NF probing antenna and the further radiating antenna elements are all below -22 dB, making the desired coupling magnitudes more distinctive from the totality of couplings received from each NF probing antenna. Fig 3.19 demonstrates the group delay between each NF probing antenna and its closest four radiating antenna elements. Group delay is the derivative of the phase variation versus the frequency, so a constant group delay indicates linear phase changes with varying frequency—desirable in a design aiming to apply array calibration and DPD training. The variation among simulated group delays for each NF probing antenna is less than 35 ps across 36 GHz to 41 GHz, for all four NF probing antenna cases.

In order to assess the ability of the proposed NF probing antenna to accurately repre-
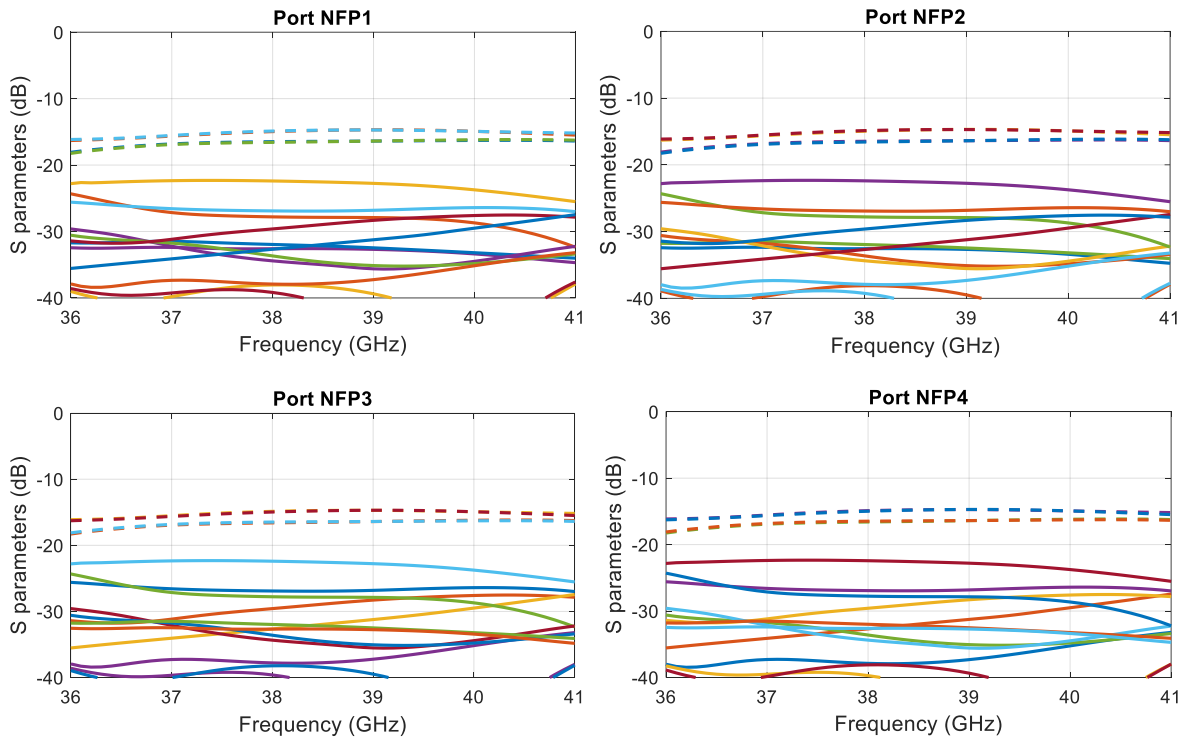
Figure 3.18: S-parameters of four NF probing antenna ports: dashed lines are couplings between each NF probing antenna and its closest four radiating antenna elements; solid lines are couplings between each NF probing antenna and its further 12 radiating antenna elements.
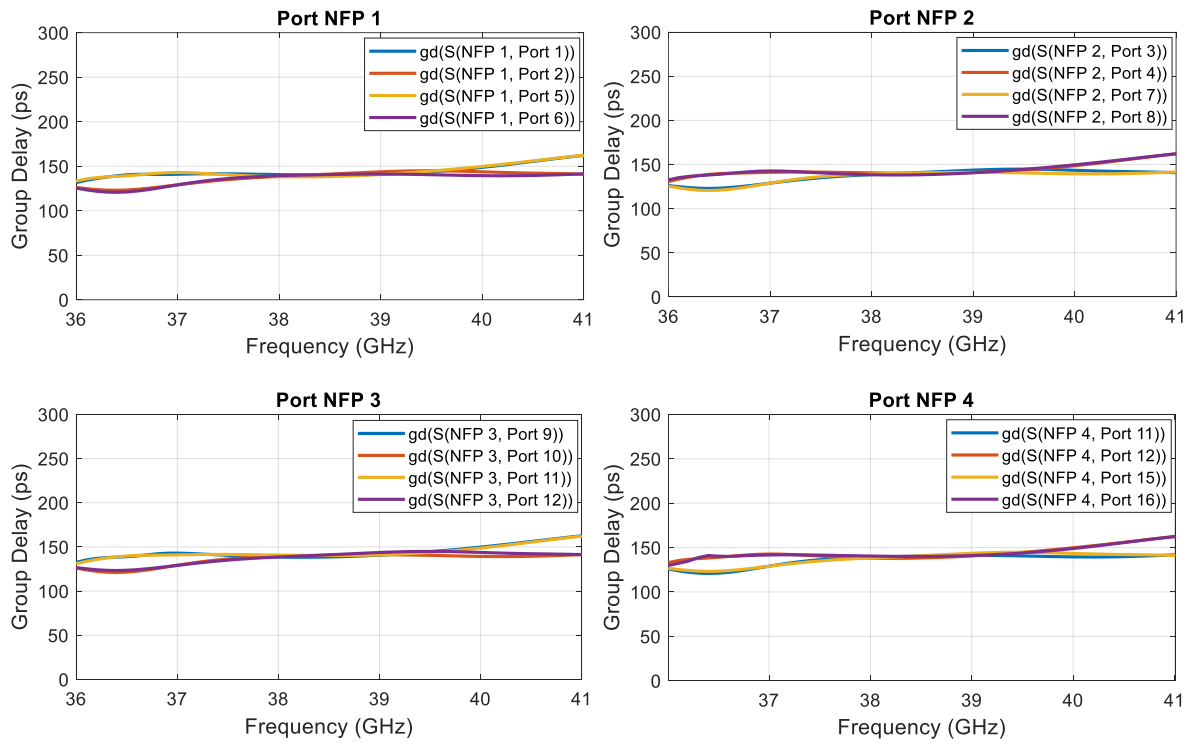
Figure 3.19: Group delays between each NF probing antenna and its closest four radiating antenna elements.
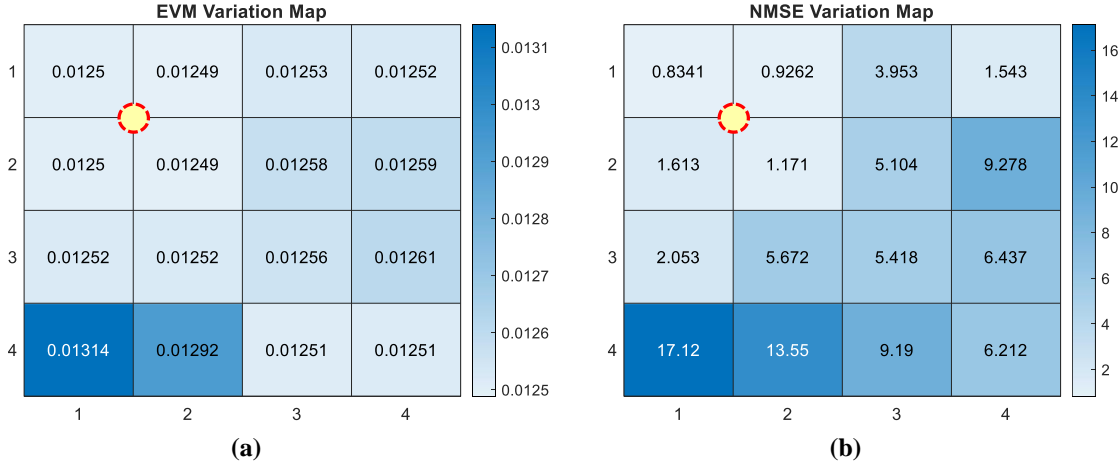
Figure 3.20: Proposed NF probing antenna simulated performance. (a) EVM results. (b) NMSE results.

sent the output of the PA, an extreme case simulation for the modulated signal was carried out. A 256 quadrature amplitude modulation (QAM), orthogonal frequency-division multiplexing (OFDM) signal with 800 MHz modulation bandwidth centered at 38.5 GHz was applied in the simulation with the waveform having a sub-carrying spacing of 120 kHz and peak-to-average power ratio (PAPR) of 11 dB. Fig 3.20 (a) and (b) show the post-processed simulation results of the proposed NF probing antenna based on the EM simulated results using Matlab. Fig 3.20 (a) is the 4×4 variation map of the simulated EVM of all 16 radiating antenna elements when one of the four NF probing antennas (marked as a yellow circle) transmits the modulated signal. A similar simulation was done to examine the normalized mean square error (NMSE) and the result is illustrated in Fig 3.20 (b). It is evident that the EVM values for the four antenna elements located closest to the specified NF probing antenna (the upper-left quarter in the 4×4 grid) have the lowest values among all of the 16 grids. A similar pattern was found for the NMSE case. Such low EVM and NMSE values indicate flat couplings and constant group delay between the NF probing antenna and the adjacent radiating antenna elements. Therefore, it can be concluded that an adequate and superior design for an NF probing antenna has been achieved.

59

Chapter 4

Experimental Validation

The PCB prototypes of a single antenna element and 4×4 active phased antenna arrays with and without embedded NF probing antennas were fabricated and assembled for experimental validation.

4.1 Passive Antenna Element Measurement

A PCB-based single antenna element was fabricated for testing purposes. The differences between the EM simulation and physical measurement results for the fabricated prototype are presented in Fig 4.1. The orange curve denotes the EM results for the post-layout simulation of the proposed antenna element with an RF connector co-simulated; the blue curve indicates the measurement results found for the fabricated single antenna PCB with the same RF connector simulated. Note, the simulation results shown in Fig 4.1 are different from those discussed in Section 3.3.1; the previous EM simulation was not a post-layout simulation and the RF connector was not included in that design. When the EM simulation results of the HFSS model [Fig 3.8] and the post-layout simulation with RF connector in Fig 4.1 are compared, it is clear the impedance matching of the signal antenna element differs significantly. Therefore, post-layout simulation is a necessary design process step to ensure suitable RF performance for the final prototype.

Moreover, there is a huge distinction between the post-simulation result and the measurement result, and the reasons for such variation come from multiple aspects. First of all, the PCB fabrication process produces high insertion loss which can not be presented in an ideal HFSS model. A PCB-based CPWG transmission line is also fabricated as a measurement reference and the measured insertion loss of this transmission line is -3.8 dB/inch at
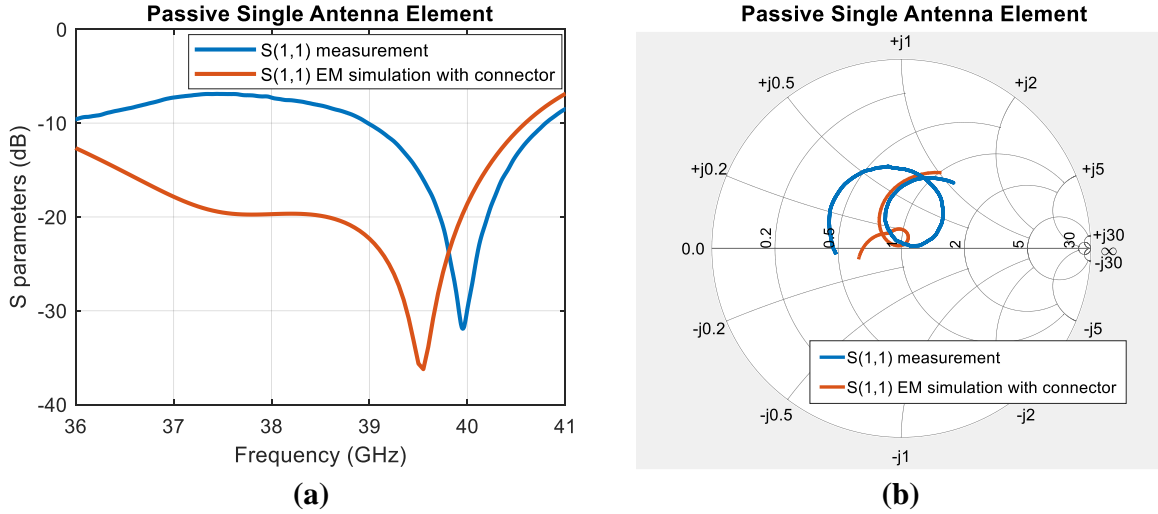
Figure 4.1: EM simulation versus measurement results. (a) Return losses in magnitude. (b) Return losses in Smith chart.

39 GHz, which is about 3 dB more loss than the simulated loss of an ideal CPWG model. Secondly, the surface roughness and the surface finish of PCBs are other factors that would affect the measurement results. The antenna patches are made of copper, and the surface of the copper patches has a certain roughness, which is not as perfectly smooth as the structure that is simulated in HFSS. Furthermore, manufacturer's typically complete the PCB by plating surface finish on both the top and bottom of the PCB to protect against corrosion and other malformations. There are many kinds of surface finish, and the most commonly used for RF circuitry is electroless-nickel-immersion-gold (ENIG), which is a composition of nickel and gold. In general, the process of ENIG starts with a thin layer of nickel being plated on top of the copper, and then another thinner layer of gold is plated on top of the nickel. To assess the impact of both surface roughness and ENIG surface finish on results, another post-layout simulation was done which showed around 3.1 dB/inch of loss using a non-ideal CPWG model. The actual errors and variations due to the manufacturing process are difficult to predict and compensate for during the design/simulation stage. It is therefore recommended that designers find a practical method for predicting or minimizing fabrication errors for better measurement results.

The third explanation for the variation between simulation and measurement results is the tolerance of the heights of the copper/substrate. The key factor contributing to the tolerance is the copper rate of each layer on the PCBs. The copper rates provided by

61
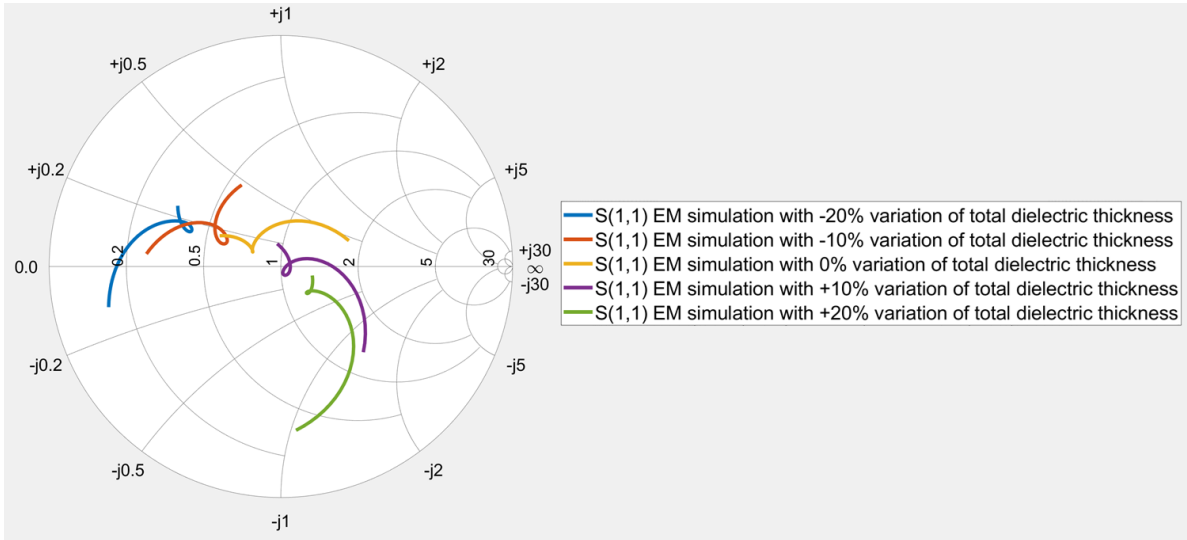
Figure 4.2: EM simulations of single antenna element model on HFSS with different variations of total dielectric thickness.

the manufacturer on a PCB stack-up are estimates; the manufacturer does not know the exact design or an accurate copper rate on each layer. Therefore, the preliminary design and simulation are based on a stack-up with estimated PCB parameters. An incremental increase or reduction in the copper rate of a copper layer would cause significant height changes on the dielectric layer above it. Typically, the copper traces are etched from a copper foil with a 100% copper rate. A sheet of prepreg is then laminated on top of the copper layer. Because the thickness of the prepreg sheet is a standard number, the more copper is etched out, the more prepreg material would fill in those grooves, which decreases the overall thickness of that layer. In most cases, an antenna structure requires a certain height of dielectric on the PCB to maintain good bandwidth and matching performance. It is common practice to use some layers in the PCB with very low copper rates as non-metal layers to maintain a certain height of dielectric for the antennas. In the proposed design, L3 and L4 of the PCB did not have any copper traces or planes, and the copper rate of these layers was less than 5%. However, based on the PCB stack-up provided by the manufacturer, the copper rate was given as 80%. Thus, the thickness of the dielectric layers of L3 and L4 was severely over-estimated in the simulations. To investigate the effect of substrate thickness variations on impedance matching, several simulations were performed. The results are presented in Fig 4.2. As seen from Fig 4.2, four cases were simulated, each with varying thicknesses of the total dielectric on the PCB. These were
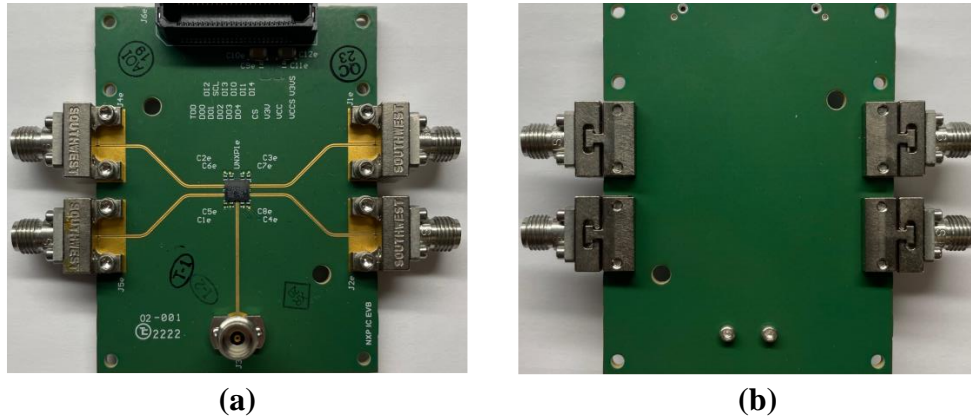
Figure 4.3: Photos of fabricated beamforming IC EVB. (a) Top view. (b) Bottom view.

compared to the reference thickness case (in yellow) (as discussed in Section 3.3.1). It is clear that varying the thickness of the total dielectric alters the matching performance of the antenna to a remarkable extent. To summarize, the tolerance and inaccurate copper rate estimation resulted in deviations in the performance found between EM simulated and measured results. One potential solution to improve this issue would be to provide the design files to the manufacturer and ask for an updated PCB stack-up based on the actual design which could then be used to re-simulate the design. Then, the matching network could be re-tuned if needed for better impedance matching. If such a process were followed, the copper rate (and therefore the dielectric thickness) would be more accurate and the EM simulation would better match measurement results. However, the drawback of this solution is the extra effort and time required from the designers.

4.2 Beamforming Array and Embedded NF Probing Antenna Assessment

4.2.1 Conducted Measurement of Beamforming IC Evaluation Board

An evaluation board (EVB) of a single beamforming IC (MMW9003KC) was fabricated on which to run conducted measurements as shown in Fig 4.3. The EVB was built on the same PCB stack-up and connected to five RF connectors—one for the RF input signal
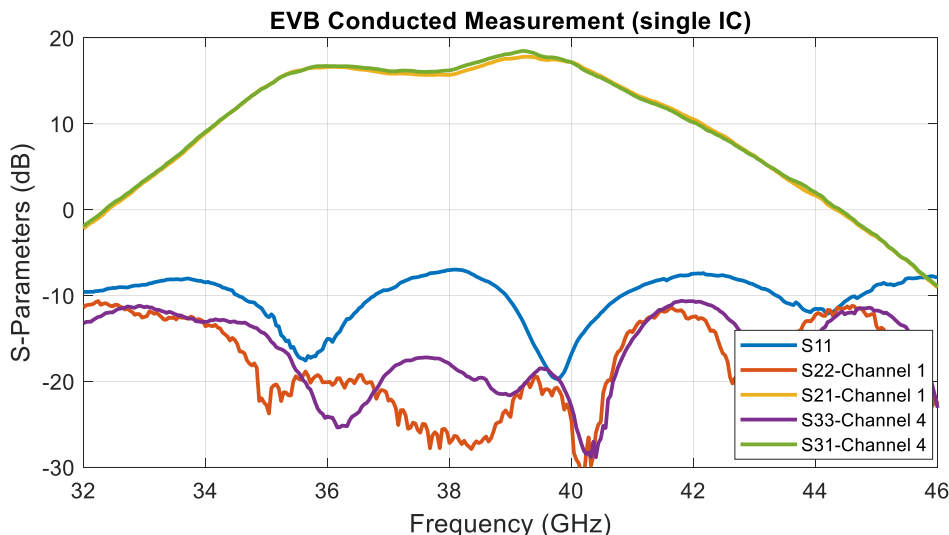
Figure 4.4: EVB conducted measurement results.

and the other four for the outputs of the four RF beamforming channels. The purpose of a conducted test is to verify the testing code for digital control and to understand the behavior of a single beamforming IC. Fig 4.4 presents the conducted measurement results of the single beamforming IC, where Port 1 is the RF input and Port 2 and Port 3 are two of the four beamforming channels. Since a five-port network cannot be measured by a four-port vector network analyzer (VNA) in a single run, the conducted measurement was split into two runs, each measuring the input and two of the four beamforming channels with the remaining ports terminated with 50-ohm coaxial connector terminators. Both sets of RF channels showed similar performance, as shown in Fig 4.4. The measured S21 and S31 showed a relatively flat frequency response over the frequency from 36 to 40 GHz, with a slight rise at 39 GHz; a similar trend was observed in the measurement results for the proposed 4×4 active phased antenna array. The measured S11 was below -7 dB across the frequency band 32-46 GHz, which matched the performance reported from the datasheet of the beamforming IC.

4.2.2   Over-the-Air Measurement Setup

Fig 4.5 (a) and (b) are photos of the proposed 4×4 beamforming array with embedded NF probing antennas fabricated PCB. Fig 4.6 (a) is the block diagram of the measure-

64
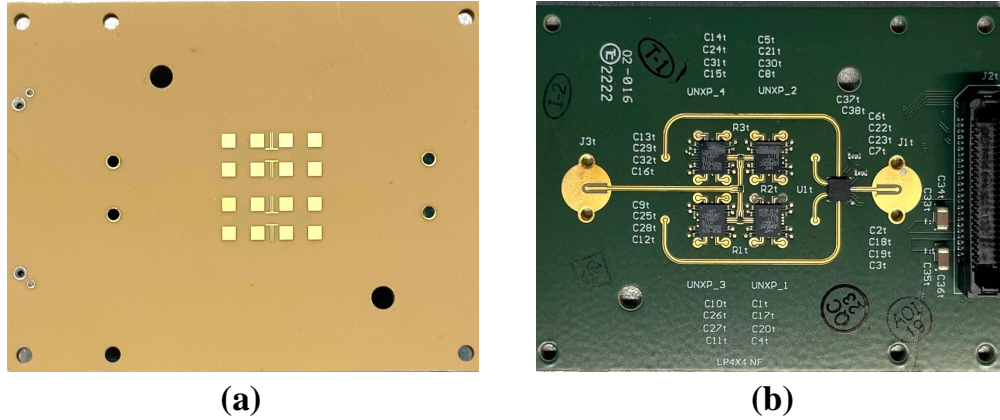
Figure 4.5: Photos of fabricated 4×4 active phased antenna array with embedded NF probing antennas. (a) Top view. (b) Bottom view.

ment setup. A Keysight N6705B DC analyzer was used for the power supply, providing voltages of 5V and 3.6V for the beamforming ICs and another 5V for an external fan. A Keysight N9040B VNA and a standard gain horn were used for the array calibration and measurements. The horn antenna was located in the far field 1 m away from the AUT and the output of the horn antenna was connected to one of the ports of the VNA using an RF cable. There are two RF ports on the phased antenna array PCB, as discussed in Section 3.3.4: one is the RF input of the phased antenna array and the other is the RF output of the NF probing antennas. Both RF ports were connected to the VNA using RF cables. Fig 4.2 (b) and (c) are photographs of the in-lab measurement setup. This setup was placed inside walls of RF absorber foam that acted as an anechoic chamber. The 4×4 active phased antenna array with embedded NF probing antenna was connected to an adapter board and then assembled on a mechanical holder. The adapter board was a 4-layer FR4 PCB and was used for power transition from the power supply to the phased antenna array. It also provided an interface for controlling the digital signals through National Instruments (NI) USB-8452 for I2C/SPI controls. The mechanical holder was fixed on a positioner with a programmable motor for rotating the active phased antenna array. In this way, the direction of the array boresight could be controlled digitally via the positioner.
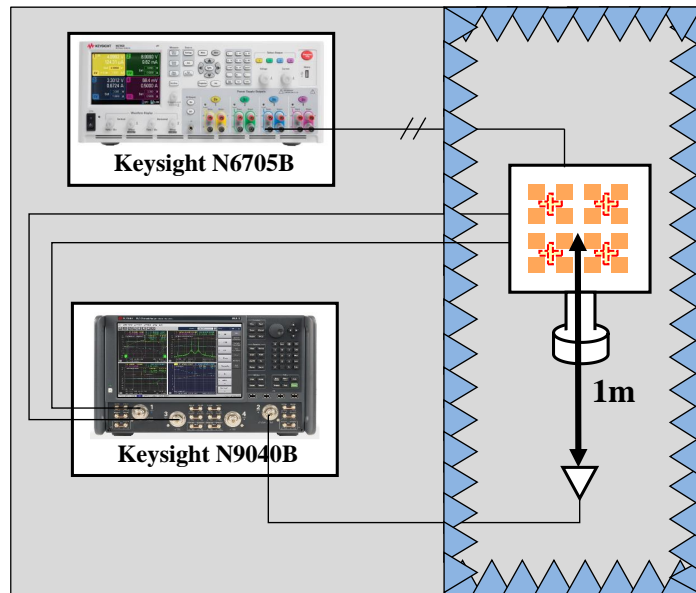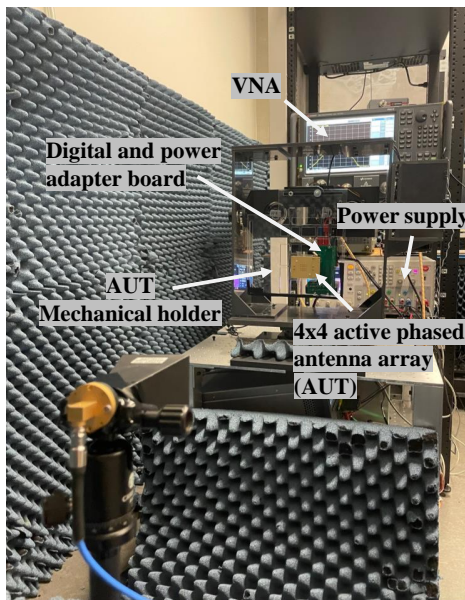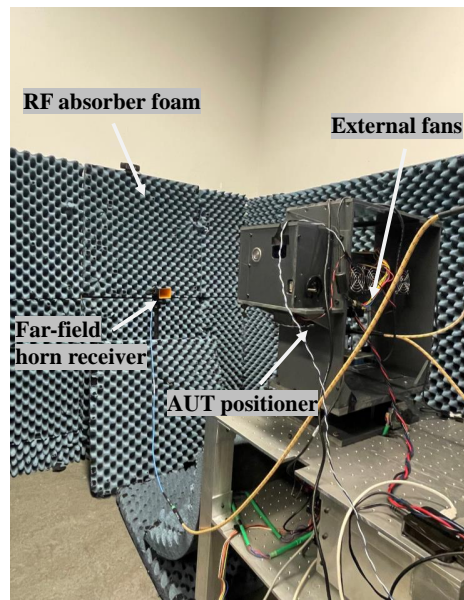
Figure 4.6: Measurement setup for NF probing antenna test and array calibration. (a) Block diagram of measurement setup. (b) View on phased antenna array side. (c) View on horn receiver side.
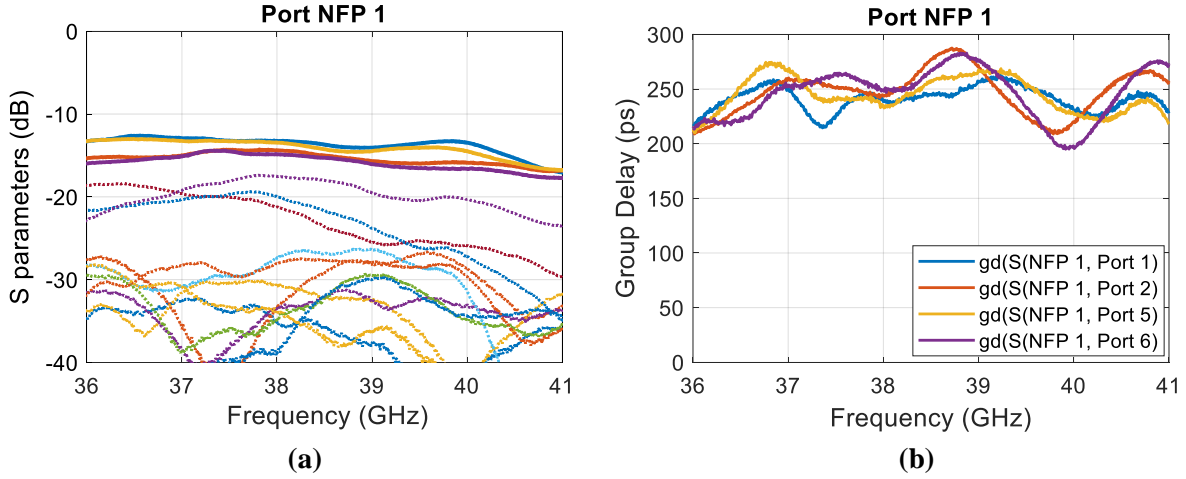
Figure 4.7: Measured performance of proposed NF probing antennas. (a) S-parameters of a single NF probing antenna (NFP 1)—the solid lines represent the couplings between the NF probing antenna and its closest four radiating antenna elements; the dashed lines are the coupling to its further radiating antenna elements. (b) Group delays between NFP 1 and its closest four radiating antenna elements.

4.2.3 NF Probing Antenna Performance

Measurements of the prototyped four NF probing antennas were taken using a far-field horn antenna and the 4×4 active phased antenna array. Two different signals were received by the VNA during testing: a feedback signal output from the SP4T switch (the coupled signal captured by the NF probing antenna while only one antenna element was radiating), and the far-field signal received by the horn antenna. Both signals included the same phase difference. By taking the ratio of the received signals and multiplying by the OTA path loss, the coupling between a single NF probing antenna and a single radiating antenna element was obtained. Moreover, by turning on the 16 radiating antenna elements one by one, all of the couplings between a single NF probing antenna and the 16 radiating antenna elements could be captured. This process was repeated four times, once for each NF probing antenna. Similar performances were found for all four NF probing antennas during measurement.

The measured coupling magnitudes between an NF probing antenna and the 16 radiating antenna elements are shown in Fig 4.7 (a). The four solid lines represent the coupling magnitudes between the NF probing antenna #1 and the radiating antennas of Ports 1, 2,

67
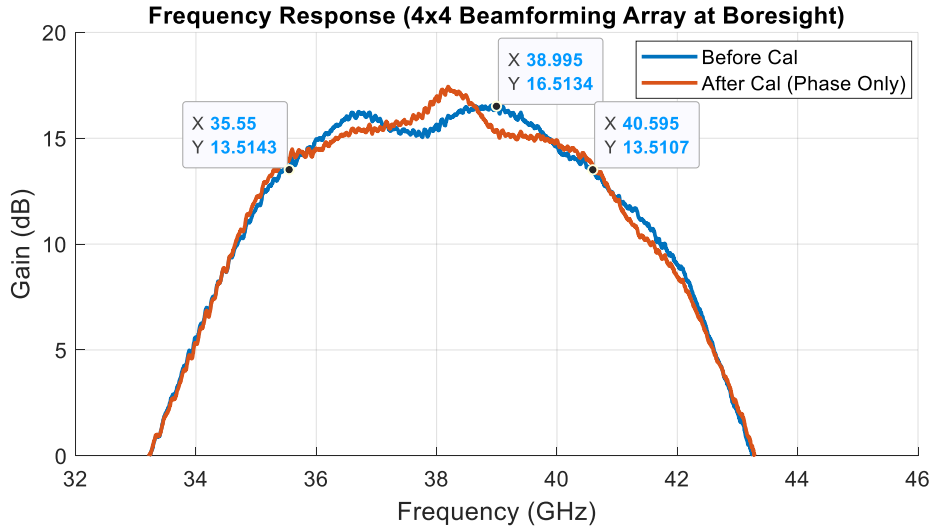
Figure 4.8: Measured frequency response of proposed 4×4 beamforming array at boresight.

5, and 6, while the dashed lines are the coupling magnitudes to the rest of the radiating antenna elements. It is clear that the proposed NF probing antenna can achieve flat coupling responses where the coupling magnitude varied by less than 4 dB across the entire designed bandwidth from $37 - 41$ GHz. In terms of the group delay, the variation between each coupling is less than 85 ps as shown in Fig 4.7 (b), demonstrating good agreement with simulation results. Note, the discrepancies between the experimental coupling of the NF probing antenna to the further 12 elements and its simulation results were mainly attributable to PCB fabrication errors. For instance, there were some unexpected solder pastes on some of the transmission lines at the bottom layer of the fabricated PCB noticed by the author which could have affected the measurement results.

4.2.4 Measured Array Gain and Radiation Pattern

Fig. 4.8 illustrates the fabricated array's frequency response over the frequency band from 32 to 44 GHz—the blue curve represents the array frequency response without any calibration; the orange curve is the frequency response with phase calibration only. The highest gain without calibration of 16.5 dB occurs at 39 GHz, matching post-layout simulation results [Fig 3.17]. This result also matches the theoretical antenna array gain found by multiplying the gain of a single antenna by $10\log_{10}($the number of antenna elements in the

68
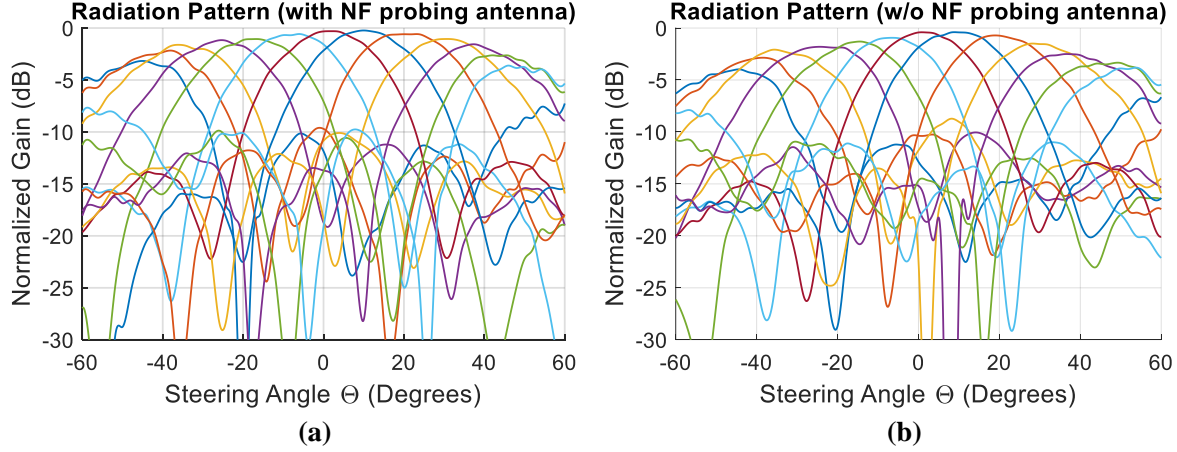
Figure 4.9: Measured normalized radiation patterns on the H-plane. (a) 4×4 active phased antenna array with four embedded NF probing antennas. (b) 4×4 active phased antenna array without NF probing antennas.

array), very well. Both cases (with and without calibration) were able to achieve a 3 dB gain bandwidth from 36 to 40 GHz, covering the entire band of n260. In addition, the small fluctuation of the frequency response followed a similar shape to the conductive test results obtained for the beamforming IC EVB, as presented in Fig 4.4.

In order to investigate the effects of the embedded NF probing antennas on the radiation performance of the phased antenna array, a 4×4 linear-polarized antenna array without NF probing antennas was fabricated to serve as a benchmark. The measured radiation pattern of the 4×4 linear-polarized array with NF probing antennas is shown in Fig. 4.9 (a). The radiation pattern found for the proposed array without NF probing antennas embedded is shown in Fig. 4.9 (b). Both arrays were steered between ±50° on the H-plane. It is clear that the array radiation pattern was not affected by including the proposed NF probing antennas in the array. In addition, the side-lobe level of the beam that steered to ±50° was similar to simulation results, and 8 dB lower than the main beam. Therefore, measurement results confirmed the negligible impact of the NF probing antennas on the antenna array's radiation pattern.
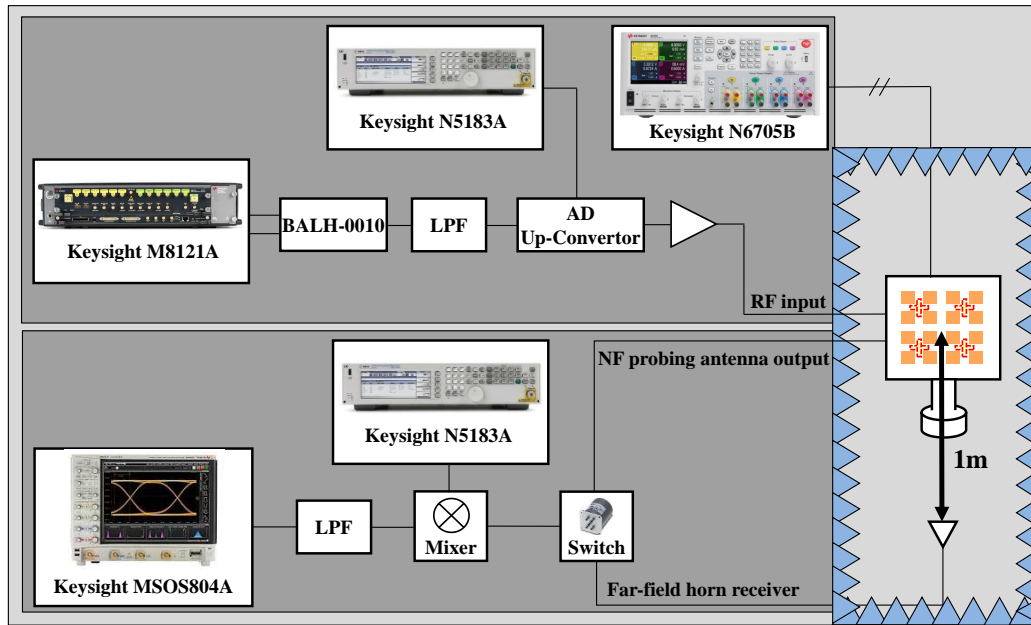
Figure 4.10: Block diagram of modulated measurement setup.

4.3 Modulated Signal Measurements

A block diagram of the modulated signal test setup is shown in Fig. 4.10. The 4×4 active phased antenna array was fed with a 256 QAM OFDM waveform generated by a Keysight M8121A arbitrary waveform generator (AWG) and up-converted to 38.5 GHz with a Keysight N5183A signal generator as the LO source. A Keysight N6705B was used for each of the power supplies. The transmitted signal from the radiating antenna elements coupled to the NF probing antennas was routed to an external single pole double throw RF switch. Another input to this RF switch is the signal received by the far-field horn antenna, and the reason for adding the horn antenna in the far-field is to examine the performance of the DPD training algorithm. One of the two signals can be selected, down-converted, and demodulated by a Keysight MSOS804A oscilloscope at a time.

EIRP (effective radiated power) is a key performance metric for beamforming phased array systems and the estimated EIRP with 256 QAM OFDM modulated signal based on the measured antenna array gain of the 4×4 active phased antenna array at 38.5 GHz is

calculated as (4.1):

$$\begin{aligned}
EIRP_{256 \text{ QAM}}(dBm) &= P_{\text{out, TX}}(dBm) + G_{\text{TX}}(dB) \\
&= (10 log_{10}(16) + P_{\text{1dB}} - PAPR_{256 \text{ QAM}}) + Antenna Array Gain \\
&= (12 + 16 - 9) + (16) \\
&= 35
\end{aligned}$$

(4.1)

where the modulated signal is a 256 QAM OFDM with a PAPR (peak-to-average power ratio) of 9 dB.

A DPD training algorithm was applied to the calibrated 4×4 beamforming array with embedded NF probing antennas to test the performance of the feedback paths. Two test signal cases were used during this measurement, both employing 256 QAM OFDM signals with 9 dB PAPR and subcarrier spacing of 120 kHz, the first with a modulation bandwidth of 200 MHz and the second with a bandwidth of 800 MHz. Fig. 4.11 shows the ACPR and EVM results for the two cases (before and after DPD training) with EIRP varying from 30 to 35 dBm. The figure also shows the corresponding spectrum for each case. It is obvious from this figure that applying the DPD training algorithm with the NF probing antenna as the feedback path, improves the ACPR and EVM significantly compared to without DPD training.

Fig. 4.11 (a) shows that by applying the DPD training using the proposed NF probing antennas, at an EIRP of 34 dBm, the EVM was reduced from 8.7% to 2.88% and the ACPR was improved from 28 to 25.6 dBc for the 200 MHz modulated signal. Similar trends were found for the 800 MHz modulated signal, as shown in Fig. 4.11 (b), where the EVM was reduced from 9.1% to 2.86% and the ACPR was improved from 27.9 to 35.4 dBc, at an EIRP of 34 dBm. The right-hand side of Fig. 4.11 (a-b) shows the power spectral density of the 200 and 800 MHz modulated signals with and without DPD training. By applying the DPD training under a 200 MHz bandwidth modulated signal at 38.5 GHz, the ACPR of the lower channel was improved from 31.1 to 40 dBc and from 31.6 to 39.2 dBc for the upper channel. For the 800 MHz modulated signal, the ACPR was improved from 30.5 to 38.4 dBc for the lower channel and from 30.1 to 39.5 dBc for the upper channel at the EIRP of 33.2 dBm.

The same DPD training algorithm was also implemented at the far field with a standard horn antenna as the feedback path. Similar curves of ACPR and EVM versus EIRP were achieved, verifying that the proposed method of using NF probing antennas for array DPD training is an effective alternative to DPD training using a far-field receiver.
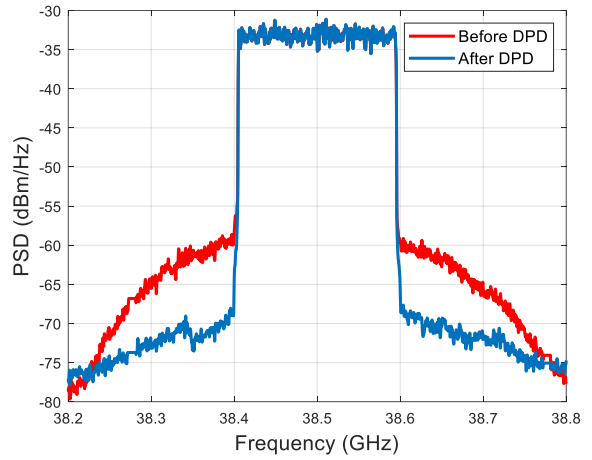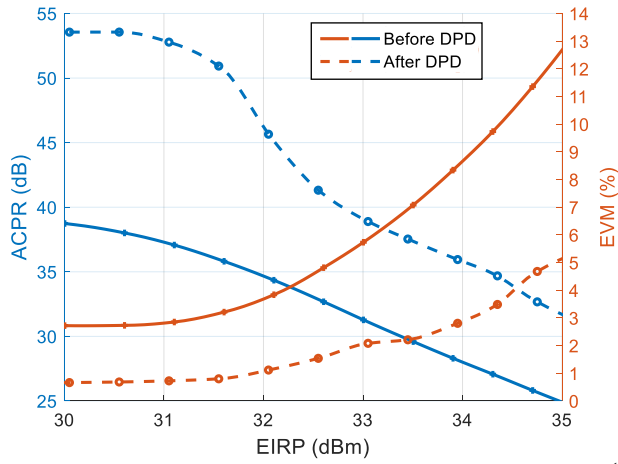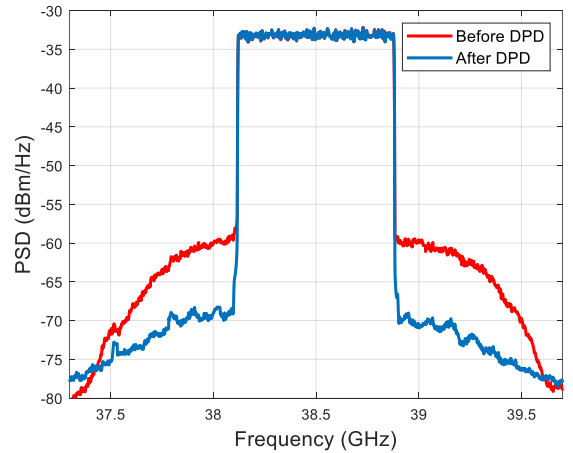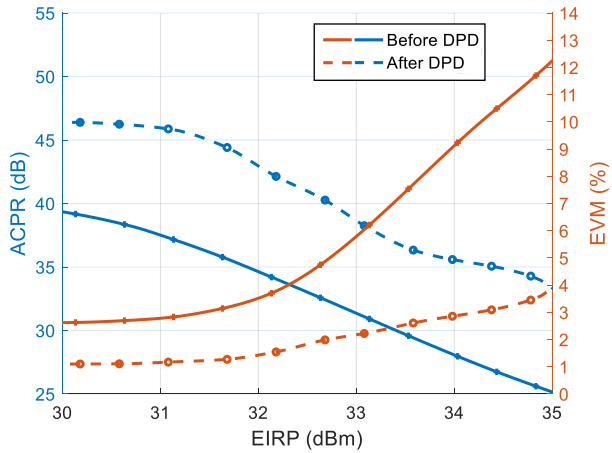
Figure 4.11: ACPR and EVM versus EIRP (left) and wave spectrum (right) under modulated signals of (a) 200 MHz modulation bandwidth, and (b) 800 MHz modulation bandwidth.

Chapter 5

Conclusions and Future Work

5.1   Conclusions

5G communication is the latest wireless communication technology; it promises to achieve superior peak data rates, latency, and connection density compared to previous generations of mobile networks. By achieving such boosted performance, 5G networks will be able to meet the world's growing demand for wireless connectivity and the requirements of advanced implementations such as self-driving, real-time 3D video streaming, smart homes/cities, and industrial automation. 5G networks are built on a combination of advanced software, hardware, and infrastructure technologies, including mm-wave front-ends, massive MIMO systems, data processing units, and cloud computing networks.

Beamforming phased antenna arrays represent a design approach that has developed rapidly in recent years. These arrays can be deployed as a TX or RX in wireless communication systems and are able to focus signal(s) in a particular direction to enhance signal strength and reduce interference with other signals. A phased antenna array consists of multiple antenna elements arranged in a geometric grid that transmits or receives signals in specific directions. By manipulating the magnitudes and phases of the transmitted or received signals of each antenna element in the array, the signal can be formed in a desired direction and create reliable connections among the users or other wireless devices.

However, mm-wave active beamforming arrays present several challenges, including suitable antenna packaging, power efficiency in beamforming architectures, high path loss, non-linearity, practical array calibration, and the requirement for DPD training methods. To solve these problems, many solutions have been proposed and proven with fabricated

prototypes in the literature. Three approaches have risen in prominence. First, RF beamforming has become the most popular architecture used in mm-wave active phased antenna array applications because of its simple circuitry and high power efficiency compared to other beamforming architectures. Second, PCB-based antenna packaging is now typically deployed for accommodating phased antenna arrays operating at or below Ka-band. The reasons for this trend are the cost-effectiveness of PCB fabrication and the maturity of this packaging technology. Third, the use of a feedback path to apply array calibration and DPD training is becoming more and more attractive to researchers and industrial developers, given the accuracy and reliability of the systems to counter inaccurate array processing and interpretation that result in decreased power efficiency, reduced directivity, and increased interference with other unwanted signals. NF calibration with embedded feedback paths is a desirable functionality for beamforming arrays as it reduces the additional hardware required for far-field setups.

This thesis proposes an NF probing antenna which can be embedded within a PCB-based active phased antenna array, fitting into the constrained spacing between antenna elements of $\lambda/2$ required at 39 GHz. In addition, the distribution of the proposed NF probing antenna can be scaled for any large-scale phased antenna array without sacrificing any design parameters. Moreover, the PCB stack-up proposed for this design is optimized—requiring only three lamination cycles—yet providing sufficient types of vias to accommodate the NF probing antenna structure. The cost of fabrication is also relatively low compared to other antenna packaging solutions. EM simulation and experimental validation results prove that the proposed design is a feasible solution to provide the feedback path for in-field array calibration and DPD training purposes. Results from experimental validation conducted on a custom-built 4×4 active phased array with four embedded NF probing antennas operating at 37-41 GHz were presented. The active phased antenna array was able to steer from $-50°$ to $50°$ on the H-plane, and the embedded NF probing antennas successfully trained a DPD function which then enabled the EIRP to be increased from 32 dBm to 34.3 dBm while maintaining an EVM below 3.5%. Moreover, a prototype of a 4×4 linear-polarized antenna array without NF probing antennas was fabricated to serve as a benchmark, and measurement results confirmed the negligible impact of the NF probing antennas on the phased antenna array's radiation pattern.

In summary, based on the results of experimental validation, it can be inferred that the proposed NF probing antenna is effective in providing a feedback path and could be practically implemented in a co-designed regular phased antenna array for array calibration and DPD training purposes.

5.2 Future Work

The key concept behind the design proposed in this thesis is the creation of a feedback mechanism in a beamforming array for array calibration and DPD training in the NF. The proposed feedback mechanism can be embedded into the main beamforming arrays without any external hardware setup in the far-field, simplifying the setup and making the beamforming array more user-friendly. Work undertaken for this thesis was necessarily targeted and limited; however, the potential of the proposed embedded NF probing antenna should be investigated further. The following list includes suggested projects that could further explore and extend this concept.

- **Larger scaled beamforming arrays (minimum size of 8×8) with embedded NF probing antennas**: Designing and testing a large-scale array would enable researchers to better emulate a base station environment; the mutual couplings and active loading in a large-scale array would be more similar to what occurs in reality in a base station. To achieve such a large-scale array would be a challenging undertaking, although it would be of great value to researchers, and it would also necessitate the development of new calibration/DPD algorithms into which the embedded NF probing antennas could be incorporated.

  Related to the size of the antenna array, the distribution of the proposed NF probing antennas in larger-sized arrays is another interesting topic to delve into. For example, each NF probing antenna is placed at the center of each 2×2 sub-array in this work, however, if the array size increases to 8×8 or even larger, the distribution of the NF probing antennas may need to alter. There may also be an optimal relationship between the size of the main beamforming array and the number of NF probing antennas incorporated.

- **Shared-aperture dual-band beamforming arrays with embedded NF probing antennas**: In the recent literature, most beamforming arrays are operated at a single frequency band such as n257 or n260. Yet, a design that could operate at two different frequency bands simultaneously (allowing multi-standard operation), and generate multi-beam signals directed toward different users would be of great interest to the field. Moreover, embedding the proposed NF probing antenna into a dual-band array for NF array calibration and DPD training would be another novel highlight, as no other design has been proposed for applying NF calibration and DPD training at two different frequencies at the time of writing.

References

[1] "Getting to 5G: Comparing 4G and 5G System Requirements," [Online.] Available: https://www.qorvo.com/design-hub/blog/getting-to-5g-comparing-4g-and-5g-system-requirements, Sep 2017.

[2] "IEEE Standard Letter Designations for Radar-Frequency Bands," *IEEE Std 521-2002 (Revision of IEEE Std 521-1984)*, pp. 1–10, 2003.

[3] "3GPP TS 38.101-1 version 16.5.0 Release 16," [Online.] Available: https://www.etsi.org/deliver/etsi_ts/138100_138199/13810101/16.05.00_60/ts_13810101v160500p.pdf, Nov 2020.

[4] "3GPP TS 38.101-2 version 17.6.0 Release 17," [Online.] Available: https://www.etsi.org/deliver/etsi_ts/138100_138199/13810102/17.06.00_60/ts_13810102v170600p.pdf, Aug 2022.

[5] A. H. Aljuhani, E. Traffenstedt, T. Kanar, S. Zihir, and G. M. Rebeiz, "Ultra-Low Cost Ku-Band Dual-Polarized Transmit and Receive Phased-Arrays for SATCOM and Point-to-Point Applications with Bandwidths up to 750 MHz," in *2019 IEEE International Symposium on Phased Array System Technology (PAST)*, 2019, pp. 8138–8143.

[6] A. J. van den Biggelaar, C. J. C. Vertegaal, U. Johannsen, A. B. Smolders, and M. Geurts, "On the Design and Calibration of a 5G Millimeter-Wave Dual-Polarized Active Phased Array," in *2021 IEEE-APS Topical Conference on Antennas and Propagation in Wireless Communications (APWC)*, 2021, pp. 055–060.

[7] Y. Yin, S. Zihir, T. Kanar, Q. Ma, H. Chung, L. Gao, and G. M. Rebeiz, "A 37–42-GHz 8 × 8 Phased-Array With 48–51-dBm EIRP, 64–QAM 30-Gb/s Data Rates, and EVM Analysis Versus Channel RMS Errors," *IEEE Transactions on Microwave Theory and Techniques*, vol. 68, no. 11, pp. 4753–4764, 2020.

[8] Z. Peterson, "2+N+2 PCB stackup design for HDI boards," [Online.] Available: https://resources.altium.com/p/2n2-pcb-stackup-design-hdi-boards, Oct 2022.

[9] S. Webb, "Overcoming the challenges of HDI design," [Online.] Available: https://www.altium.com/live-conference/sites/default/files/pdf/Overcoming%20the%20Challenges%20of%20HDI%20Design%20-%20Suzy%20Webb.pdf, 2018.

[10] W. Hong, A. Goudelev, K.-h. Baek, V. Arkhipenkov, and J. Lee, "24-Element Antenna-in-Package for Stationary 60-GHz Communication Scenarios," *IEEE Antennas and Wireless Propagation Letters*, vol. 10, pp. 738–741, 2011.

[11] Q.-Q. He, S. Ding, C. Xing, J.-Q. Chen, G.-Q. Yang, and B.-Z. Wang, "Research on Structurally Integrated Phased Array for Wireless Communications," *IEEE Access*, vol. 8, pp. 52 359–52 369, 2020.

[12] A. Bhutani, B. Göttel, A. Lipp, and T. Zwick, "Packaging Solution Based on Low-Temperature Cofired Ceramic Technology for Frequencies Beyond 100 GHz," *IEEE Transactions on Components, Packaging and Manufacturing Technology*, vol. 9, no. 5, pp. 945–954, 2019.

[13] L. Wen, Z. Yu, G. Chi, Y. Huang, T. Cao, J. Wang, and J. Zhou, "Millimeter-Wave Dual-polarized Active Phased Array Antenna for 5G Applications," in *2022 24th International Microwave and Radar Conference (MIKON)*, 2022, pp. 1–3.

[14] H. Kähkönen, J. Ala-Laurinaho, and V. Viikari, "Surface-Mounted Ka-Band Vivaldi Antenna Array," *IEEE Open Journal of Antennas and Propagation*, vol. 2, pp. 126–137, 2021.

[15] S. Li, Z. Zhang, and G. M. Rebeiz, "An Eight-Element 136–147 GHz Wafer-Scale Phased-Array Transmitter With 32 dBm Peak EIRP and ¿16 Gbps 16QAM and 64QAM Operation," *IEEE Journal of Solid-State Circuits*, vol. 57, no. 6, pp. 1635–1648, 2022.

[16] S. Li, Z. Zhang, B. Rupakula, and G. M. Rebeiz, "An Eight-Element 140 GHz Wafer-Scale Phased-Array Transmitter with 32 dBm Peak EIRP and ¿ 16 Gbps 16QAM and 64QAM Operation," in *2021 IEEE MTT-S International Microwave Symposium (IMS)*, 2021, pp. 795–798.

[17] U. Dey, J. Hesselbarth, J. Moreira, and K. Dabrowiecki, "Over-the-Air Test of Dipole and Patch Antenna Arrays at 28 GHz by Probing them in the Reactive Near-Field," in *2020 95th ARFTG Microwave Measurement Conference (ARFTG)*, 2020, pp. 1–4.

[18] M. Löhning, T. Deckert, V. Kotzsch, and M. V. Bossche, "A Novel OTA Near-Field Measurement Approach Suitable for 5G mmWave Wideband Modulated Tests," in *2022 IEEE/MTT-S International Microwave Symposium - IMS 2022*, 2022, pp. 856–858.

[19] S.-C. Chae, H.-W. Jo, J.-I. Oh, G. Kim, and J.-W. Yu, "Coupler Integrated Microstrip Patch Linear Phased Array for Self-Calibration," *IEEE Antennas and Wireless Propagation Letters*, vol. 19, no. 9, pp. 1615–1619, 2020.

[20] N. Tervo, B. Khan, O. Kursu, J. P. Aikio, M. Jokinen, M. E. Leinonen, M. Juntti, T. Rahkonen, and A. Pärssinen, "Digital Predistortion of Millimeter-Wave Phased Array Transmitter With Over-the-air Calibrated Simplified Conductive Feedback Architecture," in *2020 IEEE/MTT-S International Microwave Symposium (IMS)*, 2020, pp. 543–546.

[21] O. Inac, F. Golcuk, T. Kanar, and G. M. Rebeiz, "A 90–100-GHz Phased-Array Transmit/Receive Silicon RFIC Module With Built-In Self-Test," *IEEE Transactions on Microwave Theory and Techniques*, vol. 61, no. 10, pp. 3774–3782, 2013.

[22] R. Murugesu, M. Holyoak, H. Chow, and S. Shahramian, "Linearization of mm-Wave Large-Scale Phased Arrays Using Near-Field Coupling Feedback for ¿10Gb/s Wireless Communication," in *2020 IEEE/MTT-S International Microwave Symposium (IMS)*, 2020, pp. 1271–1274.

[23] X. Liu, W. Chen, L. Chen, F. M. Ghannouchi, and Z. Feng, "Linearization for Hybrid Beamforming Array Utilizing Embedded Over-the-Air Diversity Feedbacks," *IEEE Transactions on Microwave Theory and Techniques*, vol. 67, no. 12, pp. 5235–5248, 2019.

[24] A. B. Ayed, G. Scarlato, P. Mitran, and S. Boumaiza, "On the Effectiveness of Near-Field Feedback for Digital Pre-Distortion of Millimeter-Wave RF Beamforming Arrays," in *2020 IEEE/MTT-S International Microwave Symposium (IMS)*, 2020, pp. 547–550.

[25] A. Ben Ayed, Y. Cao, P. Mitran, and S. Boumaiza, "Digital Predistortion of Millimeter-Wave Arrays Using Near-Field Based Transmitter Observation Receivers," *IEEE Transactions on Microwave Theory and Techniques*, vol. 70, no. 7, pp. 3713–3723, 2022.

[26] Z. He, "A 37-40 ghz dual-polarized 16-element phased-array antenna with near-field probes," [Online.], Available: http://hdl.handle.net/10012/18768, 2022.

[27] Y. Kim, Y. Kim, J. Oh, H. Ji, J. Yeo, S. Choi, H. Ryu, H. Noh, T. Kim, F. Sun, Y. Wang, Y. Qi, and J. Lee, "New Radio (NR) and its Evolution toward 5G-Advanced," *IEEE Wireless Communications*, vol. 26, no. 3, pp. 2–7, 2019.

[28] "Adding channel bandwidth to existing NR bands," [Online.] Available: https://www.3gpp.org/technologies/adding-channel-bandwidth-to-existing-nr-bands, Aug 2022.

[29] "Samsung 5G Vision," [Online.] Available: https://images.samsung.com/is/content/samsung/p5/global/business/networks/insights/white-paper/5g-vision/White-Paper_Samsung-5G-Vision.pdf, 2019.

[30] J. Xia, X. Fang, A. B. Ayed, and S. Boumaiza, "Millimeter Wave SOI-CMOS Power Amplifier With Enhanced AM-PM Characteristic," *IEEE Access*, vol. 8, pp. 8861–8875, 2020.

[31] C. A. Balanis, *Antenna Theory: Analysis and Design*, ser. Fundamental Parameters of Antennas. John Wiley & Sons, Inc. ISBN=0-471-66782-X, 2005.

[32] I. Rosu, "Microstrip, Stripline, CPW, and SIW Design," [Online.] Available: https://www.signalintegrityjournal.com/articles/15-practical-method-for-modeling%-conductor-surface-roughness-using-close-packing-of-equal-spheres, Jul 2016.

[33] P. Delos, B. Broughton, and J. Kraft, "Phased array antenna patterns-part 1: Linear Array Beam characteristics and array factor," [Online.] Available: https://www.analog.com/en/analog-dialogue/articles/phased-array-antenna-patterns-part1.html, May 2020.

[34] J. EbrahimiZadeh, "Beamforming architectures in beyond-5G mmWave Networks," [Online.] Available: https://b5g-mints.eu/blog15/#:~:text=The%20goal%20of%20beamforming%20architectures,keeping%20the%20system%20performance%20high.&text=Conventionally%2C%20massive%20MIMO%20is%20a,serving%20multiple%20single%2Dantenna%20users., Feb 2022.

[35] B. Curran, C. Tschoban, I. Ndip, K.-D. Lang, H. Kroener, and A. Ippich, "Dielectric material characterization of high frequency printed circuit board laminates and an analysis of their transmission line high frequency losses," in *2016 11th European Microwave Integrated Circuits Conference (EuMIC)*, 2016, pp. 528–531.

[36] K. Kibaroglu, M. Sayginer, and G. M. Rebeiz, "A Low-Cost Scalable 32-Element 28-GHz Phased Array Transceiver for 5G Communication Links Based on a 2×2

Beamformer Flip-Chip Unit Cell," *IEEE Journal of Solid-State Circuits*, vol. 53, no. 5, pp. 1260–1274, 2018.

[37] Z. Peterson, "Everything you need to know about Microvias in printed circuit design," [Online.] Available: https://resources.altium.com/p/everything-you-need-know-about-microvias-printed-circuit-design, Dec 2022.

[38] J. Sobolewski and P. Bajurko, "A 120 GHz Antenna for LTCC Package with Via-Less Contact Pads for Probe Measurements," in *2019 13th European Conference on Antennas and Propagation (EuCAP)*, 2019, pp. 1–5.

[39] M. F. Amiruddin, S. Jaafar, S. Bujang, A. Ariffin, A. Sulaiman, N. A. M. Akib, and Y. C. Lee, "Low loss LTCC passive transmission line at Millimeter-wave frequency," in *2010 IEEE Asia-Pacific Conference on Applied Electromagnetics (APACE)*, 2010, pp. 1–4.

[40] S. Liu, J. Fang, Q. Zhu, Y. Wang, and X. Zhang, "A LTCC Antenna Array in Ka-Band for Beam Scanning Applications," in *2021 13th International Symposium on Antennas, Propagation and EM Theory (ISAPE)*, vol. Volume1, 2021, pp. 1–3.

[41] A. Rashidian, S. Jafarlou, A. Tomkins, K. Law, M. Tazlauanu, and K. Hayashi, "Compact 60 GHz Phased-Array Antennas With Enhanced Radiation Properties in Flip-Chip BGA Packages," *IEEE Transactions on Antennas and Propagation*, vol. 67, no. 3, pp. 1605–1619, 2019.

[42] D. G. Kam, D. Liu, A. Natarajan, S. Reynolds, H.-C. Chen, and B. A. Floyd, "LTCC Packages With Embedded Phased-Array Antennas for 60 GHz Communications," *IEEE Microwave and Wireless Components Letters*, vol. 21, no. 3, pp. 142–144, 2011.

[43] M. Ihle, S. Ziesche, C. Zech, and B. Baumann, "Compact LTCC Packaging and Printing Technologies for Sub–THz Modules," in *2018 7th Electronic System-Integration Technology Conference (ESTC)*, 2018, pp. 1–4.

[44] Z. Chen, S. Xu, H. Zhu, W. Feng, W. Che, and Q. Xue, "High-performance Millimeter-Wave Front-end Module Using LTCC Technology," in *2022 23rd International Conference on Electronic Packaging Technology (ICEPT)*, 2022, pp. 1–5.

[45] H.-T. Chou, S.-J. Chou, J. D. S. Deng, C.-H. Chang, and Z.-D. Yan, "LTCC-Based Antenna-in-Package Array for 5G User Equipment With Dual-Polarized Endfire Radiations at Millimeter-Wave Frequencies," *IEEE Transactions on Antennas and Propagation*, vol. 70, no. 4, pp. 3076–3081, 2022.

[46] C. Zhou, W. Yang, Q. Xue, Y. Liu, Y. Xu, and W. Che, "Millimeter-Wave Wideband Dual-Polarized LTCC Antenna Array Based on Metasurfaces for Beam-Scanning Applications," *IEEE Transactions on Antennas and Propagation*, vol. 70, no. 10, pp. 9912–9917, 2022.

[47] W.-M. Chen, P.-Z. Rao, and W.-S. Tung, "LTCC WiGig Radio Module USB Dongle," in *2019 IEEE International Symposium on Phased Array System Technology (PAST)*, 2019, pp. 1–3.

[48] F. Foglia Manzillo, M. Śmierzchalski, L. Le Coq, M. Ettorre, J. Aurinsalo, K. T. Kautio, M. S. Lahti, A. E. I. Lamminen, J. Säily, and R. Sauleau, "A Wide-Angle Scanning Switched-Beam Antenna System in LTCC Technology With High Beam Crossing Levels for V-Band Communications," *IEEE Transactions on Antennas and Propagation*, vol. 67, no. 1, pp. 541–553, 2019.

[49] M. Repeta, W. Zhai, T. Ross, K. Ansari, S. Tiller, H. K. Pothula, D. Wessel, X. Li, H. Cai, D. Liang, G. Wang, and W. Tong, "A Scalable 256-Element E-Band Phased-Array Transceiver for Broadband Communications," in *2020 IEEE/MTT-S International Microwave Symposium (IMS)*, 2020, pp. 833–836.

[50] T. Zhang, Z. Zhu, L. Li, H. Xia, and T. J. Cui, "A 60 GHz LTCC Magneto-Electric Dipole Phased Array with Symmetric Hybrid Feeding Network," in *2019 IEEE International Symposium on Antennas and Propagation and USNC-URSI Radio Science Meeting*, 2019, pp. 2007–2008.

[51] Y. P. Zhang, M. Sun, K. M. Chua, L. L. Wai, and D. Liu, "Antenna-in-Package Design for Wirebond Interconnection to Highly Integrated 60-GHz Radios," *IEEE Transactions on Antennas and Propagation*, vol. 57, no. 10, pp. 2842–2852, 2009.

[52] B. Cao, Y. Shi, and W. Feng, "W-Band LTCC Circularly Polarized Antenna Array With Mixed U-Type Substrate Integrated Waveguide and Ridge Gap Waveguide Feeding Networks," *IEEE Antennas and Wireless Propagation Letters*, vol. 18, no. 11, pp. 2399–2403, 2019.

[53] H. Kähkönen, J. Ala-Laurinaho, and V. Viikari, "Dual-Polarized Ka-Band Vivaldi Antenna Array," *IEEE Transactions on Antennas and Propagation*, vol. 68, no. 4, pp. 2675–2683, 2020.

[54] H. Kahkonen, J. Ala-Laurinaho, and V. Viikari, "A Modular Dual-Polarized Ka-Band Vivaldi Antenna Array," *IEEE Access*, vol. 10, pp. 36 362–36 372, 2022.

[55] H. Kähkönen, S. Proper, J. Ala-Laurinaho, and V. Viikari, "Comparison of Additively Manufactured and Machined Antenna Array Performance at Ka-Band," *IEEE Antennas and Wireless Propagation Letters*, vol. 21, no. 1, pp. 9–13, 2022.

[56] Y. Liu and A. Natarajan, "60 GHz concurrent dual-polarization RX front-end in SiGe with Antenna-IC Co-Integration," in *2017 IEEE Bipolar/BiCMOS Circuits and Technology Meeting (BCTM)*, 2017, pp. 42–45.

[57] U. Kodak, B. Rupakula, S. Zihir, and G. M. Rebeiz, "A Scalable 60 GHz Tx/Rx 2x64-Element Dual-Polarized Dual-Beam Wafer-Scale Phased-Array with Integrated Dual-Transceivers," in *2019 IEEE MTT-S International Microwave Symposium (IMS)*, 2019, pp. 1068–1071.

[58] U. Kodak, B. Rupakula, S. Zihir, and G. Rebeiz, "60-GHz 64- and 256-Element Dual-Polarized Dual-Beam Wafer-Scale Phased-Array Transceivers With Reticle-to-Reticle Stitching," *IEEE Transactions on Microwave Theory and Techniques*, vol. 68, no. 7, pp. 2745–2767, 2020.

[59] S. Li, Z. Zhang, B. Rupakula, and G. M. Rebeiz, "An Eight-Element 140-GHz Wafer-Scale IF Beamforming Phased-Array Receiver With 64-QAM Operation in CMOS RFSOI," *IEEE Journal of Solid-State Circuits*, vol. 57, no. 2, pp. 385–399, 2022.

[60] R. Long, J. Ouyang, F. Yang, W. Han, and L. Zhou, "Multi-Element Phased Array Calibration Method by Solving Linear Equations," *IEEE Transactions on Antennas and Propagation*, vol. 65, no. 6, pp. 2931–2939, 2017.

[61] S. Y. Kim, O. Inac, C.-Y. Kim, D. Shin, and G. M. Rebeiz, "A 76–84-GHz 16-Element Phased-Array Receiver With a Chip-Level Built-In Self-Test System," *IEEE Transactions on Microwave Theory and Techniques*, vol. 61, no. 8, pp. 3083–3098, 2013.

[62] N. Tervo, B. Khan, O. Kursu, J. P. Aikio, M. Jokinen, M. E. Leinonen, M. Juntti, T. Rahkonen, and A. Pärssinen, "Digital Predistortion of Phased-Array Transmitter With Shared Feedback and Far-Field Calibration," *IEEE Transactions on Microwave Theory and Techniques*, vol. 69, no. 1, pp. 1000–1015, 2021.

[63] "What is Back Drilling in PCB Design and Manufacturing," [Online.] Available: https://www.protoexpress.com/blog/back-drilling-pcb-design-and-manufacturing/, 2020.

[64] "The difference of PCB Back Drilling and Controlled Depth Drilling," [Online.] Available: https://wellerpcb.com/the-difference-of-pcb-back-drilling-and-controlled-depth-drilling/, 2021.

[65] "Astra® MT77," [Online.] Available: https://www.isola-group.com/pcb-laminates-prepreg/astra-mt77-laminate-and-prepreg/, 2021.

[66] B. Salski, J. Cuper, T. Karpisz, P. Kopyt, and J. Krupka, "Complex permittivity of common dielectrics in 20–110 ghz frequency range measured with a fabry–pérot open resonator," *Applied Physics Letters*, vol. 119, no. 5, p. 052902, 2021. [Online]. Available: https://doi.org/10.1063/5.0054904

[67] "pushPIN™ Heat Sink," [Online.] Available: https://www.qats.com/Search/HeatSink/3018.aspx#data_sheet.

[68] "5mm x 20M Double Side Adhesive Thermal Conductive Tape For Heatsink Chipset LED GPU," [Online.] Available: https://www.amazon.ca/Adhesive-Thermal-Conductive-Heatsink-Chipset/dp/B06XRXVGZN?th=1, 2017.

[69] M. Maggi, S. Hidri, L. Marnat, M. Ettorre, G. Orozco, M. Margalef-Rovira, C. Gaquière, and K. Haddadi, "Millimeter-Wave Phased Arrays and Over-the-Air Characterization for 5G and Beyond: Overview on 5G mm-Wave Phased Arrays and OTA Characterization," *IEEE Microwave Magazine*, vol. 23, no. 5, pp. 67–83, 2022.

[70] E. Cohen, M. Ruberto, M. Cohen, H. K. Pan, and S. Ravid, "Antenna packaging of a 32 element TX/RX phased array RFIC for 60 GHz communications," in *2013 IEEE International Conference on Microwaves, Communications, Antennas and Electronic Systems (COMCAS 2013)*, 2013, pp. 1–5.

[71] J. L. Salazar-Cerreno, Z. Qamar, and N. Aboserwal, "A Multipurpose and Reconfigurable mm-Wave Scanner System for Accurate Measurements of Passive/Active Antenna array, Array Calibration, Radome and Material Characterization," in *2021 IEEE Conference on Antenna Measurements Applications (CAMA)*, 2021, pp. 555–559.

[72] T. Takahashi, N. Nakamoto, M. Ohtsuka, T. Aoki, Y. Konishi, I. Chiba, and M. Yajima, "On-Board Calibration Methods for Mechanical Distortions of Satellite Phased Array Antennas," *IEEE Transactions on Antennas and Propagation*, vol. 60, no. 3, pp. 1362–1372, 2012.

[73] A. Nafe, K. Kibaroglu, M. Sayginer, and G. M. Rebeiz, "An In-Situ Self-Test and Self-Calibration Technique Utilizing Antenna Mutual Coupling for 5G Multi-Beam TRX Phased Arrays," in *2019 IEEE MTT-S International Microwave Symposium (IMS)*, 2019, pp. 1229–1232.

[74] A. Nafe, A. H. Aljuhani, K. Kibaroglu, M. Sayginer, and G. M. Rebeiz, "In-Situ Self-Test and Self-Calibration of Dual-Polarized 5G TRX Phased Arrays Leveraging Orthogonal-Polarization Antenna Couplings," in *2020 IEEE/MTT-S International Microwave Symposium (IMS)*, 2020, pp. 1081–1084.

[75] S. Shahramian, M. J. Holyoak, A. Singh, and Y. Baeyens, "A Fully Integrated 384-Element, 16-Tile, W -Band Phased Array With Self-Alignment and Self-Test," *IEEE Journal of Solid-State Circuits*, vol. 54, no. 9, pp. 2419–2434, 2019.